Graduate Theses, Dissertations, and Problem Reports

2006

Study of the dynamic behavior of tablet movement in a rotating drum using discrete element modeling (DEM) method

Yongxin Song
West Virginia University

Follow this and additional works at: https://researchrepository.wvu.edu/etd

Study of the Dynamic Behavior of Tablet Movement in a Rotating

Drum Using Discrete Element Modeling (DEM) Method

Yongxin Song

Dissertation Submitted to the
College of Engineering and Mineral Resources
at West Virginia University
in partial fulfillment of the requirements
for the degree of

Doctor of Philosophy
in
Chemical Engineering

Dr. Richard Turton, Chair
Dr. Eugene V. Cilento
Dr. Charter D. Stinespring
Dr. Paula J. Stout
Dr. Wu Zhang

Department of Chemical Engineering

Morgantown, West Virginia
2006

Keywords: rotating drum, discrete element modeling, tablet, contact algorithm, movement,

liquid bridge

Abstract

Particle shape is a very important factor affecting the accuracy of discrete element modeling (DEM) simulations. Therefore, the purpose of this study is to determine its effect on the dynamic behavior of tablet movement in a rotating drum. First, the shape of typical standard round tablets was represented using the intersection of three convex spherical surfaces. Contact algorithms for Tablet-Flat Surface, Tablet-Curved Surface and Tablet-Tablet were developed based on the geometry of this representation of the tablets' shape. Good agreement was obtained between the simulation results for the collision of two tablets and those obtained from experiments. In addition, simulation results for the collision of two tablets using multi-sphere representations showed that the dynamic behavior of the tablet was very different from any of the multi-sphere representations.

A study of the effect of liquid bridging between two tablets on the dynamic behavior of tablets indicated that the capillary force can be ignored compared to the viscous forces caused by the liquid bridge, especially for liquids with high viscosity. Additionally, there was a linear relationship between limiting separation distance and viscosity of the liquid. The order of magnitude of the limiting separation distance in the liquid force model is about 1 mm.

For the multi-particle DEM simulations using spheres in rotating drums, the simulations reached steady state after approximately 6 s of pan rotation. A study of the influence of particle size and the radius of the drum on the surface velocity of particles along the inclined surface showed that the surface velocity of particles was inversely proportional to the square root of the diameter of the particles, and the surface velocity of particles is proportional to the square of the radius of the drum. In addition, the fractional fill volume in the 29 cm drum should be larger than 0.25 to obtain a velocity profile consistent with larger equipment.

Comparison of the surface velocity profiles from multi-particle simulations using tablets with that from multi-particle simulations using spheres showed that the surface velocity of tablets was much larger than that for spherical particles. It was also found that simulation results for batches of 1500 tablets and spheres in a rotating drum showed that the computational time for tablet simulations was about 60 times longer than that for spherical particle simulations.

Table of Contents

iv

List of Figures

List of Tables

Acknowledgements

There are a number of people who have been important in the completion of this dissertation, both academically and personally. This work, and the time that I have spent engaged in this Ph. D. program, would have been much poorer without them. I owe them a lot.

First, I would like to express my appreciation to my advisor, Dr. Richard Turton, for the source of knowledge, guidance, and support that he has shown to me over the past years. His encouragement of my work and commitment to whatever project we would undertake was inspiring, and has made the time I have spent here enjoyable. It has been a privilege to work with him. I am extremely grateful to my doctoral committee members, Dr. Eugene V. Cilento, Dr. Charter D. Stinespring, Dr. Paula J. Stout and Dr. Wu Zhang, for their invaluable assistance and suggestions. I am fortunate to have the opportunity to work here and meet all the faculty, staff and graduate students in the department of Chemical Engineering. I appreciate all their friendship and their collective encouragement to finish this dissertation.

I would like to thank my parents, for their unconditional love and support throughout my life, but especially in attaining this degree. I am also thankful to my wife's parents, and my sister-in-law, Xiu-Xiu Cheng, for their love and encouragement that they have given me ever since I met them.

The best thing that has happened to me throughout my doctoral program has nothing to do with my dissertation at all. I would like to thank my lovely and beautiful wife, Xiufang Cheng, for the understanding, patience and support she has shown me as I have tried to complete this dissertation. I could not have done it without her help.

For Xiufang, as always.

1. Introduction

There are many engineering processes involving the handling of particulate or bulk materials in a variety of industries. These processes include mixing, drying, milling, coating, granulation and agglomeration and they utilize chutes, hoppers, rotating drums, fluidized beds, etc. In order to optimize these processes, a comprehensive understanding of the flow behavior of particulate materials in this equipment is essential. Even though the flow behavior of particulate materials has been studied through experimental and theoretical methods for more than one hundred years, many aspects of particle flow in the equipment are still not well understood. Therefore, computational methods to investigate the flow behavior of particulate assemblies have captured the interest of many engineers.

Simulation tools for particulate movement include Computational Fluid Dynamics (CFD) and Discrete Element Modeling (DEM) methods. In CFD methods, governing equations are solved numerically based on the momentum and continuity of gas, liquid and/or solids flow in the equipment. However, there are some disadvantages to the application of CFD. First, choosing the right equations of state for CFD calculations is difficult. The uncertainty of the equation of state exists even for the simplest problem, such as solids flow from a hopper. In addition, some limitations are placed on the boundary conditions for a CFD approach. Since these limitations do not exist for the application of the DEM method, DEM approaches have become another predominant tool to study the dynamic behavior of particulate systems.

For simplicity, non-spherical particle DEM simulations may be carried out by utilizing spherical particles having the same volume as the particles of interest [1]. However, the dynamic behavior of particle movement in rotating drums is significantly different from those of spheres by using the above approximation [2]-[3]. Hence, a more realistic representation of

non-spherical particles should be used for DEM simulations. In addition, the application of a liquid solution to a bed of solids is involved in coating and wet granulation processes in the pharmaceutical industry. It is well known that even a small amount of liquid has a significant effect on the characteristics of particulate flow [4]. Therefore, the effect of liquid bridging on the particle movement should be taken into account.

In this work, a representation for tablet-shaped particles is developed. Then contact algorithms for tablet-shaped particles are developed based on this representation. These are then implemented for tablet-tablet contact in a DEM simulation. The effect of liquid bridges on the dynamic behavior of tablet-tablet contact is also investigated using DEM simulation. Finally, multi-particle DEM simulation using tablets in a rotating drum is studied. It is believed that the DEM approach will become a powerful tool to investigate particle movement in particulate systems, especially for tablet coating in rotating drums in the pharmaceutical industry.

2. Literature Review

2.1 Discrete Element Modeling (DEM) method

The Discrete Element Modeling (DEM) method, which was developed by Cundall [5]-[6], is an explicit numerical scheme which includes several related mathematical tools to capture the behavior of the solids in particulate systems. It allows finite displacement, rotation and separation of each particle. In fact, as a numerical technique, DEM is analogous to the molecular dynamics simulations, which have been used widely to investigate the structure and dynamics of molecular liquids and solids [7]-[12]. However, DEM simulation is more complicated due to the non-linear and non-central interactions between particles arising from asymmetrical structures of particles, friction and the presence of a viscous fluid. DEM is applied to particulate systems to obtain the macroscopic behavior of the system by a series of calculations of the linear and angular motion of each individual particle in the system. Then the flow of the particulate system is determined by each particle's trajectory along with its time evolution.

In the above dynamic methods, the ordinary differential equations, based on Newton's Laws of motion, are used to describe the motion of the solids and these equations are integrated numerically by using a step-by-step integration procedure. In these cases, the time step is chosen to be small enough so that the velocities and accelerations of the solids may be assumed constant. In order to make the simulation more accurate, the time step chosen should also be small enough so that except for its immediate neighbors, other solids can not directly influence the properties of the particle of interest.

Utilizing a simple algorithm in which the values of positions and forces at a previous time step are used, and the linear velocities are known at the mid-point of each time-step, Walton and Braun [13] used Newton's equations of motion, which are expressed as two first order differential equations in each space dimension, to generate the particles' trajectories. Thus,

$$\frac{dv_i}{dt} = g_i + F_i / m, \qquad i = x, y, z \tag{2.1}$$

$$\frac{dr_i}{dt} = v_i, \qquad i = x, y, z \tag{2.2}$$

So the integrated forms of Eqs. 2.1 and 2.2, based on a time step Δt, are:

$$v_i^{n+1/2} = v_i^{n-1/2} + \left(g_i + \frac{F_i^n}{m} \right) \times \Delta t, \quad i = x, y, z \tag{2.3}$$

$$r_i^{n+1} = r_i^n + v_i^{n+1/2} \times \Delta t, \qquad i = x, y, z \tag{2.4}$$

where the superscript refers to the time-step, v is velocity, r is the position, F is the total surface force acting on the particle, m is the mass of the particle and g is the gravitational acceleration.

The resulting equations for the components of angular velocities in a body-fixed coordinate system are given by Euler's equations of motion,

$$\frac{d\omega_x^b}{dt} = \frac{\tau_x^b}{I_{xx}} + \left(\frac{I_{yy} - I_{zz}}{I_{xx}} \right) \omega_y^b \omega_z^b \tag{2.5}$$

$$\frac{d\omega_y^b}{dt} = \frac{\tau_y^b}{I_{yy}} + \left(\frac{I_{zz} - I_{xx}}{I_{yy}} \right) \omega_z^b \omega_x^b \tag{2.6}$$

$$\frac{d\omega_z^b}{dt} = \frac{\tau_z^b}{I_{zz}} + \left(\frac{I_{xx} - I_{yy}}{I_{zz}} \right) \omega_x^b \omega_y^b \tag{2.7}$$

4

where I_{xx}, I_{yy} and I_{zz} are the diagonal elements of the moment of inertia tensor in the body-fixed coordinate system, and τ_x, τ_y and τ_z are the three components of the torque in each resolved direction acting on the particle. The value of the torque for the previous time step is used and the angular velocities are known at the mid-point of the time-step.

From Eqs. 2.5-2.7, it is easy to integrate these three equations to obtain the angular velocity of the particles at different time steps. So a predictor-corrector algorithm is used to estimate the angular velocity from the previous time step values. The procedures for implementing this algorithm are:

(1) Angular velocities are estimated at the current time step by assuming constant angular acceleration for an additional one-half time step:

$$\omega_i^{'n} = \omega_i^{n-1/2} + \Delta\omega_i^{n-1/2} / 2, \qquad i = x, y, z \tag{2.8}$$

(2) Extrapolated angular velocities are used, along with the current torques, to make a first prediction of the angular accelerations at the current time step:

$$\Delta\omega_x^{'n} = \left[\frac{\tau_x^b}{I_{xx}} + \left(\frac{I_{yy} - I_{zz}}{I_{xx}} \right) \omega_y^{'b} \omega_z^{'b} \right] \Delta t \tag{2.9}$$

$$\Delta\omega_y^{'n} = \left[\frac{\tau_y^b}{I_{yy}} + \left(\frac{I_{zz} - I_{xx}}{I_{yy}} \right) \omega_z^{'b} \omega_x^{'b} \right] \Delta t \tag{2.10}$$

$$\Delta\omega_z^{'n} = \left[\frac{\tau_z^b}{I_{zz}} + \left(\frac{I_{xx} - I_{yy}}{I_{zz}} \right) \omega_x^{'b} \omega_y^{'b} \right] \Delta t \tag{2.11}$$

(3) The predicted angular accelerations above are used to predict more accurately the angular velocities at the current time step:

$$\omega_i^n = \omega_i^{n-1/2} + \Delta\omega_i^{'n} / 2, \qquad i = x, y, z \tag{2.12}$$

5

(4) The corrected values for the derivatives are obtained:

$$\Delta \omega_x^n = \left[\frac{\tau_x^b}{I_{xx}} + \left(\frac{I_{yy} - I_{zz}}{I_{xx}} \right) \omega_y^b \omega_z^b \right] \Delta t \qquad (2.13)$$

$$\Delta \omega_y^n = \left[\frac{\tau_y^b}{I_{yy}} + \left(\frac{I_{zz} - I_{xx}}{I_{yy}} \right) \omega_z^b \omega_x^b \right] \Delta t \qquad (2.14)$$

$$\Delta \omega_z^n = \left[\frac{\tau_z^b}{I_{zz}} + \left(\frac{I_{xx} - I_{yy}}{I_{zz}} \right) \omega_x^b \omega_y^b \right] \Delta t \qquad (2.15)$$

(5) The angular velocities at the midpoint of the next time step are calculated:

$$\omega_i^{n+1/2} = \omega_i^{n-1/2} + \Delta \omega_i^n, \qquad\qquad i = x, y, z \qquad (2.16)$$

In general, there are two different types of DEM methods for granular materials: a "hard" particle approach and a "soft" particle approach, respectively. In hard-particle models, it is assumed that the interaction forces between particles are impulsive. The linear and angular momentum is balanced between interacting particles based on the collision dynamics. Different collision models have been proposed and their application to granular flows has been simulated using a hard-particle approach method [14]-[17]. However, the main area of application of the hard-particle approach is rapid granular flows.

The soft-particle approach is different from the hard-particle approach in that the inter-particle collisions are treated as a continuous process that take place over a finite time. Apart from external forces acting on the system, the interacting forces between particles are of key importance to the soft-particle model. The interacting contact forces exerted on each particle are predicted as continuous functions of the overlap between interacting particles on the basis of some contact-force models, which will account for the physical properties of the particles,

such as Young's Modulus, Poisson ratio, etc. Although this approach is more computationally intensive, it can provide more useful information about the structure and dynamic behavior of granular materials. Therefore, the soft-particle approach will be used in this work.

From the above discussion, it is clear that when the DEM method is used to simulate the tablet movement in the rotating drum, the appropriate models for estimating the interaction forces between two particles must be applied. The following section discusses these models as applied to the DEM method.

2.2 Contact Force Models

In general, there are many interacting forces between particles which include Van der Waals forces, electrostatic forces and mechanical forces, etc. But when the particle size increases, Van der Waals forces and electrostatic forces between particles typically become less important. So for this particular research, these forces will be neglected. Only the mechanical forces caused by particles interacting with each other will be considered.

2.2.1 Hertz theory of elastic contact

Hertz [18] was the first person to provide a satisfactory analysis of the stress at the contact of two elastic solids. He made the following assumptions in his theory:

(1) The contact area of two elastic solids is elliptical;

(2) Each solid is an elastic half-space;

(3) The dimensions of the contact area are much less than the body's dimensions;

(4) There is no friction between two elastic solids when they contact.

The simple case of two identical spherical elastic solids of radius R is shown in Figure 2.1.
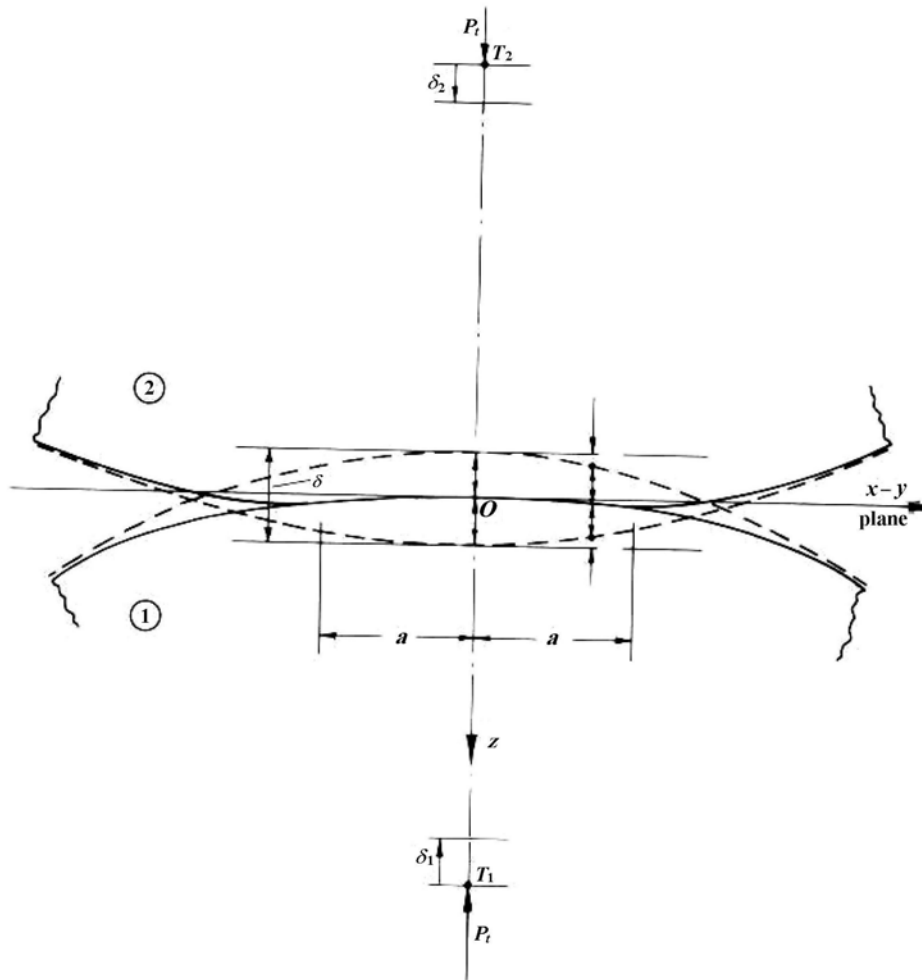
Figure 2.1 Displacement of particles in contact (Johnson [19])

From the above assumptions, the contact area is a circle whose radius is a for spherical elastic bodies. The radius of the contact circle is

$$a = \left(\frac{3P_t R}{4E^*} \right)^{1/3}$$

(2.17)

And the overlap of two spherical particles is

$$\delta = \frac{a^2}{R} = \left(\frac{9P_t^2}{16RE^{*2}} \right)^{1/3}$$

(2.18)

In the above equations

$$\frac{1}{E^*} = \frac{1-v_1^2}{E_1} + \frac{1-v_2^2}{E_2} \qquad (2.19)$$

where E_1 and E_2 are the Young's modulus, v_1 and v_2 are the Poisson ratios of the two particles, respectively. P_t is the total loading force acting on the two particles.

In reality, during the course of particle-particle interactions, particles will lose some energy. In addition, when the particles slide in the presence of a normal force, there is a tangential force between the particles. So other contact-force models must be used.

2.2.2 The Force-Displacement Model (FDM)

Cundall and Strack [20] introduced the FDM method for the case of two discs in contact. Discs x and y, whose radii and masses are $R_{(x)}$, $R_{(y)}$ and $m_{(x)}$, $m_{(y)}$ respectively, are shown in Figure 2.2. The centers of the two discs are $x_i = (x_1, x_2)$ and $y_i = (y_1, y_2)$ where the subscripts 1 and 2 refer to the coordinates of a Cartesian system as shown in Figure 2.2.

From Figure 2.2, it can be seen that when the distance L between two centers is less than the sum of the radii of two discs, the two discs are in contact with each other. After that, the relative displacement at the contact point C (see Figure 2.2) is determined by the relative velocity of the two discs. The definition of the relative velocity is the velocity of point $P_{(x)}$ with respect to point $P_{(y)}$. The unit vector shown in Figure 2.2 from the center of disc x to the center of disc y is:

$$e_i = \frac{y_i - x_i}{D} = (\cos\varphi, \sin\varphi) \qquad (2.20)$$
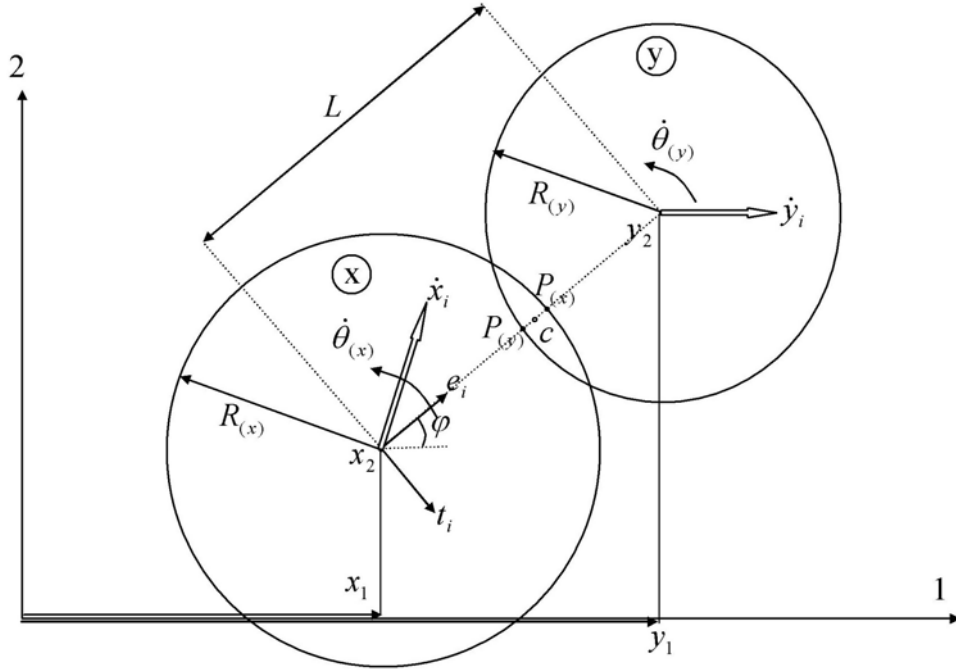
Figure 2.2 The schematic diagram of force-displacement law

When the unit vector e_i is rotated clockwise through 90^0 based on the center of disc x, the new vector, t_i, is

$$t_i = (e_2, -e_1) \tag{2.21}$$

So the relative velocity of point $P_{(x)}$ with respect to point $P_{(y)}$ expressed by $\dot{X}_i$ is

$$\dot{X}_i = (\dot{x}_i - \dot{y}_i) - (\dot{\theta}_{(x)} R_{(x)} + \dot{\theta}_{(y)} R_{(y)}) t_i \tag{2.22}$$

So the projections of $\dot{X}_i$ onto e_i and t_i are

$$\dot{n} = \dot{X}_i e_i = (\dot{x}_i - \dot{y}_i) e_i - (\dot{\theta}_{(x)} R_{(x)} + \dot{\theta}_{(y)} R_{(y)}) t_i e_i = (\dot{x}_i - \dot{y}_i) e_i \tag{2.23}$$

$$\dot{s} = \dot{X}_i t_i = (\dot{x}_i - \dot{y}_i) t_i - (\dot{\theta}_{(x)} R_{(x)} + \dot{\theta}_{(y)} R_{(y)}) t_i t_i$$

$$\therefore \quad \dot{s} = (\dot{x}_i - \dot{y}_i) t_i - (\dot{\theta}_{(x)} R_{(x)} + \dot{\theta}_{(y)} R_{(y)}) \tag{2.24}$$

where the Einstein summation convention is adopted for the index i. Therefore, by integrating the relative velocity component with respect to time, the components Δn and Δs of the relative displacement increments are

$$\Delta n = (\dot{n})\Delta t = ((\dot{x}_i - \dot{y}_i)e_i)\Delta t \tag{2.25}$$

$$\Delta s = (\dot{s})\Delta t = ((\dot{x}_i - \dot{y}_i)t_i - (\dot{\theta}_{(x)}R_{(x)} + \dot{\theta}_{(y)}R_{(y)}))\Delta t \tag{2.26}$$

By using the above relative displacement increments along with the force-displacement law, ΔF_n and ΔF_s, the increments of the normal and shear forces, are

$$\Delta F_n = k_n\Delta n = k_n((\dot{x}_i - \dot{y}_i)e_i)\Delta t \tag{2.27}$$

$$\Delta F_s = k_s\Delta s = k_s((\dot{x}_i - \dot{y}_i)t_i - (\dot{\theta}_{(x)}R_{(x)} + \dot{\theta}_{(y)}R_{(y)}))\Delta t \tag{2.28}$$

where k_n and k_s are the normal and shear stiffnesses, respectively. These two parameters can be estimated based on the physical properties of the particles or using experimental methods.

Finally, adding the increments of the normal and shear forces to the normal and shear forces at the previous time step, the forces at the current time step are

$$(F_n)_N = (F_n)_{N-1} + \Delta F_n; \quad (F_s)_N = (F_s)_{N-1} + \Delta F_s \tag{2.29}$$

where the subscripts N and $N-1$ represent the times t_N and t_{N-1} which satisfy $t_N - t_{N-1} = \Delta t$.

Figure 2.3 shows the sign convention for the normal and shear forces acting on the disc x.
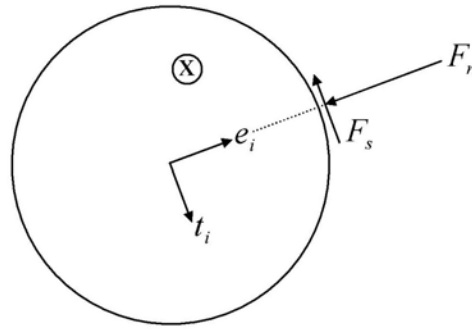
Figure 2.3 Sign convention for F_n and F_s

In Figure 2.3, F_n and F_s are positive in the directions opposite to e_i and t_i. But there is a limitation for shear force in this model. The maximum value of the magnitude of the shear force should be less than or equal to the maximum possible value $(F_s)_{max}$ which is defined as

$$(F_s)_{max} = F_n \tan \phi_\mu + c \tag{2.30}$$

where ϕ_μ is the smaller of the inter-particle friction angles of the two discs in contact and c is the smaller of their cohesions. If the absolute value of $(F_s)_N$ from Eq. 2.29 is larger than $(F_s)_{max}$, $(F_s)_N$ is set equal to $(F_s)_{max}$ in order to maintain the sign from Eq. 2.29. Hallquist [21] first proved that for perfectly elastic spheres, the relationship between Hertz's normal force and the relative approach (overlap) is

$$F_n = K_n \delta^{3/2} \tag{2.31}$$

where K_n is elastic stiffness, δ is the relative approach (overlap) after initial contact.

Walton and Braun [22] used the Inter-particulate Normal Force Model and Incremental Slipping Friction Model in a one dimensional approximation for inelastic, frictional granular solid flows. For ease of calculation in the two-dimensional disk interaction model, they used a partially-latching-spring model to approximate the disks' behavior, which is obtained by the finite element calculations of elastic-plastic spheres and observed in experiments as shown in Figure 2.4. In this model, the normal force is

$$\begin{cases} F_n = K_1 \delta & \text{For loading} \\ F_n = K_2 (\delta - \delta_0) & \text{For unloading} \end{cases} \tag{2.32}$$

where δ is the relative approach (overlap) after initial contact, and δ_0 is the value of δ where the unloading force goes to zero. No negative values are permitted for normal force F.
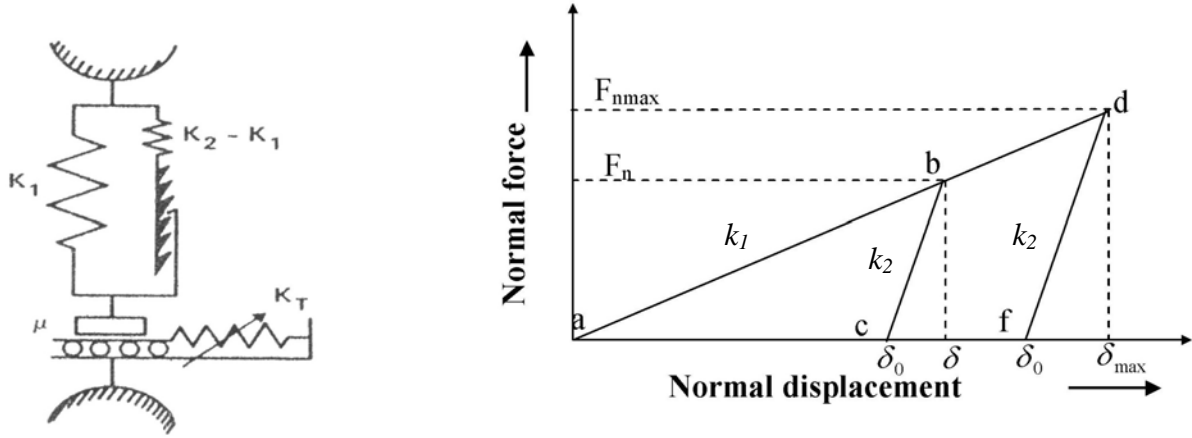
Figure 2.4 Schematic of partially latching-spring model and the corresponding normal force deflection curve used to describe inelastic normal direction forces acting between two colliding disks. (Walton and Braun [22])

The right hand side of Figure 2.4 shows that initial loading is along the line from a to b with slope K_1. Before the maximum relative overlap is reached, unloading is initiated. So unloading is along the line from b to c. And reloading from point c gives the path c, b, d. After reaching the maximum overlap, unloading is from d to f, to c and finally to a. Therefore, for this normal force model, there is a position dependent hysteresis which leads to a less-than-unity coefficient of restitution defined as follows:

$$e = \left(\frac{K_1}{K_2} \right)^{1/2}$$

(2.33)

where e is the ratio of initial to final relative velocities in the normal direction.

For the tangential friction force model, Mindlin, and Mindlin and Deresiewicz [23]-[24] proposed theoretical models for the friction forces between elastic spheres in contact. Walton and Braun [22] gave the definition of the effective tangential stiffness, K_T, to approximate the expressions of Mindlin and Deresiewicz. The effective tangential stiffness, K_T, is

$$
K_T = \begin{cases} K_0 \left(1 - \dfrac{T - T^*}{\mu F_n - T^*} \right)^{\lambda} & \text{For } T \text{ increasing} \\[4ex] K_0 \left(1 - \dfrac{T^* - T}{\mu F_n + T^*} \right)^{\lambda} & \text{For } T \text{ decreasing} \end{cases}
\tag{2.34}
$$

where T is the total tangential force, K_0 is the initial tangential stiffness, μ is the coefficient

of friction, F_n is the total normal force, λ is a fixed parameter usually set to one-third to agree

with Mindlin's theory, and T^*, which is initially zero, is subsequently set to the value of the

total tangential force, T, whenever the relative tangential slip reverses direction.

For finite difference methods, the tangential force, $T^{'}$, at the current time step is obtained

from the old tangential force, T, at the previous time step plus the incremental force, which is

caused by the relative surface displacement between the contacting particles. The expression is

$$
T^{'} = T + K_T \Delta s
\tag{2.35}
$$

with K_T given by Eq. 2.34 and Δs is called the relative tangential surface displacement at the

current time interval. According to Amonton's Law, there exists a maximum value of

tangential force, T, namely

$$
T \leq \mu F_n
\tag{2.36}
$$

Therefore, in order to obtain the total tangential force acting on the particles, only the value

of two parameters at the previous time step are used.

Figure 2.5 shows the relationship between the tangential force and tangential surface

displacement for this incrementally slipping friction model.
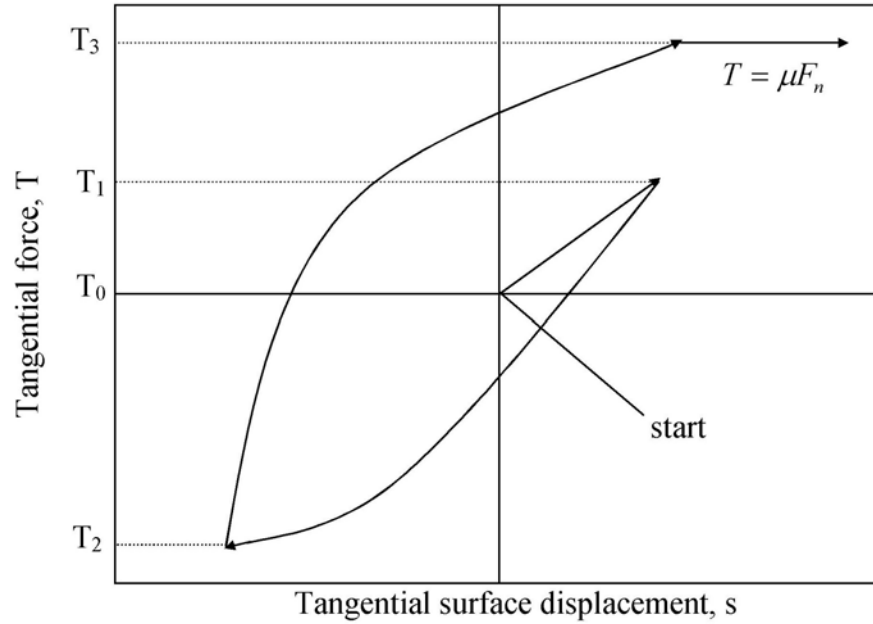
Figure 2.5 The relationship of tangential force with tangential surface displacement

Walton [25] proposed a two-dimensional model to calculate the tangential surface displacement. Here the tangential surface displacement is separated into two parts: one is parallel to the current friction force and the other perpendicular to the friction force. Later they are combined together vectorially.

Since the direction of the normal force at contact is changed for every time step, Walton [25] suggested using vector manipulation to implement this friction model. Because the time step is very small, it is assumed that the tangential surface displacement at one time step is relatively small. For two spheres in contact, let $\hat{k}_{ij}$ be the current unit from the center of sphere i to the center of sphere j, that is, $\hat{k}_{ij} = (\vec{r}_j - \vec{r}_i)/|\vec{r}_j - \vec{r}_i|$, where $\vec{r}_i$ is the radius vector for the location of sphere i, etc. From the definition of $\hat{k}_{ij}$, it is also the unit normal at the contact point between two spheres. The procedures for calculating the tangential surface displacement and tangential force at the current time step are:

(1) The tangential force at the previous time step, $\vec{T}_{old}$, is projected onto the current tangent plane;

$$\vec{T}_0 = \hat{k}_{ij} \times \vec{T}_{old} \times \hat{k}_{ij} = \vec{T}_{old} - \hat{k}_{ij}\left(\hat{k}_{ij} \cdot \vec{T}_{old}\right) \tag{2.37}$$

(2) This projected friction force is normalized to get the same magnitude of the old tangential force, and to get the unit vector for this "new" tangential force;

$$\vec{T} = \left|\vec{T}_{old} / \vec{T}_0\right|\vec{T}_0, \qquad \hat{t} = \vec{T} / \left|\vec{T}\right| \tag{2.38}$$

(3) The relative surface tangential displacement is calculated from the properties of two spheres at the previous time step, then the projected surface displacement on the contact tangent plane is obtained;

$$\Delta\vec{s}^{\,n-1/2} = \left[\hat{k}_{ij} \times \left(\vec{v}_i^{\,n-1/2} - \vec{v}_j^{\,n-1/2}\right) \times \hat{k}_{ij} + \vec{r}_i\left(\vec{\omega}_i^{\,n-1/2} \times \hat{k}_{ij}\right) + \vec{r}_j\left(\vec{\omega}_j^{\,n-1/2} \times \hat{k}_{ij}\right)\right]\Delta t \tag{2.39}$$

where $\vec{v}$ is the linear velocity, $\vec{\omega}$ is the angular velocity, Δt is the time step.

The displacements parallel and perpendicular to the "new" friction force are

$$\Delta\vec{s}_{\parallel} = \left(\Delta\vec{s}^{\,n-1/2} \cdot \hat{t}\right)\hat{t}, \qquad \Delta\vec{s}_{\perp} = \Delta\vec{s}^{\,n-1/2} - \Delta\vec{s}_{\parallel} \tag{2.40}$$

(4) The tangential force at the current time step is calculated from;

$$\vec{T}_{\parallel} = \vec{T} + K_T\Delta\vec{s}_{\parallel}, \qquad \vec{T}_{\perp} = K_0\Delta\vec{s}_{\perp}$$

$$\vec{T}' = \vec{T}_{\parallel} + \vec{T}_{\perp} \tag{2.41}$$

(5) Finally, this value is checked to make sure that the magnitude of this friction force abides by Amonton's Law.

Thornton [26] proposed a simplified theoretical model for the normal contact between two elastic-perfectly plastic spheres. He assumed that quasi-static contact mechanic theories are valid during the interaction of two spheres. There is a Hertzian elastic component along with a plastic deformation component for the normal force. Therefore, for initial loading where the

elastic limit has not been exceeded, the normal force follows the Hertz theory. Once the plastic limit is exceeded, Thornton [26] assumed a linear relationship between the normal force and the normal displacement for continued loading which is described by

$$F_n = F_y + k_y (\delta - \delta_y) \tag{2.42}$$

where $k_y = \dfrac{3F_y}{2\delta_y}$ (slope of F vs δ curve is continuous at δ_y), δ_y is the elastic limit (defined through F_y, a fitting parameter). And k_y is called the "plastic stiffness". When unloading occurs, two possibilities occur. If the elastic limit is not exceeded, then the normal force just follows the Hertz theory. However, if the elastic limit has been exceeded, then the normal force is given by

$$F_n = F_{max} - k_{un} (\delta_{max} - \delta)^{3/2} \sqrt{\overline{R}} \tag{2.43}$$

where $\overline{R}$ is the ratio of the new contact radii due to plastic deformation, R' and R^*

$$\overline{R} = \frac{R'}{R^*} = \frac{F_y}{F_{max}} \left(\frac{2F_{max} + F_y}{3F_y} \right)^{3/2} \tag{2.44}$$

and k_{un} is the plastic stiffness for unloading.

The Normal Force-Normal Displacement characteristics are shown in Figure 2.6.

There are other Normal FDMs, such as those applied by Tsuji et al., Yamane et al. and Mishra [27]-[29], in which a dashpot is used to account for the energy dissipation caused by plastic deformation. The advantages of the spring-dashpot model are that they are simple and direct to implement. But in this model, the dashpot coefficient and the relative velocity in a collision influence highly the energy dissipation. In addition, it is hard to estimate the energy dissipation for this model, *a priori*.
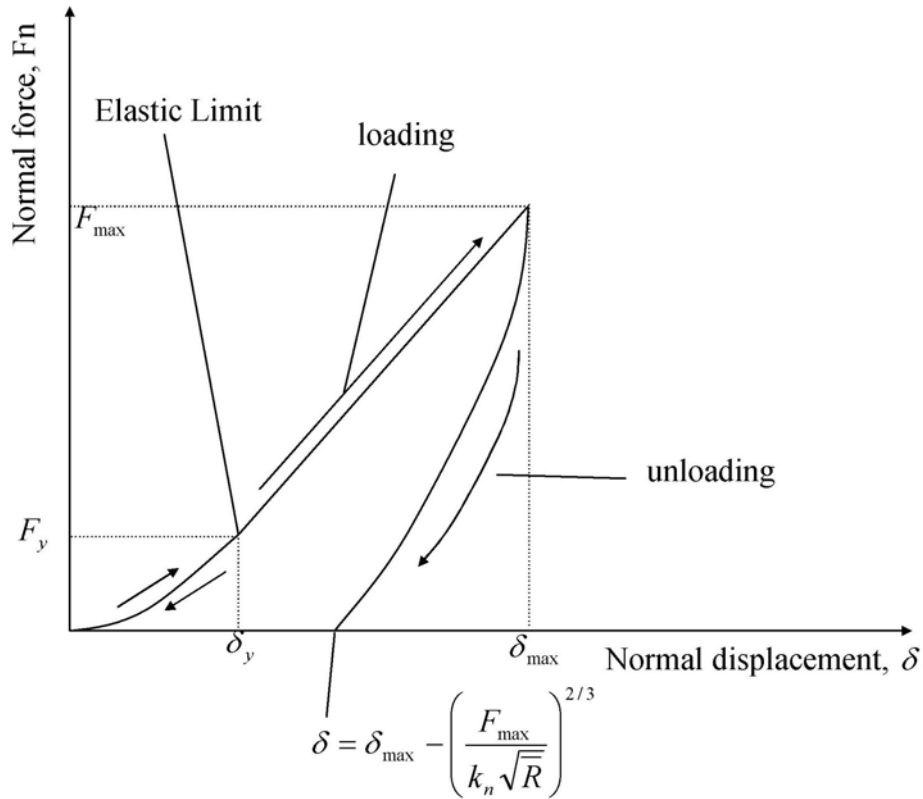
Figure 2.6 The Normal Force-Normal Displacement characteristics

2.3 Methods of Contact Detection

In order to apply the contact force models to multi-particle DEM simulations, it is necessary to determine whether particles are in contact with each other, and how many particles are in contact for each time step in a given system. Since contact detection will take a considerable proportion of the total CPU time that is required to analyze the whole problem, an efficient and robust contact detection algorithm is very important when implementing the simulation.

2.3.1 Brute Force Approach

　　Brute force is a straightforward approach to detect whether particles contact each other. It is based on a test between each particle and all other particles with a lower index number. Figure 2.7 shows the search mechanism for the brute force approach.
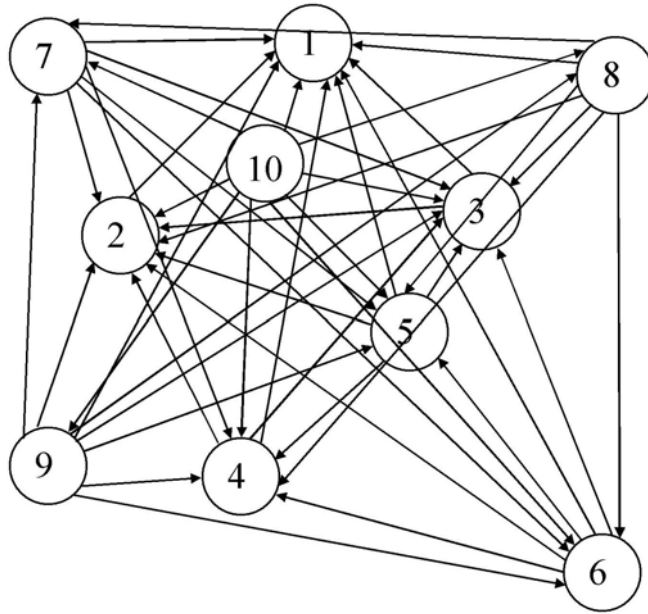
Figure 2.7 The schematic diagram of the brute force approach

　　From Figure 2.7, it is clear that if there are N particles in the system, there are $0.5 \times N \times (N-1)$ pairs which are tested for contact. So the brute force approach is a simple, intuitive, and spontaneous method which is useful for small domains. However, when a large number of particles are involved, the logical testing of every pair in the particulate system is usually very inefficient.

2.3.2 Cell Index Method

　　The Cell Index method is an approach for keeping track of neighbors for large particulate systems [7]-[8], [30]. In this method, the region being modeled is divided into $M \times M \times M$ cells

for a three-dimensional representation. The value of M is chosen based on the principle in which the side of cell $l = L/M$ is greater than the cutoff distance for the force, which was defined by Verlet [31]. Here L is the principal length of the region being modeled. To understand better this method, a two-dimensional representation is shown in Figure 2.8.

21	22	23	24	25
16	17	18	19	20
11	12	13	14	15
6	7	8	9	10
1	2	3	4	5
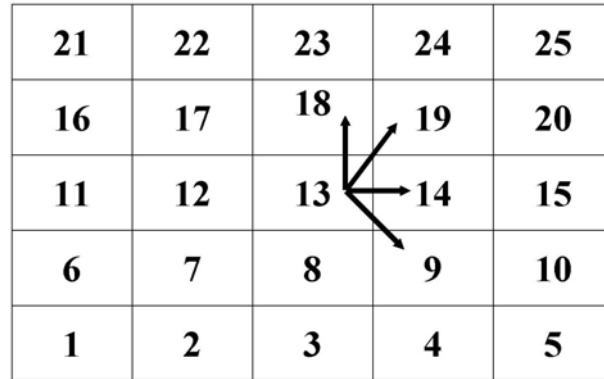
Figure 2.8 The central box is divided into $M \times M$ cells ($M = 5$)

From Figure 2.8, the neighbors of any particle in cell 13 are in the cells 7, 8, 9, 12, 13, 14, 17, 18, 19. Although a particle in cell 13 may contact other particles in the 8 adjacent cells, only particles in cells 9, 14, 18, and 19 are checked, noting that particles in cells 7, 8, 12 and 17 would be automatically checked when each of these cells is the focus of the search. The procedures for this method are:

1.   All particles in the system are sorted into their appropriate cells;

2.   Initially, contacts are tested for all particles in each cell and selected cell neighbors; here detection of multiple particles in a single cell leads to the brute force approach.

Therefore, for the Cell Index method, an appropriate method should first be used to sort all particles into their relative cells. The linked lists method for this application was discussed by Knuth, Hockney and Eastwood, and Allen and Tildesley [7]-[8], [32]. Two arrays, HEAD and LIST, are used in this method. The HEAD array contains one element for each cell which is

used to get the element of the LIST array. Then the element in the LIST array is used as an index to point to the next particle in the cell, and so on. The particles in each cell are sorted from the highest number to the lowest number. For example, in Figure 2.9 there are two cells: and particles 1, 2, 5, 7, 8 are in cell 1 and particles 3, 4, 6, 9 are in cell 2. For this case, HEAD(1) = 8, and HEAD(2) = 10.
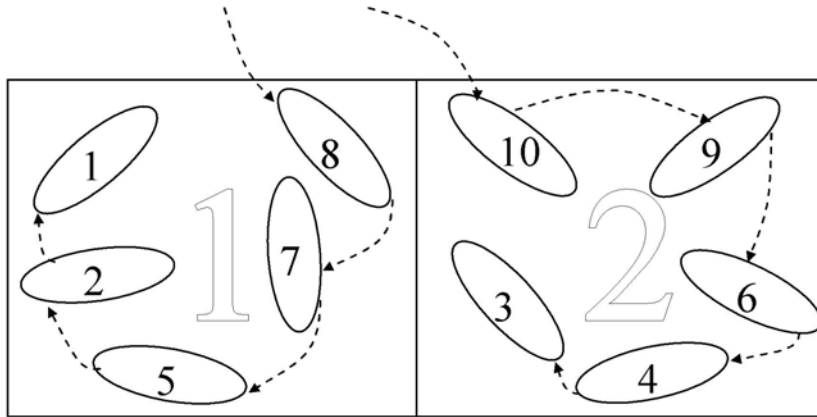
Figure 2.9 A close-up of cells 1 and 2, showing the particles and the link-list structures [7]

The following sequence shows how the particles in cell 2 are sorted in the LIST array:

LIST{HEAD(2)}=LIST(10)=9 (particle 9 is the next highest particle in cell # 2)

LIST{LIST(10)}=LIST(9)=6 (particle 6 is the next highest particle in cell # 2)

LIST{LIST(9)}=LIST(6)=4 (particle 4 is the next highest particle in cell # 2)

LIST{LIST(6)}=LIST(4)=3 (particle 3 is the next highest particle in cell # 2)

LIST{LIST(4)}=LIST(3)=0 (this indicates that there are no more particles in cell # 2)

For this method, there are about $N \times \ln(N)$ pairs which are tested for particle contact.

2.3.3 No Binary Search

The No Binary Search (NBS) method is based on the assumption that each particle can be approximated by a sphere [33]. This method is similar to the Cell Index Method. The cubic

simulation box is also divided into $M \times M \times M$ cells. The linked lists method is also used in NBS. The major difference between these two methods is that the size of the cubic cell is the size of the largest particle for NBS method in the system. From the known information on the center locations of the particles, each particle in the system will be sorted into their cells. And three arrays are used to represent the particles' locations in this system. Then contacts are tested for all particles in any non-empty cell against all particles in neighboring cells. It is noted that no loop over cells is performed in NBS. So the total CPU time needed to perform the contact tests is independent of the number of cells, and is proportional to the total number of particles, i.e, $T_t \propto N$. Here T_t is total detection time, and N is the total number of particles in the system.

In summary, for the above mentioned three contact detection algorithms, the relationships between the total detection time and the total number of particles in the system are:

$$\begin{cases} T_t \propto N^2 & \text{Brute Force} \\ T_t \propto N \ln(N) & \text{Cell Index} \\ T_t \propto N & \text{No Binary Search} \end{cases}$$

Figure 2.10 shows the relationships between total detection time and total particle number for the three contact detection algorithms.
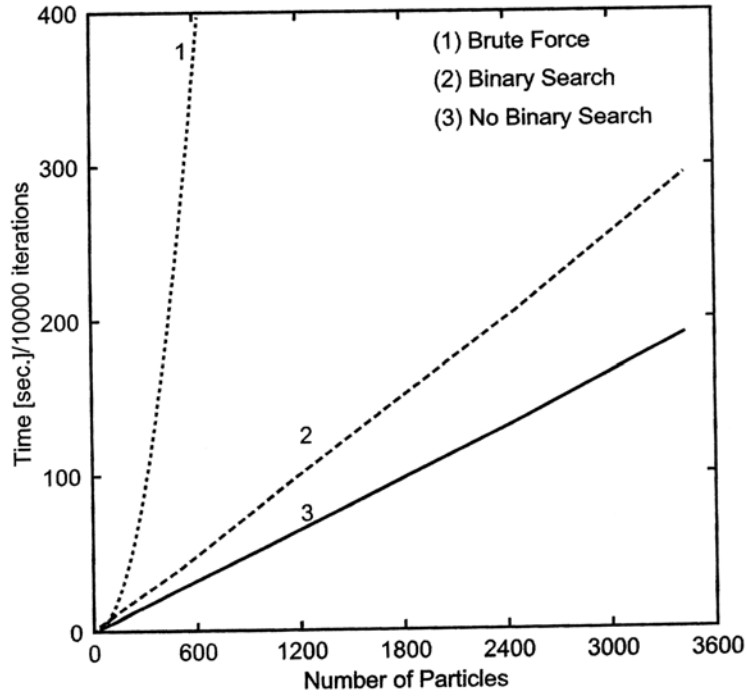
Figure 2.10 Comparison of three contact detection algorithms (McCarthy [34])

2.4 Orientation with Quaternions

In many fields of mechanics, Euler angles are used to represent the rotation of a rigid body. The basic idea of Euler angles is that any rotation can be separated into a series of three rotations about the major axes. Thus, a rotation matrix is used to specify the orientation of a rigid body between global and local coordinates. The relationship of one vector in the global system, e^s, with the same vector in the local system, e^b, is

$$e^b = A_R \cdot e^s \qquad (2.45)$$

where A_R is the rotation matrix.

Figure 2.11 shows the definition of Euler angles (ϕ, θ, ψ) in a suitable convention [7], [35]. For this definition of Euler angles, the rotation matrix A_R is:
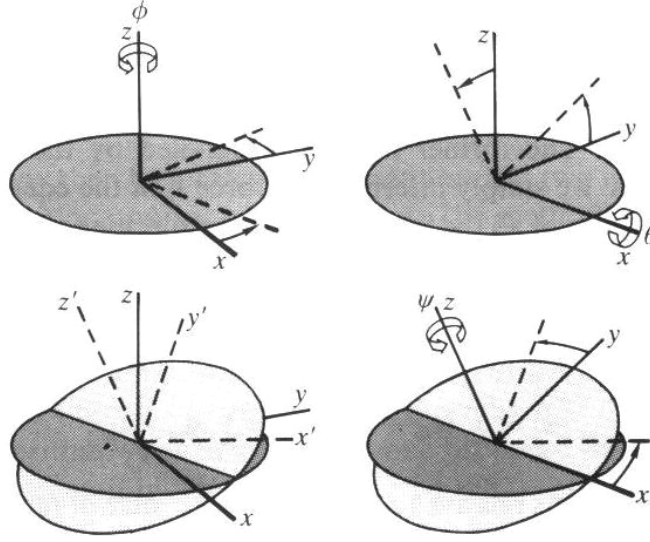
Figure 2.11 Definition of Euler angles ([7])

$$A_R = \begin{bmatrix} \cos\phi\cos\psi - \sin\phi\cos\theta\sin\psi & \sin\phi\cos\psi + \cos\phi\cos\theta\sin\psi & \sin\theta\sin\psi \\ -\cos\phi\sin\psi - \sin\phi\cos\theta\cos\psi & -\sin\phi\sin\psi + \cos\phi\cos\theta\cos\psi & \sin\theta\cos\psi \\ \sin\phi\sin\theta & -\cos\phi\sin\theta & \cos\theta \end{bmatrix} \quad (2.46)$$

From Eq. 2.45, it is clear that for transformation of vectors in global and local coordinates, the inverse of rotation matrix, A_R, is required. But from Eq. 2.46, when θ is equal to $\pm\pi/2$, the determinant of A_R is zero. Therefore, the inverse of A_R does not exist and the singularity of the transformation occurs. To resolve this singularity, Evans [35] suggested using quaternions to represent the orientations. In fact, quaternions were first mentioned by Hamilton [36] as an extension of complex numbers. A quaternion, Q, is a vector of four scalar coefficients as follow:

$$Q = (q_0, q_1, q_2, q_3) \quad (2.47)$$

Here the magnitude of this quaternion is 1. In the Euler angle convention of Figure 2.11 and Eq. 2.46, Goldstein [37] defined:

$$q_0 = \cos\frac{1}{2}\theta\cos\frac{1}{2}(\phi+\psi)$$

$$q_1 = \sin\frac{1}{2}\theta\cos\frac{1}{2}(\phi-\psi)$$

$$q_2 = \sin\frac{1}{2}\theta\sin\frac{1}{2}(\phi-\psi)$$

$$q_3 = \cos\frac{1}{2}\theta\sin\frac{1}{2}(\phi+\psi)$$

(2.48)

So the rotation matrix becomes

$$A_R = \begin{bmatrix} q_0^2 + q_1^2 - q_2^2 - q_3^2 & 2(q_1q_2 + q_0q_3) & 2(q_1q_3 - q_0q_2) \\ 2(q_1q_2 - q_0q_3) & q_0^2 - q_1^2 + q_2^2 - q_3^2 & 2(q_2q_3 + q_0q_1) \\ 2(q_1q_3 + q_0q_2) & 2(q_2q_3 - q_0q_1) & q_0^2 - q_1^2 - q_2^2 + q_3^2 \end{bmatrix}$$

(2.49)

By using this rotation matrix, there is no problem of singularity in the transformation between global and local systems.

Although the representation by Euler angles is useful and intuitive in some cases, Euler angles have some drawbacks:

- There is no universal standard for Euler rotations;

- Since any rotation can be represented by a matrix, the rotation should be converted between them. However, computing the required angles is time-consuming and can introduce errors;

- It is straightforward to visualize the tablet orientation by the known Euler angles. But in contrast, it is hard to determine Euler angles from any given orientation.

Shoemake [38] gives a new approach to represent the rotations of rigid bodies by a natural extension of quaternions. For computing a rotation about the unit vector, $\hat{u} = (u_x, u_y, u_z)$, by an angle θ, the quaternion is

$$q = (s,v)$$

(2.50)

where

$$s = \cos\frac{\theta}{2}, v = \hat{u}\sin\frac{\theta}{2}$$

For a point p in space, let the quaternion $P = (0, p)$. So the desired rotation of that point is

$$P_{rotated} = qPq^{-1} \tag{2.51}$$

From Eq. 2.50, we can confirm that q is a unit quaternion. So the inverse of q is q', which is the conjugate of quaternion q. Eq. 2.51 becomes

$$P_{rotated} = qPq' \tag{2.52}$$

where $q' = (s, -v)$.

By using the rotation matrix, we can compute P_R in another way

$$P_R = pA_R \tag{2.53}$$

where

$$A_R = \begin{bmatrix} s^2 + u_x^2 - u_y^2 - u_z^2 & 2(u_x u_y + s u_z) & 2(u_x u_z - s u_y) \\ 2(u_x u_y - s u_z) & s^2 - u_x^2 + u_y^2 - u_z^2 & 2(u_y u_z + s u_x) \\ 2(u_x u_z + s u_y) & 2(u_y u_z - s u_x) & s^2 - u_x^2 - u_y^2 + u_z^2 \end{bmatrix}$$

Therefore, when a solid object which has simultaneous rotation about the x, y and z axes is taken into account, this rotation could be represented by a single rotation about the axis which is obtained by normalizing the axis $(\omega_x, \omega_y, \omega_z)$. The rotation angle is the magnitude of the vector $(\omega_x, \omega_y, \omega_z)$ times the time interval dt. Here ω_x, ω_y and ω_z are angular velocities about x, y and z axes respectively.

From the above discussion, compared with Euler's angles, it is much easier to represent the orientation of the rigid body by quaternions. So quaternions will be used to represent the orientation of particles in this research.

2.5 DEM Simulations in a Rotating Drum

Particle diffusion and segregation in a rotating drum were studied using DEM simulations [39]-[40]. Simulation results showed that the DEM method can be used to investigate and interpret complex phenomena, which include disorder, pattern formation, segregation, diffusive motion of particles parallel to the axis of rotation and flowing motion perpendicular to the axis of rotation, of granular flow in a rotating drum. McCarthy and Ottino [41] also studied mixing and segregation of particles in a tumbling mixer. Comparison of results showed good qualitative agreement between experiments and DEM simulations.

Steady particulate flows in a rotating cylinder were investigated using the DEM method and Magnetic Resonance Imaging (MRI) [42]. Periodic boundary conditions in the longitudinal direction were used to reduce the computational time. The DEM simulation was carried out in a 15 mm long, half-filled 6.9 cm diameter cylinder, using a time step of 10^{-4} s. Although good agreement was obtained between simulations and experiments, which included the comparison of dynamic angle of repose, velocity field in a plane perpendicular to the cylinder axis and velocity fluctuations, the experimental and simulation conditions were much different from the typical settings used in pan coating device. In addition, the accuracy of measurement of the dynamic angle of repose was limited since the opening was only about seven particle diameters. Yang et al. [43] also simulated particle flow in a rotating drum filled with 3 mm diameter spheres using the DEM method. The diameter and the thickness of the drum were 100 mm and 16 mm, respectively. Periodic boundary conditions along the axial direction were used to avoid the end wall effect. A Positron Emission Particle Tracking (PEPT) technique was used. Good agreement was obtained in terms of the dynamic angle of repose between simulations and PEPT measurements. However, the disparity for the angular velocity of particles indicated that

DEM simulation may not perfectly represent the PEPT experimental conditions. In addition, the axial motion of particles was not taken into account although DEM data were generated in a three-dimensional simulation.

Although considerable work has been done to investigate particle movement in rotating drums using DEM, there is still a lack of information about particle movement in the spray zone of a typical pan coating device used in the pharmaceutical industry. Most of the earlier simulation work focused on particle mixing, segregation, and agglomeration phenomena rather than considering important issues in a coating process. For a coating process in a pan coating device, information about particle movement in the spray zone is essential in order to predict product uniformity.

In addition, most particulate systems involve the use of non-spherical particles. In particular, the coating processes of standard round and elongated tablets in the pharmaceutical industry is an important unit operation. In order to simulate non-spherical particles, the shape of the particles is usually approximated by spheres, with the same volume as the non-spherical particles, due to its easy implementation in DEM [1]. However, there is a concern about the accuracy of this approximation. Pandey and Turton [2] showed that the dynamic angles of repose and average surface velocities were much higher for tablets than for spheres when using video-imaging techniques to study the movement of different shaped particles, even though the volume of tablets and spheres were the same. Therefore, a more realistic shape description for non-spherical particles should be used to obtain more accurate simulation results.

Along with the increase in CPU speed and distributed computing techniques, non-spherical particles such as ellipsoidal, polyhedral, superquadric, multi-sphere particles, and digitized representations have been modeled in three-dimensional DEM simulations [44]-[51]. Due to

the complex contact detection algorithms for these non-spherical particles, it is extremely computationally expensive to implement the DEM simulations for systems with a large number of particles. Recently, some efficient contact detection algorithms for non-spherical particles have been developed [52]-[54]. Generally, to simplify the problem of detecting contacts between non-spherical particles, the shape of non-spherical particles is approximated by a cluster of identical spheres. Using multi-sphere representations for non-spherical particles, the geometric packing of particles of various shapes were simulated and good agreement was obtained with analytical results from the Carnahan-Starling and Boublik-Mansoori equations [49]. In addition, Gan et al. [50] used DigiPac simulations, which is a new, digital packaging algorithm based on the digitized representations of particles' shapes by pixels (in 2D) or voxels (3D), to investigate the packing densities of non-spherical particles. There was no explicit consideration of particle interactions in DigiPac simulations. Comparison of packing densities from DigiPac simulations with experiments and other published data showed good agreement in all cases.

For equipment such as pan coating devices, not only is the packing density important in the non-cascading portion of particle bed, but also the accurate modeling of the dynamic behavior of particle movement in the cascading layer is essential to obtain good results for a coating process. Since particle interactions in DigiPac simulations were not taken into account, it can not be used to study the dynamic behavior of particulate flow in the pan coating devices. For multi-sphere representations, it seems that good results can be obtained for the study of packing densities of non-spherical particles. However, the key concern of this research is the accuracy of simulation for dynamic behavior of particle movement in pan coating devices.

2.6 Modeling of Liquid Bridge Forces

Liquid solutions are used for coating and wet granulation processes in the pharmaceutical industry. In order to model these processes using DEM, when a liquid bridge is formed between two particles, the effect of the liquid bridging on the particle movement must be taken into account. Figure 2.12 shows the liquid bridges formed in the gap between particles.
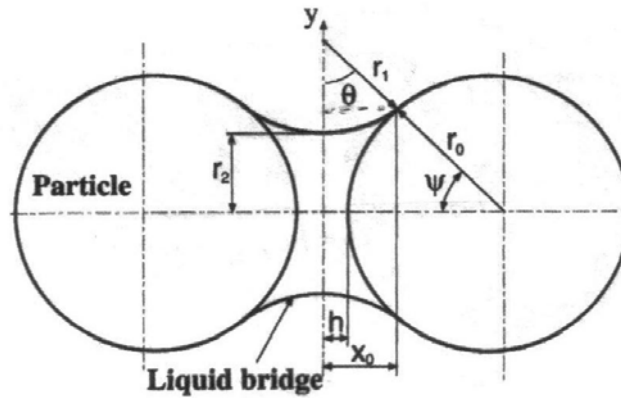
Figure 2.12 Liquid bridges formed between particles [55]

Generally, there are two kinds of forces caused by the liquid bridge. One is the adhesive force, which arises from capillary and surface tension effects. The other is a viscous force, which is dependent on the viscosity of the liquid.

Based on the assumption that the shape of the liquid bridge between two particles may be approximated by an arc of a circle, Fisher [56] gave the adhesive force as follows:

$$f_L = \pi r_2^2 \gamma \left(\frac{1}{r_1} - \frac{1}{r_2} \right) + 2\pi r_2 \gamma \tag{2.54}$$

where γ is the surface tension of liquid, and r_1, r_2 are the radii of curvature of liquid bridge surfaces, and they are defined in Figure 2.12. The first term on the right hand side of Eq. 2.54 is due to the pressure deficiency across the air-liquid interface. The second term arises from the surface tension of the liquid.

Muguruma et al. [55] provided the numerical solution of the Young-Laplace equation to calculate the radii of the curvature of the liquid bridge. The contact angle was assumed to be zero. Curvature of the liquid bridge can be determined if the volume of the bridge and the length of the gap between particles are known. It should be noted that there is a limit to the length of the gap between particles in which the liquid bridge is formed. Calculation of this limit is also provided by Muguruma et al. [55].

In addition to the capillary force, "wet" particles also encounter a viscous force resisting their motion. Viscous force can be predicted using lubrication theory. In fact, there are two components of the viscous force, one in the normal and one in the tangential direction. The expression of the viscous force in the normal direction between two particles was given by [57]:

$$F_{V_n} = 6\pi\mu R^* v_n \frac{R^*}{S}$$ (2.55)

where R^* is defined as:

$$\frac{1}{R^*} = \frac{1}{R_1} + \frac{1}{R_2}$$ (2.56)

here μ is the viscosity of the interstitial fluid, v_n is the relative normal velocity of the spheres, R_1 and R_2 are the radii of the two particles, respectively, and S is the separation between particles.

The viscous force in the tangential direction was predicted by [57]:

$$F_{Vt} = \left(\frac{8}{15}\ln\frac{R^*}{S} + 0.9588\right) \times 6\pi\mu R^* v_t$$ (2.57)

where v_t is the relative tangential velocity of the particles

From Eq. 2.55, the viscous force in the normal direction is arbitrarily large for arbitrarily small separation distances between two particles. Hence, a restriction should be applied while

using Eqs. 2.55 and 2.57 in the simulations. In the current study, S_C, called the limiting separation distance, will be introduced in the liquid viscous force model. When the separation distance of two tablets is less than S_C or the two tablets contact each other, S in Eqs. 2.55 and 2.57 will be replaced by S_C to predict the viscous force in the simulations. S_C will be determined based on the comparison between experiments and simulations for the collision of two tablets.

2.7 Objectives of the Research

Since standard round tablets are widely used in the pharmaceutical industry, these tablets will be selected as the non-spherical particles in this research. In order to simulate tablet movement in rotating drums using DEM, a representation method of the shape of the standard round tablets will be proposed, and then the contact algorithms will be developed based on this representation.

In addition, a high speed digital imaging system will be used to validate this representation method through the comparison of experiments and DEM simulations. The efficiency and accuracy of this representation will also be studied by using a different representation method for non-spherical particles. Since coating solutions are used in coating processes, the effect of liquid bridging between tablets on tablet movement will be investigated through DEM.

Finally, multi-particle simulations using spheres and tablets in the rotating drums will be studied. Dynamic behavior of particle flow in the rotating drums will be compared with experimental data.

3. Experimental Methods and Implementation Procedure

3.1 High speed digital imaging system

In the current research, a MotionPro high speed digital imaging system from Redlake MASD, Inc. was used to record the images of tablet-plane contact and tablet-tablet contact. This system includes a mega-pixel resolution SMOS PCI camera, PCI camera control, and a memory board with up to 65.4 s of record time at 25 frames per second. The maximum frame rate is 2000 frames per second. Images will be quantitatively analyzed by using the spreadsheet analysis module (Redlake MiDAS) included in the high speed digital imaging system. Figure 3.1 shows the schematic diagram of the high speed digital imaging system.

Figure 3.1 Schematic diagram of the high-speed digital imaging system

Figure 3.2 shows a series of successive images of a tablet hitting a stationary tablet affixed to a solid surface from the high speed digital imaging system.

(1)   (2)   (3)   (4)

(5)   (6)   (7)   (8)

(9)   (10)   (11)   (12)

(13)   (14)   (15)   (16)
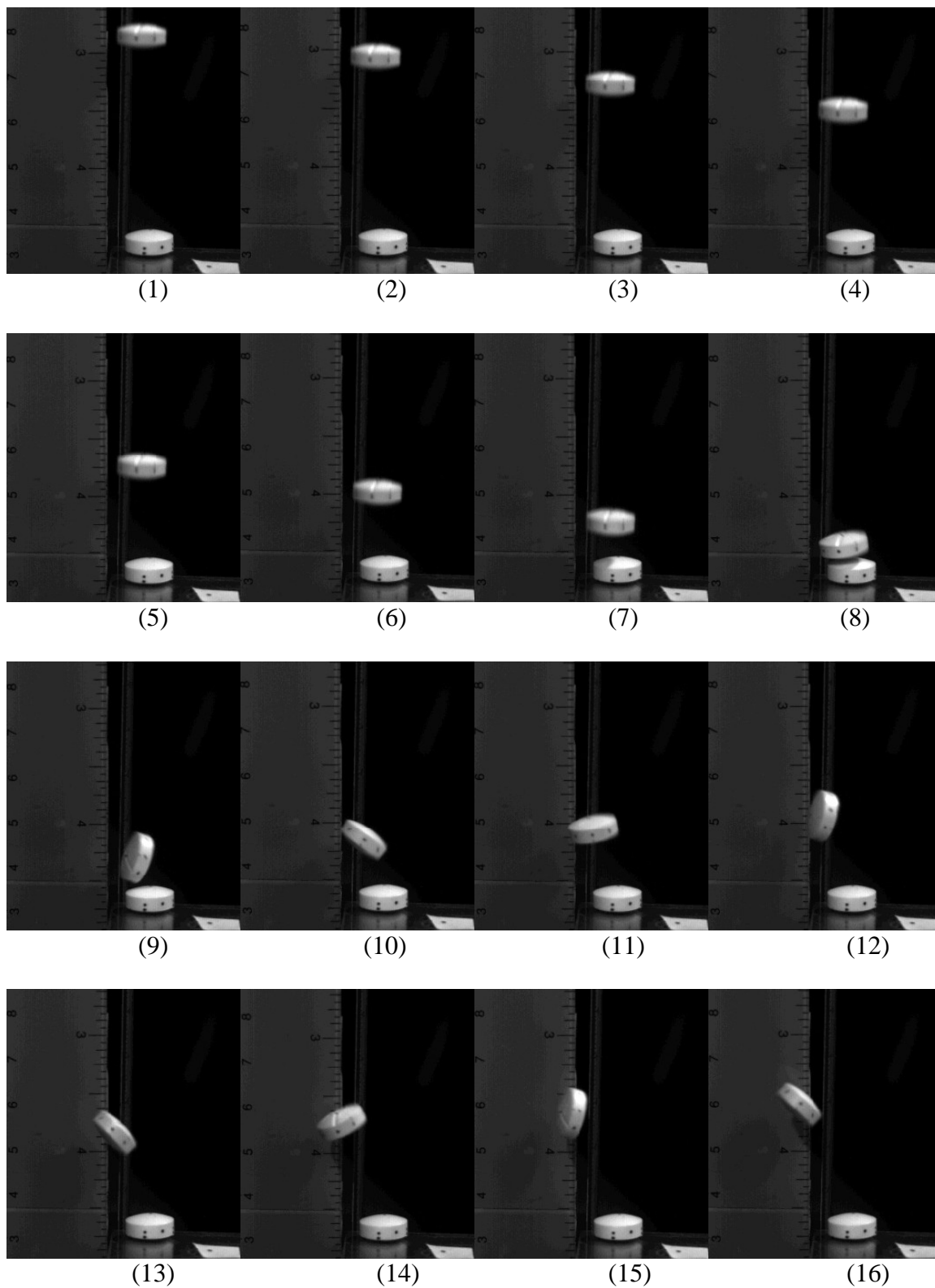
Figure 3.2 A series of successive images of tablet-hitting-tablet from the high speed digital imaging system. (The time interval between two images is 5 ms)

34

In Figure 3.2, the time interval between two images is 5 ms. By using the spreadsheet analysis module in the high speed digital imaging system, the locations of the marked points on the surface of the tablet may be obtained. Then the center locations and orientation of the tablets are found from the geometry of the tablets. Finally, the linear velocities of the tablets can be calculated based on the center locations of the tablets at different images. The angular velocity of the tablet can be obtained through tracking the locations of the marked points on the surface of the tablet for different recorded images.

As mentioned in Section 2.2, the coefficient of restitution used in the normal contact force models should be known in order to implement these models in DEM simulations. If there is a linear relationship between normal force and normal displacement for loading and unloading, the coefficient of restitution is equal to $(1 - \text{relative energy loss for a single contact})^{1/2}$. Therefore, the coefficient of restitution for particle contact can be estimated by using the high speed digital imaging system.

In this experiment, the movement of a free falling particle and its rebound from a flat surface is recorded using the imaging system at different initial heights. The linear and angular velocities of the particles before and after contact can be calculated using the spreadsheet analysis module. The relative energy loss for a single contact may thus be obtained. Finally, the coefficient of restitution is determined based on the relative energy loss for a single contact of the particle.

In addition, the high speed digital imaging system can also be used to investigate the effect of liquid bridging, between two tablets, on the dynamic behavior of tablet-tablet contact. Thin films of liquids, with different viscosities, will be applied to the surface of the tablet. Quantitative analysis of these images, obtained by using this imaging system will provide

important information to determine the parameters used in the viscous force models for DEM simulations. Figure 3.3 shows the images of tablet-tablet contact using different viscous liquids.

3.2 Micro-Hardness Tester

In order to implement the contact force models in the DEM simulations, some physical properties of particles such as Young's modulus, hardness, etc., must be known in order to predict the values of the parameters used in the contact force models. In practice, tablets used in the pharmaceutical industry are composed of many ingredients. Therefore, it is very difficult to predict, *a priori*, the physical properties of tablets. Fortunately, micro indentation studies can be used to estimate the values of some parameters in the contact force models. Tablets used in this work were analyzed using a micro-hardness tester (MHT) and performed by Micro Photonics Inc., Irvine, CA [58].

In the MHT method, an indenter tip with a known geometry is driven into a specific site of the material to be tested by applying a gradually increasing normal loading force. When a pre-set maximum value is obtained, the loading force is reduced until partial or complete relaxation occurs. The position of the indenter relative to the sample surface is precisely monitored with a differential capacitive sensor during the experiment.

For each loading/unloading cycle, the indentation curve, which is obtained by plotting the loading forces with the corresponding position of the indenter, provides the mechanical properties of the material under test. Finally, established models are used to analyze the indentation curve and obtain quantitative hardness and modulus values for this kind of material. The MHT method is especially useful for loading and penetration depth measurement at micrometer length scales.

	t = 0		t = 0
	t = 0.014 s		t = 0.014 s
	t = 0.028 s		t = 0.028 s
	t = 0.042 s		t = 0.042 s
	t = 0.056 s		t = 0.056 s
(A)		(B)	(C)
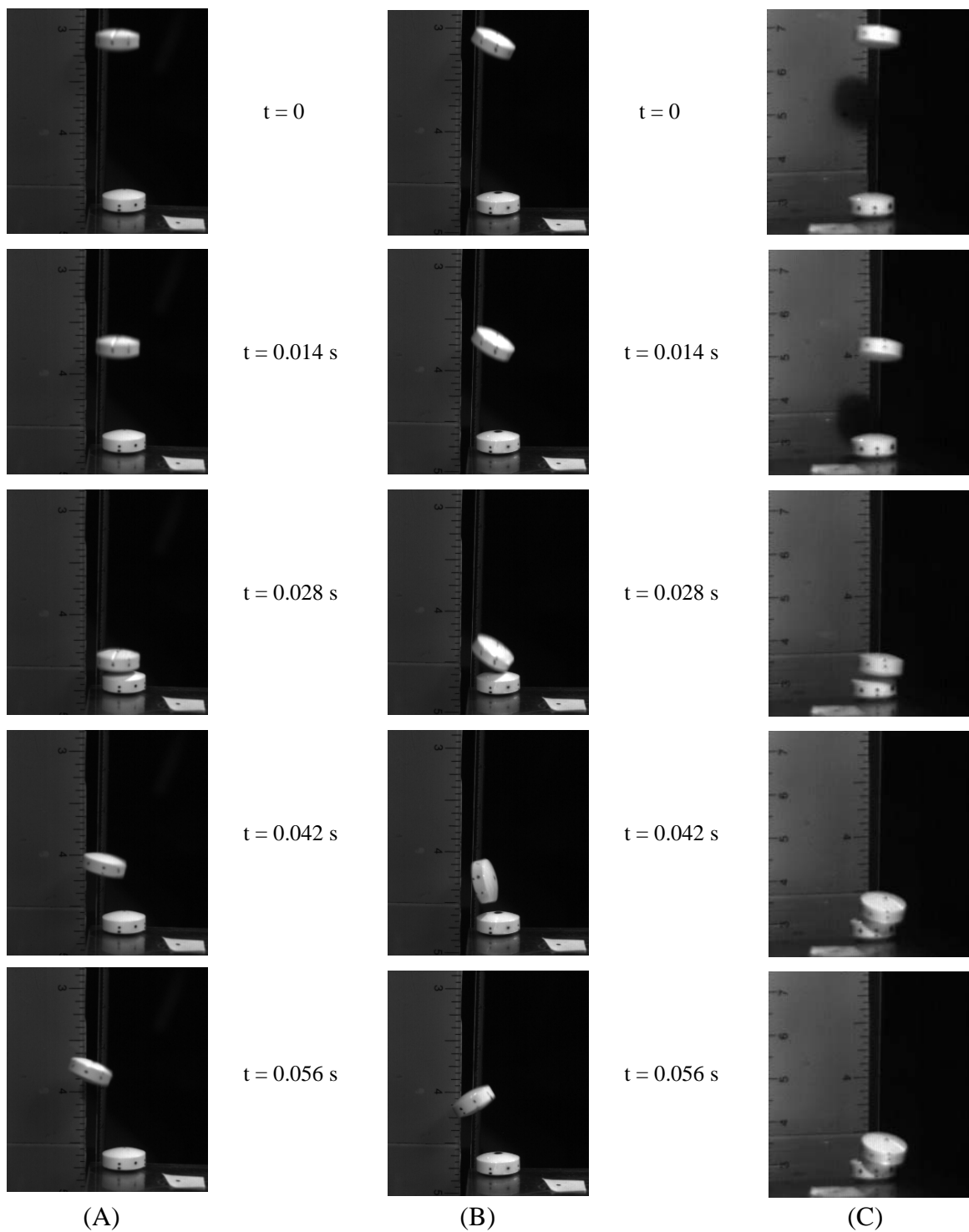
Figure 3.3 A series of successive images of tablet-tablet contact using different viscous silicone oils from the high speed digital imaging system. (A) No silicone oil is applied on the surface of two tablets; (B) Silicone oil with viscosity of 134 cps is applied on two tablets; (C) Silicone oil with viscosity of 1000 cps is applied

Figure 3.4 shows one typical indentation curve obtained by applying a maximum load force of around 80 mN to a 13/32" standard round cellulose tablet through a MHT [58]. The indenter type used in this MHT is a SS ball with a diameter 1.5 mm. The contact stiffness S, given by the derivative at peak load, shown in Figure 3.4, is determined after correction for thermal drift.
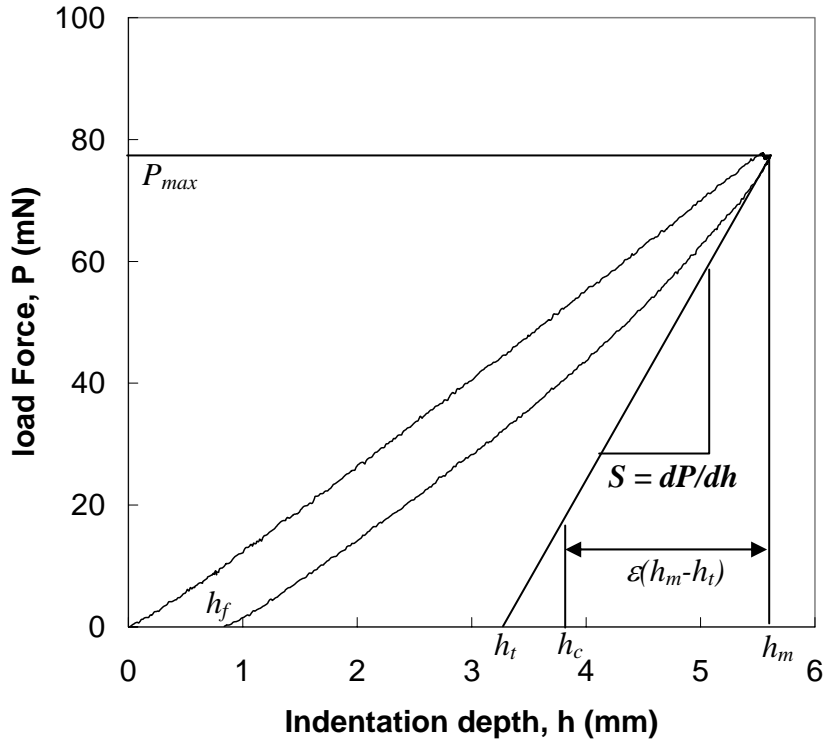
Figure 3.4 The relationship of load force with the corresponding indentation depth

From Figure 3.4, by fitting the upper 80% of the unloading data, the following fitting equation is obtained:

$$P = P_{\max}\left(\frac{h - h_0}{h_m - h_0}\right)^n \tag{3.1}$$

So

$$S = \left(\frac{dP}{dh}\right)_{\max} = nP_{\max}\left[\frac{(h_m - h_0)^{n-1}}{(h_m - h_0)^n}\right] = nP_{\max}(h_m - h_0)^{-1} \tag{3.2}$$

and the tangent depth, h_t, and the contact depth, h_c are

$$h_t = h_m - \frac{P_m}{S}, \; h_c = h_m - \varepsilon(h_m - h_t) \tag{3.3}$$

where ε depends on the power law exponent, n.

Table 3.1 gives some values of these two parameters for different indenter geometries.

Table 3.1 Some values of ε and n for different indenter geometries [58]

Elastic indentation Behavior (indenter geometry)	n (power law exponent)	ε
Flat	1	1
Paraboloid	1.5	0.75
Conical	2	0.72

So the reduced modulus, E_r, is

$$E_r = \frac{\sqrt{\pi}}{2} \frac{S}{A_C} \tag{3.4}$$

where A_c is the projected contact area.

Therefore, the Young's modulus, E, of the tested material can be obtained by

$$\frac{1}{E_r} = \frac{1-v^2}{E} + \frac{v_i^2}{E_i} \tag{3.5}$$

where E_i and v_i are the Young's modulus and Poisson coefficient of the indenter and v the Poisson coefficient of the tested sample.

And the hardness of the tested sample is

$$H = \frac{P_{max}}{A_c} \tag{3.6}$$

3.3 The procedure for implementation of DEM

The main procedures for implementing the DEM method include:

- Representation of the tablet-shaped bodies;

- Contact detection algorithms for these tablet-shaped bodies;

- Selection of appropriate force displacement models;

- Visualization of the movement during tablet-tablet contact movement.

Figure 3.5 shows a schematic diagram of the DEM implementation.
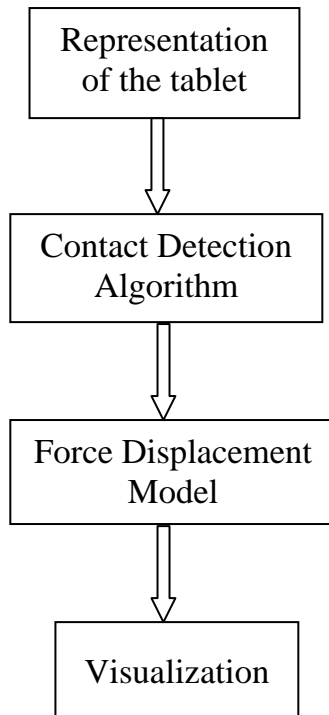
Figure 3.5 Schematic diagram of the DEM implementation

3.4 Definitions of parameters

In the DEM simulation of particle motion in a rotating drum, the main characteristic parameters used to describe particle movement are introduced as follows:

- Dynamic angle of repose (θ): This is the angle between a horizontal line and the slope or surface of the particle bed in a rotating drum, as the drum rotates. Generally, the slope or surface of the bed is not a perfect straight line. The side view of particle movement in a rotating drum using DEM is shown in Figure 3.4. Figure 3.4 shows how to estimate the dynamic angle of repose.

- Cascading Surface Velocity (V_y): This refers to the velocity of particles moving downward in the surface of the cascading layer. As shown in Figure 3.6, y axis is the direction of particle movement in the drum.
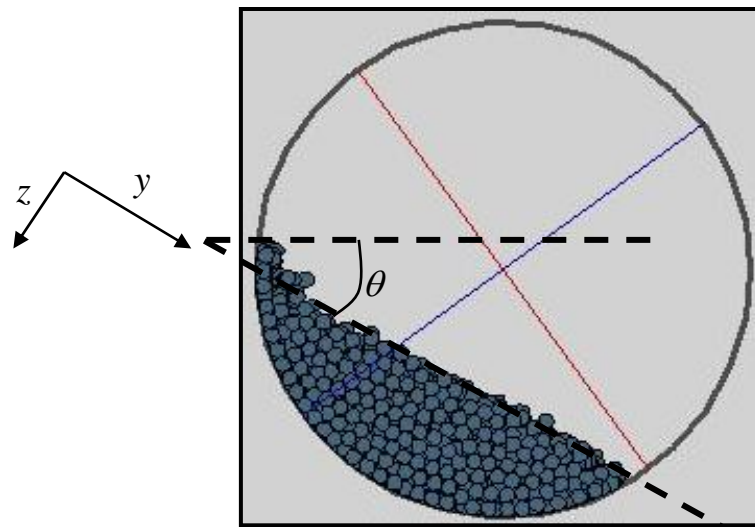
Figure 3.6 The schematic diagram to calculate the dynamic angle of repose in the DEM simulations

4. Simulation and Experimental Results

4.1 Representation of Tablet Shape

In this research work, the intersection of just three spheres is used to represent accurately the shape of a typical round tablet as shown in Figure 4.1 [59].
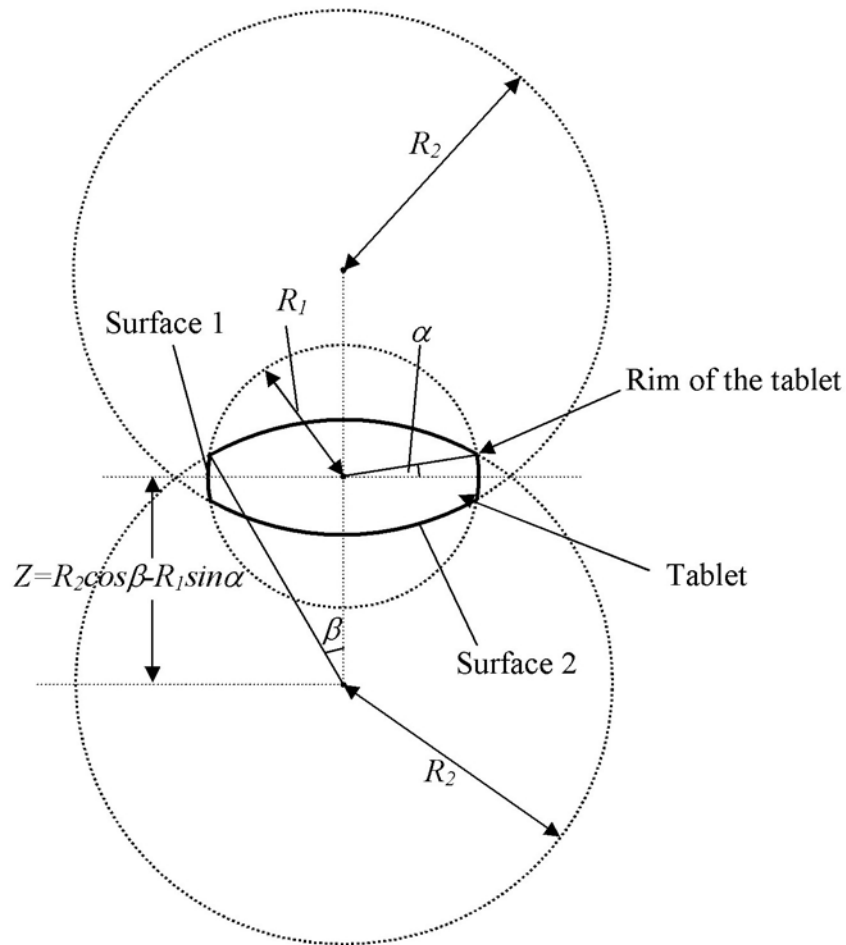
Figure 4.1 Representation of tablet's shape using three spherical surfaces [59]

In Figure 4.1, several parameters are used to define the shape of the tablets. R_1 and R_2 are the radii of the spheres, which are used to represent the shape of the tablet. Z is the distance from the center of the larger sphere to the center of the tablet. α and β are the angles as

defined in Figure 4.1. The values of these parameters can be determined by knowing the dimensions of the tablet as shown in Figure 4.2.
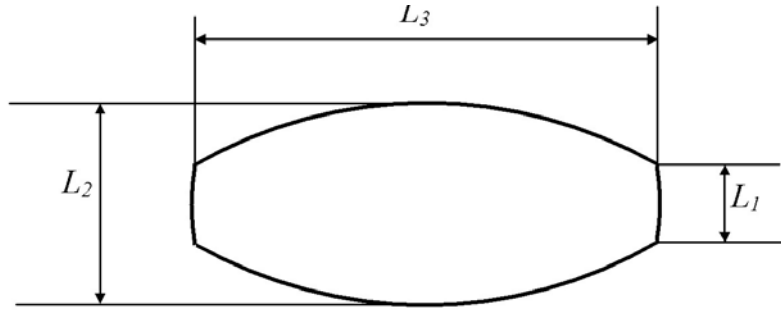
Figure 4.2 Three dimensions of one kind of standard round tablet [59]

From Figures 4.1 and 4.2, we have

$$R_1 = \sqrt{(L_3/2)^2 + (L_1/2)^2} \tag{4.1}$$

$$\tan \alpha = \frac{L_1}{L_3} \Rightarrow \alpha = \tan^{-1} \frac{L_1}{L_3} \tag{4.2}$$

$$2R_2 \sin \beta = L_3 \tag{4.3}$$

$$R_2 - R_2 \cos \beta = \frac{1}{2}(L_2 - L_1) \tag{4.4}$$

$$Z = R_2 \cos \beta - R_1 \sin \alpha \tag{4.5}$$

When the shape of the tablet is determined by the parameters illustrated in Figure 4.1, the volume of the tablet and the moments of inertia based on the three axes shown in Figure 4.3 are given by:

$$V = \iiint_{\Omega} dxdydz$$

$$= 2\int_0^{R_1 \sin \alpha} dz \iint_{x^2+y^2=R_1^2-z^2} dxdy + 2\int_{R_1 \sin \alpha}^{R_2-Z} dz \iint_{x^2+y^2=R_2^2-(z+Z)^2} dxdy$$

$$= 2\int_0^{R_1 \sin \alpha} \pi\left(R_1^2 - z^2\right)dz + 2\int_{R_1 \sin \alpha}^{R_2-Z} \pi\left(R_2^2 - (z+Z)^2\right)dz$$

$$= 2\pi\left(R_1^2 \cdot z - \frac{1}{3}z^3 \right)\Bigg|_0^{R_1 \sin \alpha} + 2\pi\left(R_2^2 \cdot z - \frac{1}{3}(z+Z)^3 \right)\Bigg|_{R_1 \sin \alpha}^{R_2-Z}$$

$$V = 2\pi R_1^3\left(\sin \alpha - \frac{1}{3}\sin^3 \alpha \right) + 2\pi R_2^3\left(\frac{2}{3} - \cos \beta + \frac{1}{3}\cos^3 \beta \right) \tag{4.6}$$

So

$$\rho = \frac{m}{V} \tag{4.7}$$
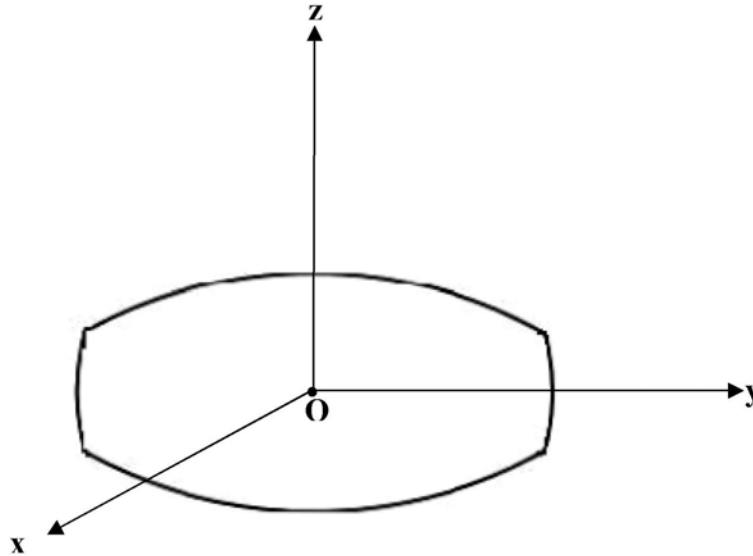
Figure 4.3 Schematic diagram of tablet initial position in Cartesian coordinates

$$I_z = \iiint\limits_{\Omega} \rho\left(x^2 + y^2\right) dxdydz$$

$$= \rho\iiint\limits_{\Omega} x^2 dxdydz + \rho\iiint\limits_{\Omega} y^2 dxdydz$$

$$= 2\rho\iiint\limits_{\Omega} x^2 dxdydz$$

Let $S \equiv \iiint\limits_{\Omega} x^2 dxdydz$, so

$$S \equiv \iiint\limits_{\Omega} x^2 dxdydz = 2\int_0^{R_1\sin\alpha} dz \iint\limits_{x^2+y^2=R_1^2-z^2} x^2 dxdy + 2\int_{R_1\sin\alpha}^{R_2-Z} dz \iint\limits_{x^2+y^2=R_2^2-(z+Z)^2} x^2 dxdy$$

$$\because \quad \iint\limits_{x^2+y^2=b^2} x^2 dxdy = 4\int_0^b x^2 dx \int_0^{\sqrt{b^2-x^2}} dy = 4\int_0^b x^2\sqrt{b^2-x^2}\, dx = \frac{\pi}{4}b^4$$

So

$$S \equiv \iiint\limits_{\Omega} x^2 dxdydz = 2\int_0^{R_1\sin\alpha} dz \iint\limits_{x^2+y^2=R_1^2-z^2} x^2 dxdy + 2\int_{R_1\sin\alpha}^{R_2-Z} dz \iint\limits_{x^2+y^2=R_2^2-(z+Z)^2} x^2 dxdy$$

$$= 2\int_0^{R_1\sin\alpha} \frac{\pi}{4}\left(R_1^2 - z^2\right)^2 dz + 2\int_{R_1\sin\alpha}^{R_2-Z} \frac{\pi}{4}\left(R_2^2 - (z+Z)^2\right)^2 dz$$

$$= \frac{\pi}{2}\left(R_1^4 \cdot z - \frac{2}{3}R_1^2 \cdot z^3 + \frac{1}{5}z^5\right)\Bigg|_0^{R_1\sin\alpha} + \frac{\pi}{2}\left(R_2^4 \cdot z - \frac{2}{3}R_2^2 \cdot (z+Z)^3 + \frac{1}{5}(z+Z)^5\right)\Bigg|_{R_1\sin\alpha}^{R_2-Z}$$

$$S = \frac{\pi}{2}R_1^5\left(\sin\alpha - \frac{2}{3}\sin^3\alpha + \frac{1}{5}\sin^5\alpha\right) + \frac{\pi}{2}R_2^5\left(\frac{8}{15} - \cos\beta + \frac{2}{3}\cos^3\alpha - \frac{1}{5}\cos^5\alpha\right)$$

So

$$I_z = 2\rho S$$

$$I_z = \pi\rho\left[R_1^5\left(\sin\alpha - \frac{2}{3}\sin^3\alpha + \frac{1}{5}\sin^5\alpha\right) + R_2^5\left(\frac{8}{15} - \cos\beta + \frac{2}{3}\cos^3\beta - \frac{1}{5}\cos^5\beta\right)\right] \quad (4.8)$$

$$I_x = \iiint_\Omega \rho\left(y^2 + z^2\right) dxdydz$$

$$= \rho\iiint_\Omega y^2 dxdydz + \rho\iiint_\Omega z^2 dxdydz = \frac{I_z}{2} + \rho\iiint_\Omega z^2 dxdydz$$

Let $M \equiv \iiint_\Omega z^2 dxdydz$, so

$$M \equiv \iiint_\Omega z^2 dxdydz$$

$$= 2\int_0^{R_1\sin\alpha} z^2 dz \iint_{x^2+y^2=R_1^2-z^2} dxdy + 2\int_{R_1\sin\alpha}^{R_2-Z} z^2 dz \iint_{x^2+y^2=R_2^2-(z+Z)^2} dxdy$$

$$= 2\int_0^{R_1\sin\alpha} \pi\left(R_1^2 - z^2\right)\cdot z^2 dz + 2\int_{R_1\sin\alpha}^{R_2-Z} \pi\left(R_2^2 - (z+Z)^2\right)\cdot z^2 dz$$

$$= 2\pi\left(\frac{1}{3}R_1^2\cdot z^3 - \frac{1}{5}z^5\right)_0^{R_1\sin\alpha} + 2\pi\left(\frac{1}{3}R_2^2\cdot z^3 - \frac{1}{5}z^5 - \frac{Z}{2}z^4 - \frac{Z^2}{3}z^3\right)_{R_1\sin\alpha}^{R_2-Z}$$

$$M \equiv 2\pi R_1^5\left(\frac{1}{3}\sin^3\alpha - \frac{1}{5}\sin^5\alpha\right)$$
$$+ 2\pi\left[-\frac{1}{5}\left((R_2-Z)^5 - R_1^5\sin^5\alpha\right) - \frac{Z}{2}\left((R_2-Z)^4 - R_1^4\sin^4\alpha\right) + \frac{1}{3}\left(R_2^2 - Z^2\right)\left((R_2-Z)^3 - R_1^3\sin^3\alpha\right)\right]$$

So,

$$I_x = \frac{I_z}{2} + \rho\cdot M$$

$$= \frac{\pi\rho}{2}\left[R_1^5\left(\sin\alpha - \frac{2}{3}\sin^3\alpha + \frac{1}{5}\sin^5\alpha\right) + R_2^5\left(\frac{8}{15} - \cos\beta + \frac{2}{3}\cos^3\beta - \frac{1}{5}\cos^5\beta\right)\right]$$

$$+ 2\pi\rho R_1^5\left(\frac{1}{3}\sin^3\alpha - \frac{1}{5}\sin^5\alpha\right)$$

$$+ 2\pi\left[-\frac{1}{5}\left((R_2-Z)^5 - R_1^5\sin^5\alpha\right) - \frac{Z}{2}\left((R_2-Z)^4 - R_1^4\sin^4\alpha\right) + \frac{1}{3}\left(R_2^2 - Z^2\right)\left((R_2-Z)^3 - R_1^3\sin^3\alpha\right)\right]$$

$$(4.9)$$

From the symmetry of the tablet, the moment of inertia based on the y axis is equal to the moment of inertia based on the x axis, therefore, $I_y = I_x$.

4.2 Contact Detection Algorithm

As shown in Figure 4.1, the surfaces of the tablet are represented by using the intersection of three spherical surfaces. Surface 1 refers to the side surface of tablet whose radius is R_1. Surface 2 is the top and bottom surfaces whose radii are R_2. The rim of the tablet represents the intersectional circle of smaller and larger spheres, which have radii of R_1 and R_2, respectively. Since one objective of this research is to study tablet flow in a rotating drum, the contact forms for Tablet-Flat Surface, Tablet-Curved Surface and Tablet-Tablet contacts should be taken into account. There are three possible contact forms between the tablet and a flat surface, namely, Surface 1-Flat Surface, Surface 2-Flat Surface, and Rim-Flat Surface contacts. Three contact forms also exist for Tablet-Curved Surface contact, which are Surface 1-Curved Surface, Surface 2-Curved Surface, Rim-Curved Surface contacts. In addition, there are six possible interactions between two tablets, which are Surface 1-Surface 1, Surface 1-Surface 2, Surface 2-Surface 2, Rim-Surface 1, Rim-Surface 2 and Rim-Rim contact forms. The contact algorithms for these contact forms are developed in Cartesian coordinates in the following sections. These can be converted into the appropriate vectorial forms through vector manipulations.

4.2.1 Tablet-Flat Surface contact

As shown in Figure 4.1, Surface 1 refers to the smaller surface of the tablet and Surface 2 is the larger surface of the tablet. The circle formed by the intersection of the two spheres represents the rim of the tablet. Therefore, for this contact form, there are three possible contact

forms, which are Surface 1-Flat Surface, Surface 2-Flat Surface and Rim-Flat Surface contacts [59].

4.2.1.1 Surface 1-Flat Surface contact

This contact form is shown in Figure 4.4. R_1 is the radius of the smaller sphere in Figure 4.1. d is the distance from the center of the tablet to the flat surface. For this contact form, the following criteria must be satisfied:

- $90 - \alpha \le \gamma \le 90$
- $d \le R_1$
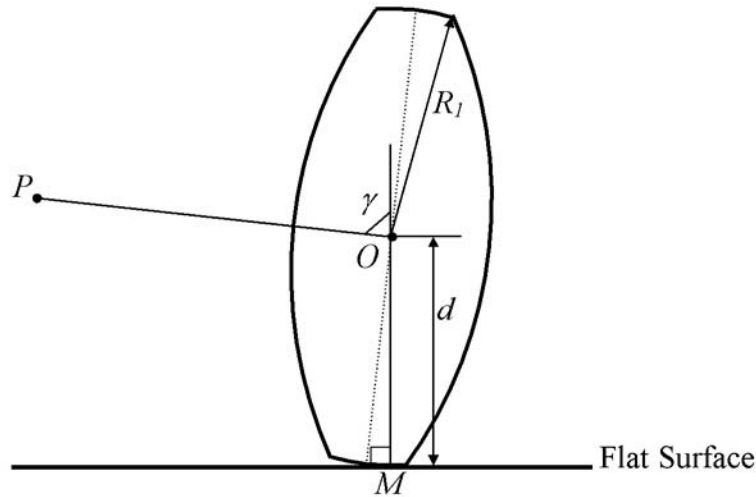
Figure 4.4 Schematic diagram of Surface 1-Flat Surface contact [59]

4.2.1.2 Surface 2-Flat Surface contact

Figure 4.5 shows this kind of contact form. In Figure 4.5, point O is the center of the tablet, and point P is the center of one of the larger spheres determining the shape of the tablet. R_2 is the radius of the spheres mentioned in Figure 4.1, d is the distance from the point P to the Flat Surface, and γ is the angle between two lines, OP and PM.
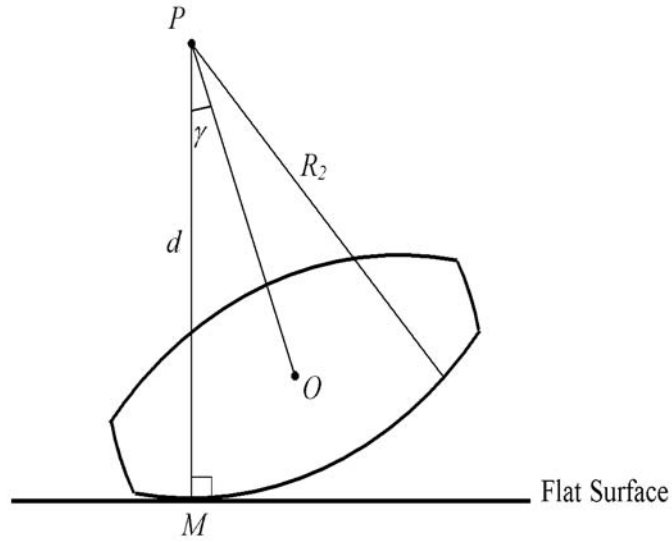
Figure 4.5 Schematic diagram of Surface 2-Flat Surface contact [59]

From Figure 4.5, when the contact form is Surface 2-Flat Surface Contact, the two criteria given below must be satisfied:

- $\gamma \leq \beta$
- $d \leq R_2$

where β is the angle defined in Figure 4.1.

4.2.1.3 Rim-Flat Surface contact

Figure 4.6 shows the Rim-Flat Surface contact form. For this case, S is the point on the rim of the tablet in contact with the flat surface. γ is the angle between two lines, OP and OM .
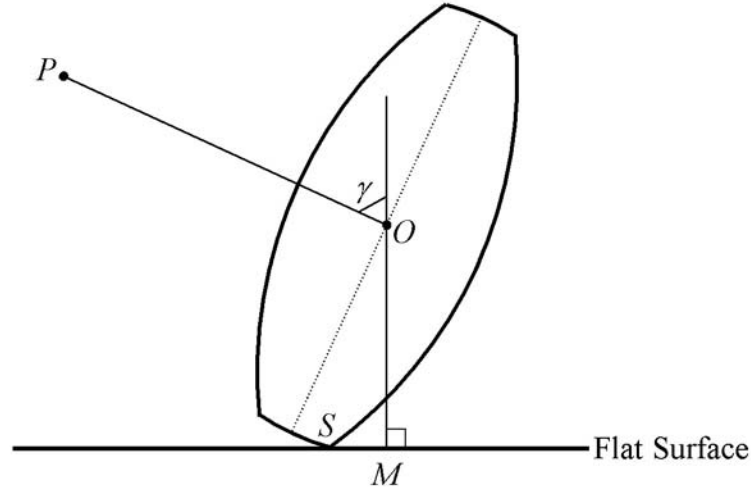
Figure 4.6 Schematic diagram of Rim-Flat Surface contact [59]

The schematic diagram for determining the point S on the rim of the tablet is shown in Figure 4.7. In Figure 4.7, C_R is the center of the rim circle of the tablet. From Figure 4.1, the radius of the rim circle is $R_1 \cos\alpha$. $\vec{U}_1$ is the unit normal vector that passes through the center of the tablet, $\vec{V}_{12}$ is the unit normal vector of the Flat Surface. $\vec{V}_1$ and $\vec{V}_2$ are orthogonal projections of $\vec{V}_{12}$ on $\vec{U}_1$ and on the plane of the rim circle, respectively. These are defined as $\vec{V}_1 = (\vec{U}_1 \cdot \vec{V}_{12})\vec{U}_1$, and $\vec{V}_2 = \vec{V}_{12} - \vec{V}_1$, respectively.
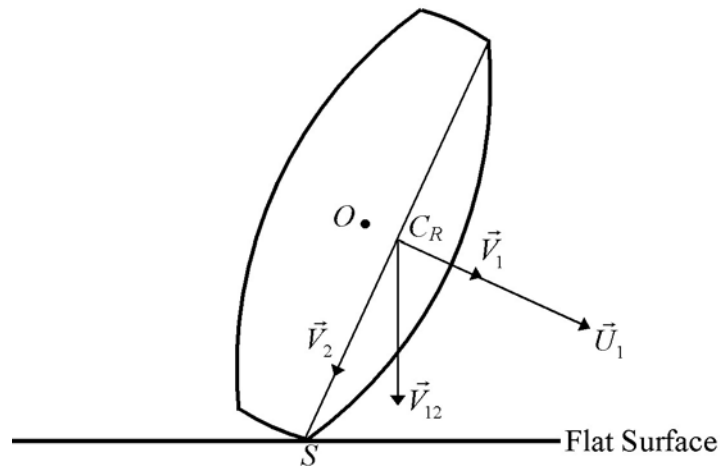
Figure 4.7 Schematic diagram of method determining the point S on the rim of the tablet

Therefore, the location of point S is:

$$S = C_R + (R_1 \cos \alpha) \frac{\vec{V_2}}{\left| \vec{V_2} \right|} \tag{4.10}$$

It is assumed that the equation of the flat surface is $Ax + By + Cz + D = 0$ and the tablet is located above the flat surface. Therefore, after determining the location of point $S(x_0, y_0, z_0)$, the criteria for this contact form are:

- $\beta < \gamma < 90 - \alpha$
- $Ax_0 + By_0 + Cz_0 + D \leq 0$

4.2.2 Tablet-Curved Surface contact

Since the shape of the rotating drum is cylindrical, a cylindrical shape is used to represent the curved surface in this study. And there are three different contact forms, namely, Surface 1-Curved Surface, Surface 2-Curved Surface and Rim-Curved Surface contacts.

4.2.2.1 Surface 1-Curved Surface contact

Figure 4.8 shows this kind of contact form. In Figure 4.8, R is the radius of the cylinder, L represents the line which goes through the axis of the cylinder, d is the distance from the center of the tablet to the line L, and γ is the angle between two lines, OP and OM. The criteria for Surface 1-Curved Surface contact are:

- $90 - \alpha \leq \gamma \leq 90$
- $d \geq R - R_1$
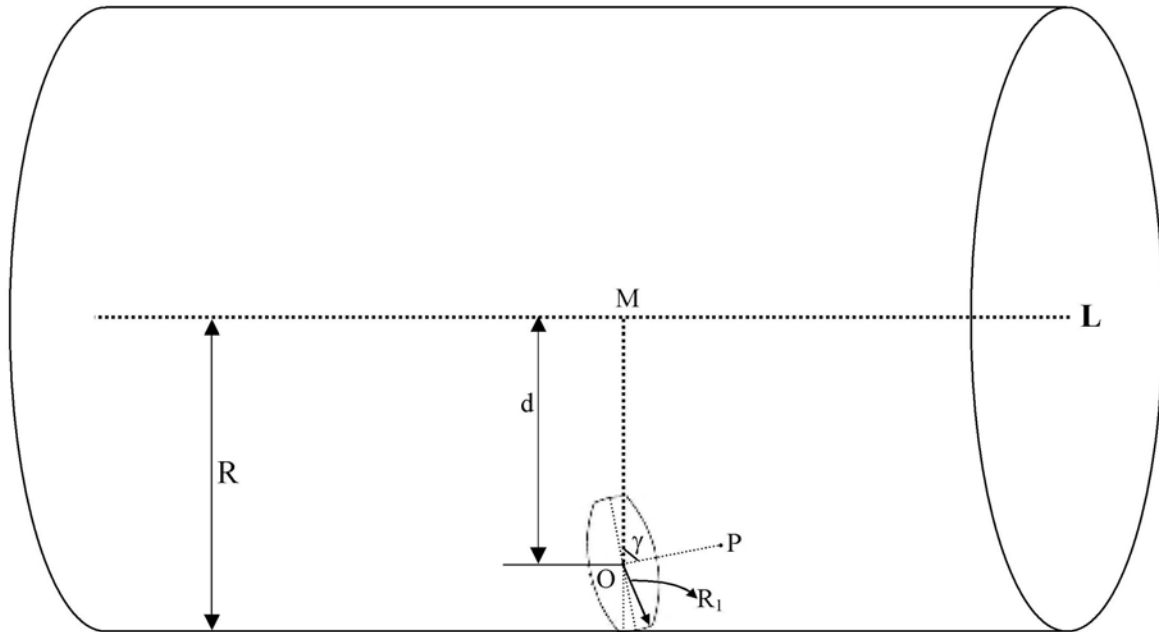
Figure 4.8 Schematic diagram of Surface 1-Curved Surface contact

4.2.2.2 Surface 2-Curved Surface contact

This contact form is shown in Figure 4.9. In this figure, R is the radius of the cylinder. L represents the line which goes through the axis of the cylinder, d is the distance from the center of the larger sphere to the line L, and γ is the angle between two lines, OP and PM. When the contact form is Surface 2-Curved Surface contact, the criteria for this contact are:

- $\gamma \leq \beta$
- $d \geq R - R_2$
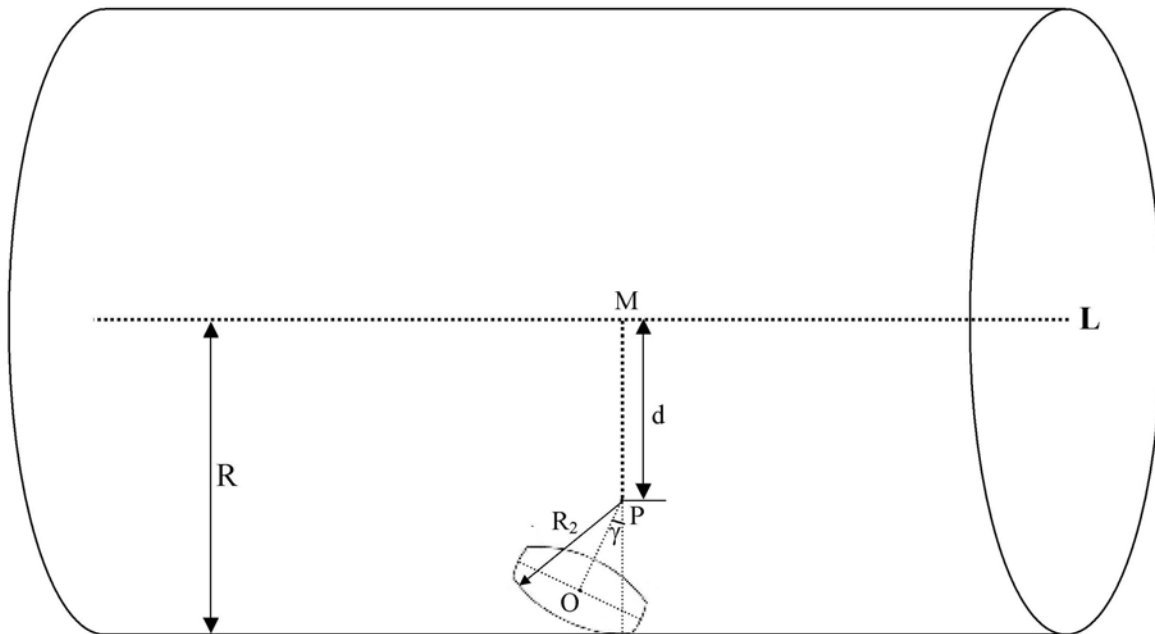
Figure 4.9 Schematic diagram of Surface 2-Curved Surface contact

4.2.2.3 Rim-Curved Surface contact

Figure 4.10 shows Rim-Curved Surface contact. In Figure 4.10, R is the radius of the cylinder, L represents the line which goes through the axis of the cylinder, Point M is the projection of point O on the line L, and γ is the angle between two lines, OP and OM. The first criterion for this kind of contact is that $\beta < \gamma < 90 - \alpha$. When this criterion is satisfied, further information should be used to determine whether the rim of the tablet is in contact with the curved surface or not. For this case, the location of point S on the rim of the tablet from which the distance to point M is maximum will be determined using the same method mentioned in Section 4.2.1.3. Finally, if the distance from S to line L is less than R, which is the radius of the cylinder, Rim-Curved Surface contact exists. Otherwise, the tablet does not contact the curved surface at all.
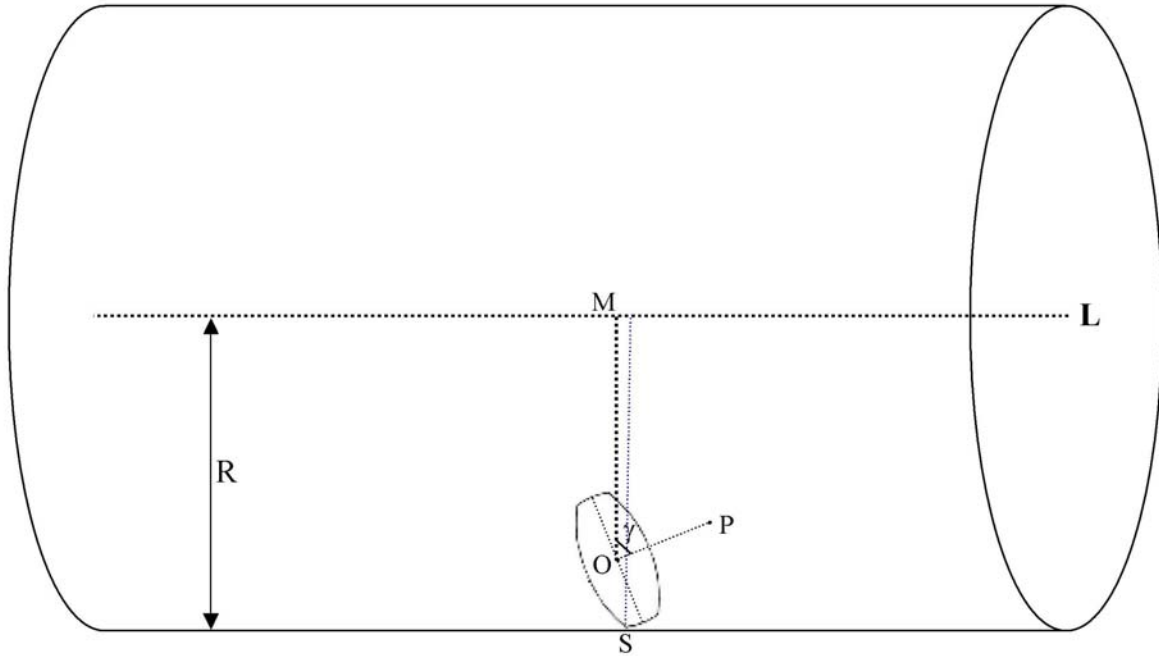
Figure 4.10 Schematic diagram of Rim-Curved Surface contact

4.2.3 Tablet-Tablet contact

From the representation of the shape of the tablet in Figure 4.1, it can be seen that there are three kinds of contact forms in Tablet-Tablet contact, which are Surface 1-Surface 1, Surface 2-Surface 2 and Surface 1-Surface 2, respectively. Considering the rim contact with the tablet, three additional contact forms are possible in Tablet-Tablet contact: Rim-Surface 1, Rim-Surface 2 and Rim-Rim contact [59].

4.2.3.1 Surface 1-Surface 1 contact

Figure 4.11 illustrates the Surface 1-Surface 1 contact form. In Figure 4.11, O_1 and O_2 are the centers of two tablets, P and M are the centers of the larger spheres that determine the tablets' shape, R_1 is the radius of the smaller sphere, α is the angle defined in Figure 4.1, γ_1 is the angle between two lines O_1P and O_1O_2, and γ_2 is the angle between lines O_2M and O_1O_2.
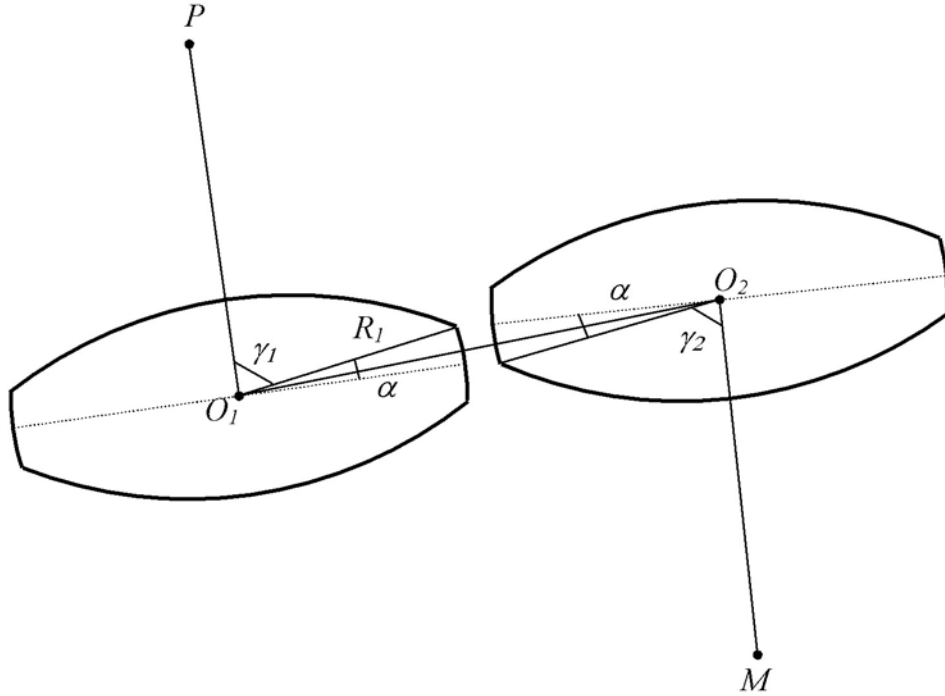
Figure 4.11 Schematic diagram of Surface 1-Surface 1 contact [59]

The criteria for Surface 1-Surface 1 contact are:

- $\gamma_1 \geq 90 - \alpha$
- $\gamma_2 \geq 90 - \alpha$
- $O_1 O_2 \leq 2R_1$

4.2.3.2 Surface 2-Surface 2 contact

Surface 2-Surface 2 contact is shown in Figure 4.12. R_2 and β are defined in Figure 4.1, γ_1 is the angle between the two lines $O_1 P$ and MP, and γ_2 is the angle between the two lines $O_2 M$ and MP. The criteria for Surface 2-Surface 2 contact are:

- $\gamma_1 \leq \beta$
- $\gamma_2 \leq \beta$
- $MP \leq 2R_2$
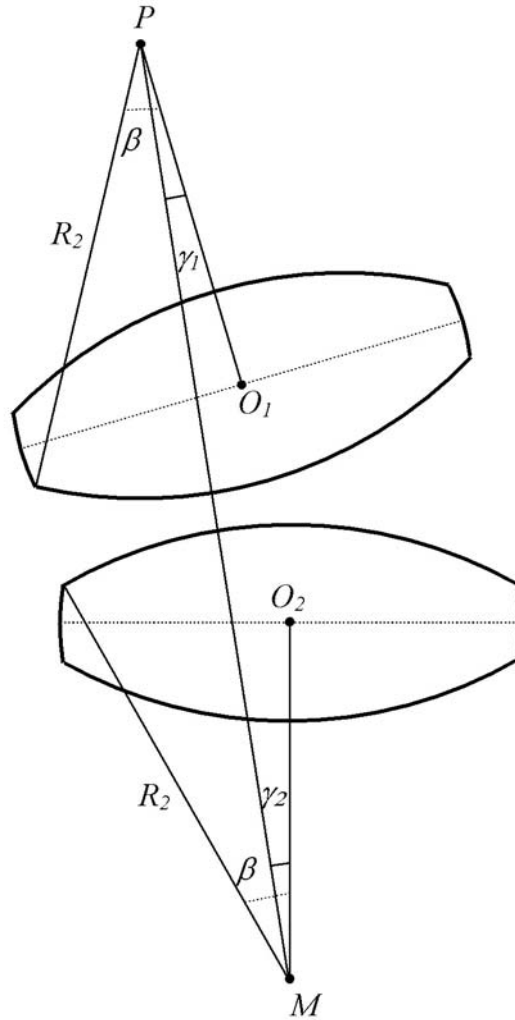
Figure 4.12 Schmetic diagram of Surface 2-Surface 2 contact [59]

4.2.3.3 Surface 1-Surface 2 contact

Figure 4.13 shows the Surface 1-Surface 2 contact form. In Figure 4.13, γ_1 is the angle between the two lines O_1P and MO_1, and γ_2 is the angle between the two lines O_2M and MO_1. The criteria for Surface 1-Surface 2 contact are:

- $\gamma_1 \geq 90 - \alpha$
- $\gamma_2 \leq \beta$
- $O_1M < R_1 + R_2$

56
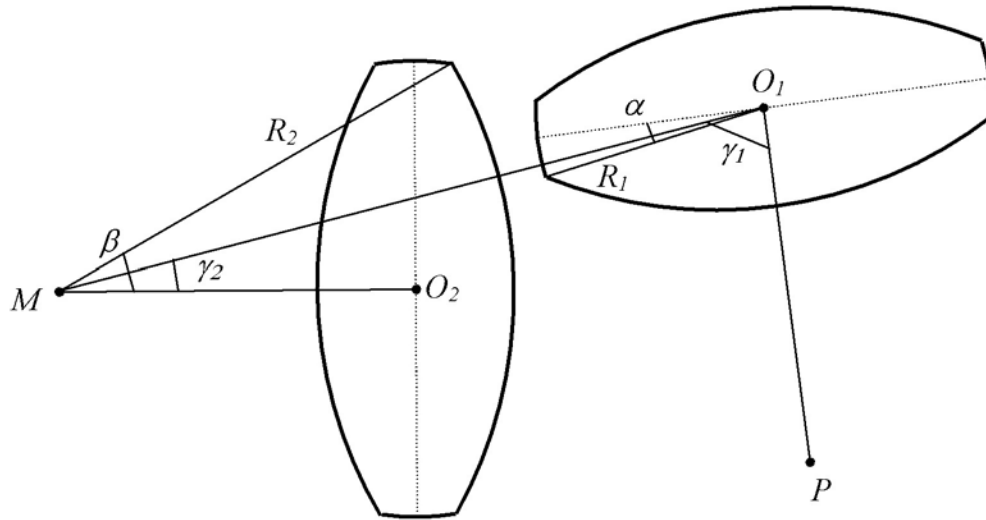
Figure 4.13 Schematic diagram of Surface 1-Surface 2 contact [59]

4.2.3.4 Rim-Surface 2 contact

Figure 4.14 shows the Rim-Surface 2 contact form. For this case, $\vec{V}_{12}$ is the vector from the center of the rim circle to the point P. The location of point S on the rim of the tablet from which the distance to point P is minimum is determined using the same method as in Section 4.2.1.3. Let γ be the angle between two lines, O_1P and PS.
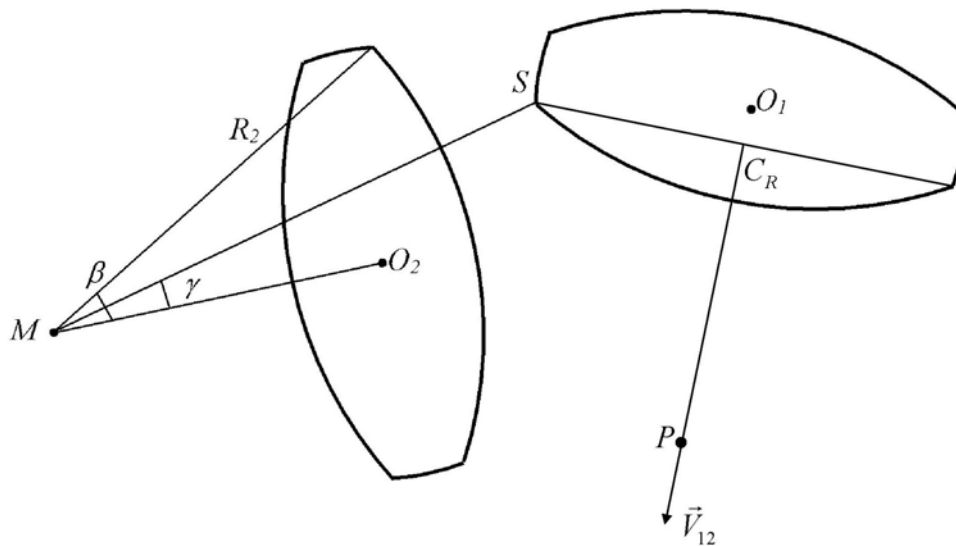
Figure 4.14 Schematic diagram of Rim-Surface 2 contact [59]

57

Therefore, the criteria for this contact are:

- $\gamma < \beta$
- $PS < R_2$

4.2.3.5 Rim-Surface 1 contact

This contact form is shown in Figure 4.15. First, point S on the rim of the tablet is determined by using the method previously mentioned in Section 4.2.1.3. The only difference is that $\vec{V}_{12}$ is the vector from the center of the rim circle to the center of the tablet. Let γ be the angle between two lines, O_1P and O_1S.
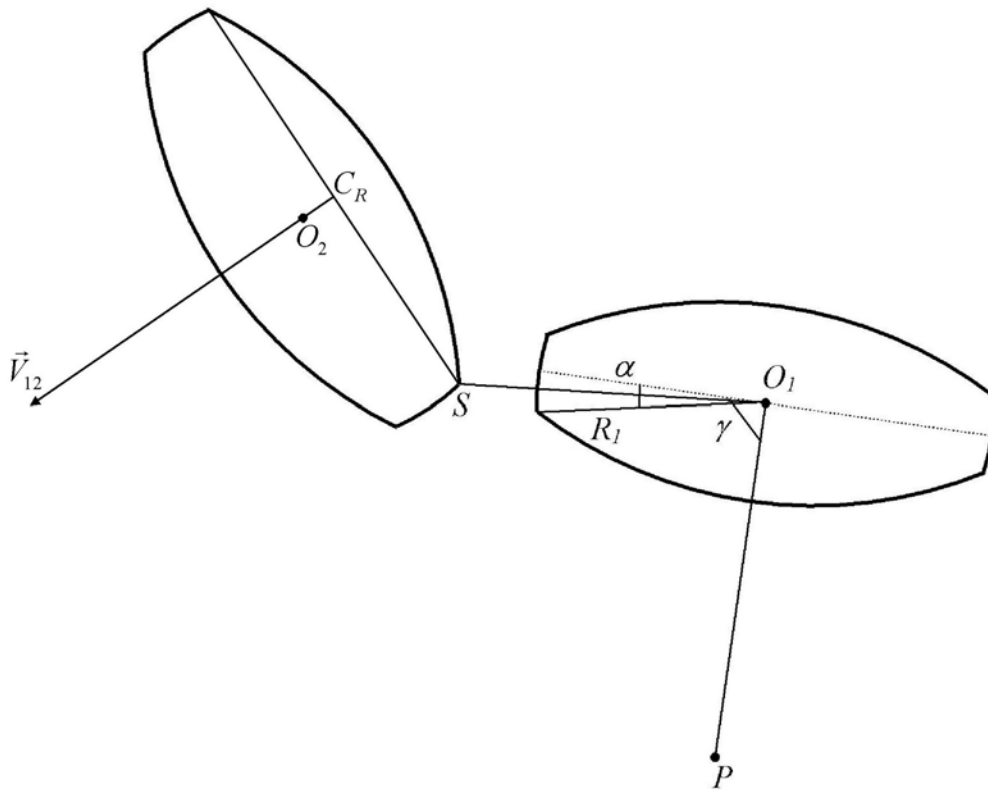
Figure 4.15 Schematic diagram of Rim-Surface 1 contact [59]

Therefore, the criteria for Rim-Surface 1 contact are:

- $\gamma > 90 - \alpha$
- $O_1S < R_1$

4.2.3.6 Rim-Rim contact

Although the Rim-Rim contact is not frequent, it does occur approximately 5% of the time during the multi-particle simulations using tablets. The details of the contact criteria are not addressed in detail here. However, the contact is most conveniently simulated by the contact of two small spheres of radius equal to the radius of curvature of the tablet rim.

4.3 Determination of the parameters used in the contact force models

As mentioned before, Newton's equations of motion will be used to obtain the trajectory of the particles in the DEM simulations. In order to apply Newton's equations to track particle motion, appropriate contact force models should be used to predict the normal and tangential forces between interacting particles in the simulations.

For the normal force model, it is assumed that there is a linear relationship between normal force and normal displacement in the DEM simulations as follows:

$$\begin{cases} Fn = k_1\alpha & \text{For loading} \\ Fn = k_2\alpha + C & \text{For unloading} \end{cases} \tag{4.11}$$

Two parameters should be determined in this normal force model. They are plastic stiffness for loading (k_1) and for unloading (k_2). In general, the plastic stiffness for loading and for unloading can be estimated if the physical properties of the particles are known. However, since tablets used in the pharmaceutical industry are composed of several ingredients and are produced at different operating conditions, it is very difficult to obtain physical properties for tablets, *a priori*. Instead, other methods such as micro indentation studies and a high speed imaging system can be used to estimate these parameters.

Based on the experimental data for tablets obtained through micro indentation studies (performed by Micro Photonics Inc., CA) [58], the value of the plastic stiffness for loading is

set at 2.918×10^4 (N/m). The relative energy loss for a single tablet contact was assessed by using the high speed imaging system to record the movement of a tablet hitting a flat surface. It was found that the relative energy loss was about 50%. Therefore, the value of coefficient of restitution $\left(COR = \sqrt{k_1 / k_2} \right)$ was set at 0.707. Figure 4.16 shows the relationship of normal force with normal displacement used in the DEM simulations.
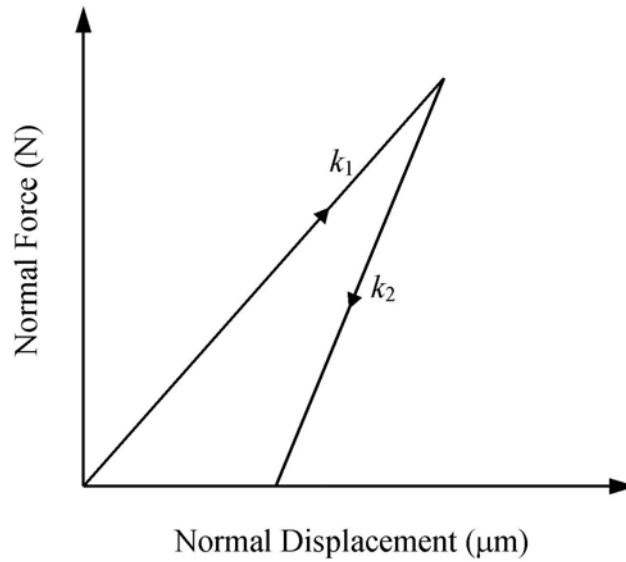
Figure 4.16 The relationship between normal force and normal displacement in the DEM simulations

The tangential forces between the interacting tablets were estimated by using an incremental slipping friction model in the DEM simulations [21]. The tangential displacement was predicted by a two-dimensional surface model discussed in Section 2.2.2 [24]. As shown in Eq. 2.34, K_0 was estimated using following equation in the tangential force model:

$$K_0 = 1.5 k_1 \delta_y^{0.5} (1-v)/(1-v/2) \tag{4.12}$$

where, k_1 is the stiffness for loading, δ_y is the plastic limit and is set equal to 10 μm, and v is the Poisson ratio of the tablet, which is equals 0.33. The value of coefficient of friction was 0.4. The time step used in the DEM simulation was 1.0×10^{-6} s.

4.4 Comparison of DEM simulations with experiments for tablet-tablet contact

Figure 4.2 shows the dimensions of a typical standard round tablet used in this research. For a 420 mg standard tablet, the dimensions are $L_1 = 3.3$ mm, $L_2 = 5.1$ mm and $L_3 = 10.5$ mm. By using MATLAB^{TM} code, I developed the DEM simulation program for tablet-tablet contact. Tablet orientation was represented by using Quaternion method in this simulation. The criteria given above for tablet-tablet contact were implemented in MATLAB^{TM} code to simulate a single tablet hitting another stationary tablet. The conditions of the simulation are shown in Table 4.1.

Table 4.1 Conditions of the DEM simulation for tablet-tablet contact

Diameter of the tablet (mm)	10.5
Center thickness of the tablet (mm)	5.1
Edge thickness of the tablet (mm)	3.3
Tablet density (g/cm^3)	1.1
Poisson ratio of the tablet	0.33
Coefficient of restitution	0.707
Plastic stiffness for loading (N/m)	2.918×10^4
Coefficient of friction	0.4
Plastic limit (μm)	10
Time interval (second)	1×10^{-6}

In order to verify the simulation, the high speed imaging system was used to capture the images of one tablet hitting another one fixed to a flat surface. Since angular velocity is the most sensitive parameter measured by the high speed imaging system, only the magnitude of the angular velocities were compared between simulations and experiments. Table 4.2 shows

the results from both simulations and experiments. From Table 4.2, it can be seen that there was good agreement between simulation and experimental results.

Table 4.2 Comparison of simulation and experimental results for angular velocities for two contacting tablets [59]

	Angular velocity (rad/s)		% error
	from experiment	from simulation	
Case 1	170	166	2%
Case 2	89	90	-2%
Case 3	209	187	11%
Case 4	251	236	6%

As mentioned in Section 2.5, other methods have been used to represent the shape of non-spherical particles. Practically, multi-sphere representations have been widely used for non-spherical particle DEM simulations due to the simplicity of handling spherical particles. Simulation results for non-spherical particles using multi-sphere representations showed that good agreement was obtained from both experiments and simulations in determining packing density of non-spherical particles [48]. However, to date, there has been no comparison of the dynamic behavior of particles using multi-sphere representations.

Therefore, in order to verify the efficiency of the current representation of tablet shape through the intersection of three spheres, representations of the tablet shape using multiple identical spheres were also used to simulate a tablet hitting another stationary tablet. The difference between these two representation methods is that the contact criteria developed in Section 4.2 will be used for the tablet form, while the contact detection algorithm in multi-sphere representations is based on the center locations of each sphere used to determine the shape of the tablet. For the multi-sphere representations, the number, the diameter of the spheres, and the locations of these spheres were determined to give the best representation of

the geometry of the tablet. The algorithm for the multi-sphere representations involves identifying the pair of contacting spheres and then applying the contact force models for the two contacting spheres.

For the tablet-tablet contact simulations using multi-sphere representations, four different representations of the tablet containing 10, 26, 66 and 178 identical spheres were used. Figure 4.17 shows these four multi-sphere representations. The computational times for tablet-tablet contact using different representation methods were compared. The computational time is defined as the time required for the moving tablet to contact and fully rebound from the stationary tablet. The initial conditions are the same for all tablet shape representations in the simulations. The initial velocity of the moving tablet is [0 0 -1.18] m/s, the relative horizontal distance between the two tablets is $3R_1/4$ and both tablets have initial horizontal orientation. Here R_1 is the radius of the smaller sphere in Figure 4.1.
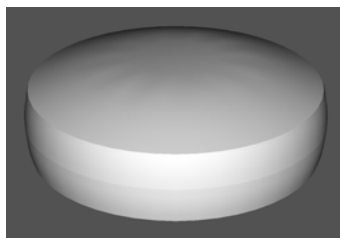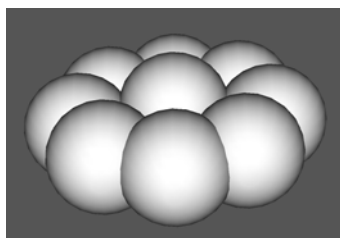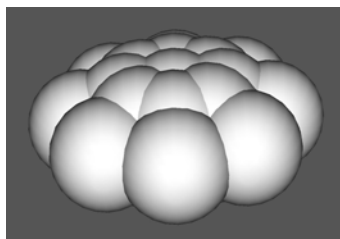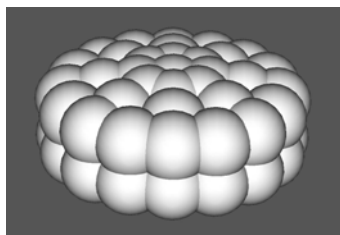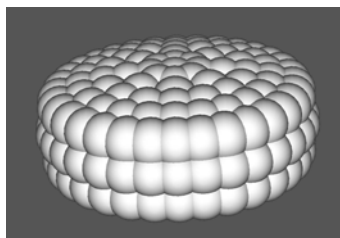
Figure 4.17 The tablet shape and the multi-sphere representation of tablet shape (A) Tablet shape, (B) 10-sphere representation, (C) 26-sphere representation, (D) 66-sphere representation, (E) 178-sphere representation [59]

The computational times for all different representations are shown in Figure 4.18. In addition, the computational time for a single sphere-sphere contact is also shown in Figure 4.18. For the single sphere, the volume of the sphere is equal to the volume of the tablet defined by Figure 4.2.
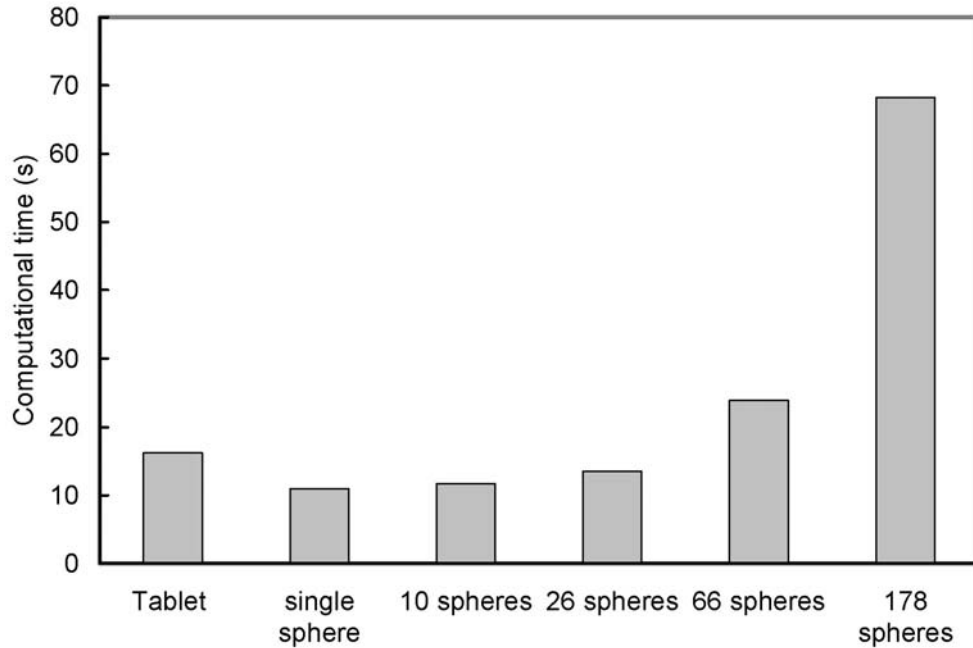
Figure 4.18 The computational times for different shape representation methods [59]

From Figure 4.18, it is seen that the computational time for tablet using 3-sphere model was about 1.5 times longer than for a single sphere contact. In addition, the computational times for 66- and 178-sphere representation were much larger than for the tablet using 3-sphere model. The reason is that although the contact algorithm for spherical particles is straightforward, many single sphere-sphere contact detections must be performed for a single tablet-tablet contact when multi-sphere representations were used. Therefore, the detection time will be dramatically increased when the number of spheres used for the representation of the non-spherical particle shape is increased. Moreover, the contact detection times will increase on the

order of $N^{1\sim2}$ (N is the total number of spheres in the system) for multi-particle simulations using tablets through multi-sphere representations.

Bertrand et al. [60] noted that no study has been made to investigate the effect of the number of spheres on the overall accuracy of non-spherical particle DEM simulations using multi-sphere representations. So the angular velocities of the moving tablet were also studied and compared for tablet-tablet contact using all tablet shape representations. Two different initial conditions were used in the simulations. One tablet was horizontally anchored to a flat surface. The initial height of the other tablet was set at 10 cm above the fixed tablet. Two different cases were investigated in the simulations: the two tablets have the same orientation in the first case, and the initial angle of the moving tablet was set at 11.25° from the horizontal and the rotation axis is [1 0 0] in the second case. These two different sets of initial conditions are shown in Figure 4.19, where X is the distance between two lines that go through the tablet centers, β is the relative orientation angle between two tablets ($\beta = 11.25^{\circ}$ in the simulation).
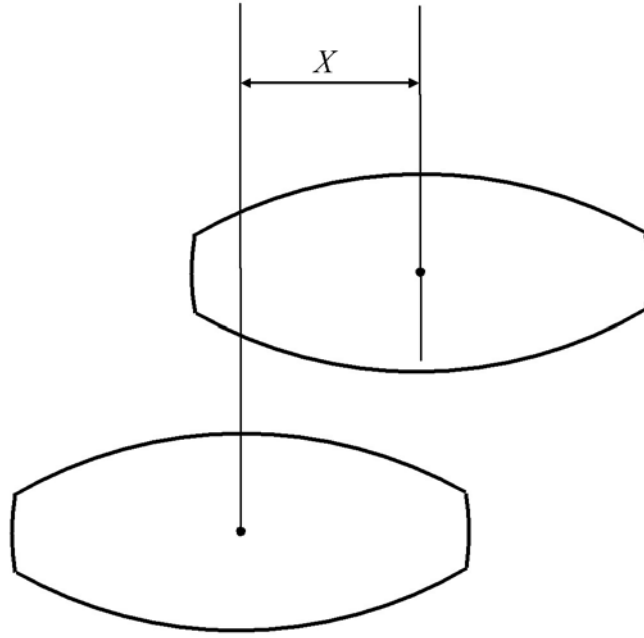
(A)
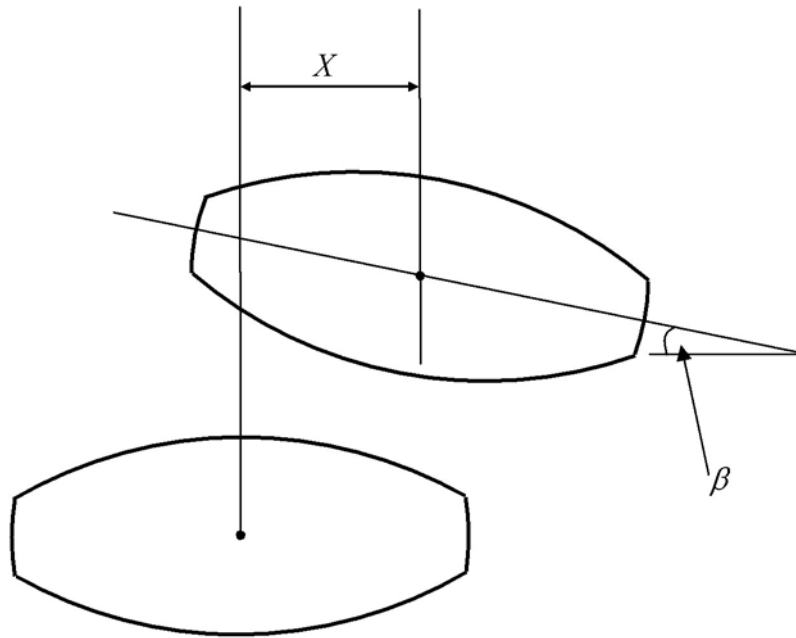
(B)

Figure 4.19 The initial relative conditions of the two tablets used in the DEM simulations. (A) Two tablets have the same orientation, (B) the rotation angle is 11.25° between two tablets [59]

Table 4.3 shows the angular velocities for all cases. From Table 4.3, it is seen that the angular velocities for the 178-sphere representation were still much larger than those for the tablet representation for all cases. Compared with the tablet shape representation, the direction of normal forces and the magnitude of the torques acting on the moving tablet were significantly different from the results for multi-sphere representations. The reason why the dynamic behavior of tablets hitting each other is different for all cases is that there is different macro-roughness for the surfaces of particles comprised of different number of spheres.

Table 4.3 Comparison of simulation results between tablet shape using 3-sphere model and different tablet representations using 10, 26, 66 and 178 identical spheres [59]

X	Angular Velocity (rad/s)				
	Tablet using 3-sphere model	10 spheres	26 spheres	66 spheres	178 spheres
(A)					
0	0	0(1)	0(1)	0(1)	0(1)
$R_1/4$	-1.1	-36.5(1)	-35.3(11)	-52.3(13)	-47.0(20)
$R_1/2$	-17.6	-49.9(2)	-71.2(9)	-78.2(11)	-81.6(16)
$3R_1/4$	-43.3	-69.1(2)	-101.7(7)	-102.7(11)	-114.5(16)
R_1	-72.1	--90.7(1)	-117.0(3)	-117.5(5)	-130.7(18)

Positive values represent the anti-clockwise direction, and negative values are the clockwise direction about the rotation axis. The values in the parenthesis represent the number of sphere-sphere contact calculations per tablet contact.

X					
(B)					
0	7.3	-4.47(1)	54.2(11)	48.5(13)	43.2(16)
$R_1/4$	-5.5	-44.5(1)	15.5(11)	7.7(13)	1.14(16)
$R_1/2$	-3.7	-19.6(2)	-50.7(9)	-35.3(13)	-25.2(16)
$3R_1/4$	-10.3	-28.4 (1)	-90. 6(9)	-61.5(9)	-73.8(18)
R_1	-30.4	-53.8(1)	-103.4(5)	-105.9(9)	-101.2(16)

Positive values represent the anti-clockwise direction, and negative values are the clockwise direction about the rotation axis. The values in the parenthesis represent the number of sphere-sphere contact calculations per tablet contact.

      (A) corresponds to a starting position given in Figure 4.19(A)
      (B) corresponds to a starting position given in Figure 4.19(B)

Table 4.3 also shows the number of sphere-sphere contacts for a single tablet-tablet contact using the multi-sphere representations. It is found that as many as 20 different sphere-sphere contacts occurred for the multi-sphere representations compared to the single tablet-tablet contact using the intersection of three spheres as the tablet shape. Overall, the accuracy of the prediction of single tablet-tablet interactions using multi-sphere representations is poor and computational times were much larger than for the tablet shape representation using 3-sphere model. Therefore, the representation of tablet shape using the intersection of three spheres is more efficient and accurate for investigating the dynamic behavior of the standard round tablets using DEM methods.

4.5 Effect of liquid bridges on the dynamic behavior of the collision of two tablets

For the simulation of tablet-tablet contact including the presence of a liquid bridge between two particles, it is assumed that the contact angle for the liquid-tablet interface is zero and that the thickness of the liquid film on the surface of the tablet is about 100 μm. Therefore, the ratio of the volume of liquid bridge to the volume of the tablet is about 1.1×10^{-4} in the simulation. Table 4.4 shows the simulation results for the effect of the presence of a liquid. In the simulation, the two tablets had the same initial orientation. The initial height of the moving tablet was set at 12 cm above the fixed one. The velocity of the moving tablet was calculated after it rebounded from the stationary tablet.

Table 4.4 Simulation results showing the effect of surface tension and liquid viscosity

Surface Tension of Liquid (J/m²)	Viscosity of Liquid (cps)	Rebounded Velocity (m/s)		
		Limiting separation distance: 1000 μm	Limiting separation distance: 100 μm	Limiting Separation distance: 10 μm
N/A	N/A	1.31	1.31	1.31
0.00725	N/A	1.295	1.295	1.295
0.0215	N/A	1.294	1.294	1.294
0.00725	1	1.289	1.266	1.114
0.00725	10	1.232	1.008	0
0.00725	100	0.669	0	0
0.00725	200	0.054	0	0

From Table 4.4, it can be seen that the effect of capillary forces was negligible compared to the effect of viscous forces, especially for high viscosity liquids. The effect of the magnitude of the limiting separation distance, used to predict the viscous forces, is also shown in Table 4.4. For a limiting separation distance of 100 μm, the simulation predicts that the two tablets stick together when the viscosity was 100 cps or greater. However, in experiments shown in Figure 3.3, using a high speed imaging system to record single tablet-tablet contacts with impact velocities of about 1.5 m/s, the results showed that the moving tablet still rebounded back, even though a silicone oil with a viscosity of 134 cps was used. This comparison of simulation results with experiments indicated that the limiting separation distance should be larger than 100 μm when the proposed viscous force model is applied in the DEM simulations. The proposed value of the S_C is much different from that used by Nase et al. [57], who suggested that a value of about 10^{-6} m, due to the presence of asperities. Simons [60] mentioned that the liquid bridge volume should be sufficient (the ratio of the liquid bridge volume to the volume of the particle is about 0.05) in order to apply this liquid viscous force model. In the current work, this ratio is about 1.1×10^{-4}, which may be the reason why the limiting separation distance is different in our simulations.

In addition, for a limiting separation distance of 1 mm, when the viscosity of the liquid is increased from 1 cps to 100 cps, the velocity is decreased from 1.289 m/s to 0.669 m/s, which means that the relative energy loss for single tablet-tablet contact, due to the presence of the liquid bridge, is about 73%. For typical aqueous film coating solutions used in the pharmaceutical industry, the viscosity of the solution ranges from 50 to 200 cps when the solid concentration is in the range of 8-10% [62]. In addition, liquid bridge may be formed between particles by under-drying in the coating process. The viscosity of liquid bridge between particles will be increased dramatically since the solid concentration is increased, which results in twinning problem for the coating process. Therefore, the effect of liquid bridges is important and should be taken into account for the simulation of tablet coating in a rotating drum.

In order to apply the proposed viscous force model in multi-particle DEM simulations, it is essential to obtain the value of a limiting separation distance, *a priori*. The movement of tablet-tablet contact with five different viscous silicone oils was recorded using the high speed imaging system. The viscosities of the silicone oils used were 100, 200, 350, 500 and 1000 cps. Figures 4.20-4.24 show the images of tablet-tablet contact using oils of different viscosity.

t = 0			t = 0
t = 0.021 s			t = 0.026 s
t = 0.042 s			t = 0.052 s
t = 0.063 s			t = 0.078 s
t = 0.084 s			t = 0.104 s
t = 0.105 s			t = 0.130 s
t = 0.126 s			t = 0.156 s

(A)   (B)
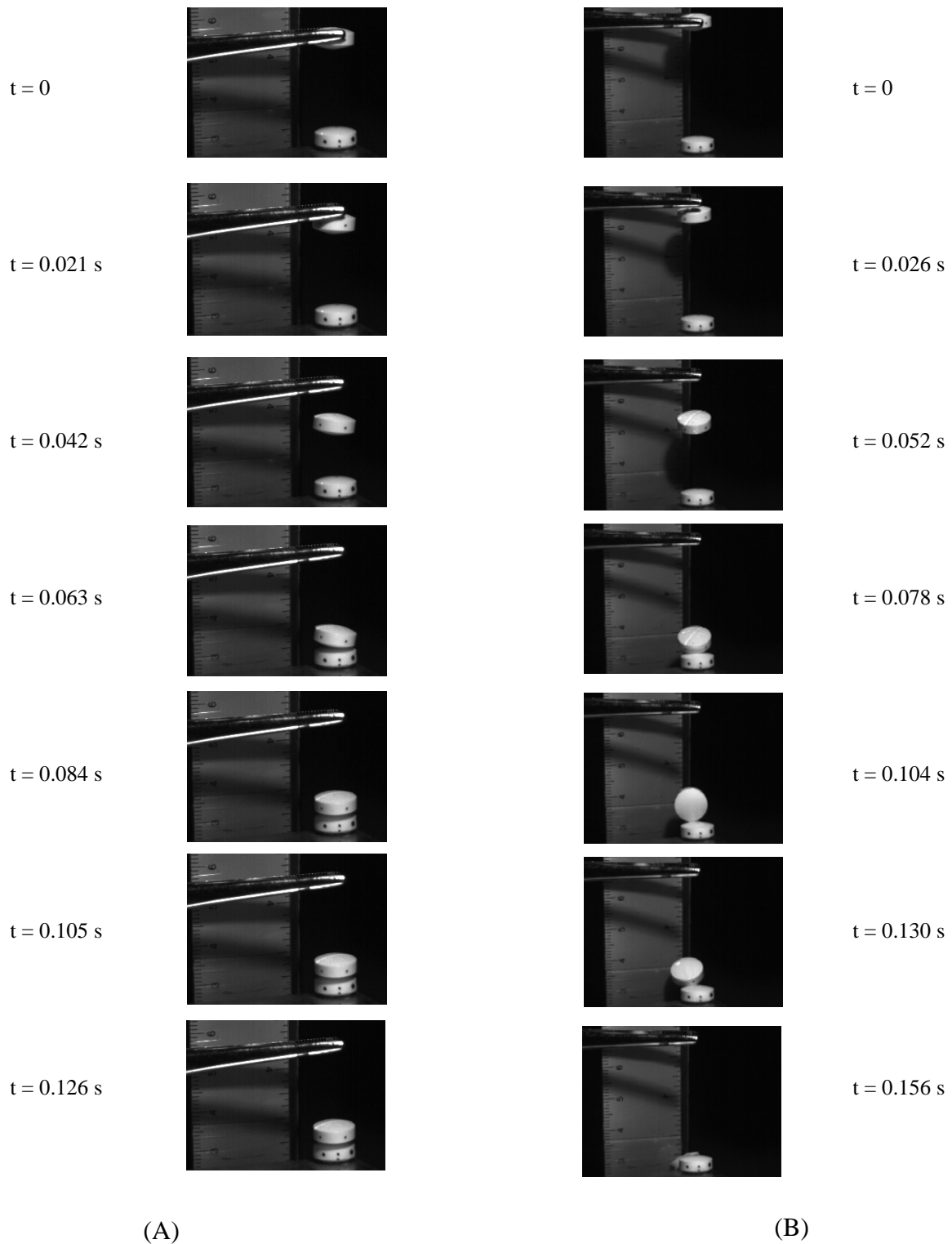
Figure 4.20 Comparison of a series of successive images of tablet-tablet contact using viscous silicone oil with viscosity of 100 cps (A) sticking together; (B) not sticking together

t = 0   t = 0

t = 0.049 s   t = 0.040 s

t = 0.098 s   t = 0.080 s

t = 0.147 s   t = 0.120 s

t = 0.196 s   t = 0.160 s

t = 0.245 s   t = 0.200 s

t = 0.294 s   t = 0.240 s

(A)   (B)
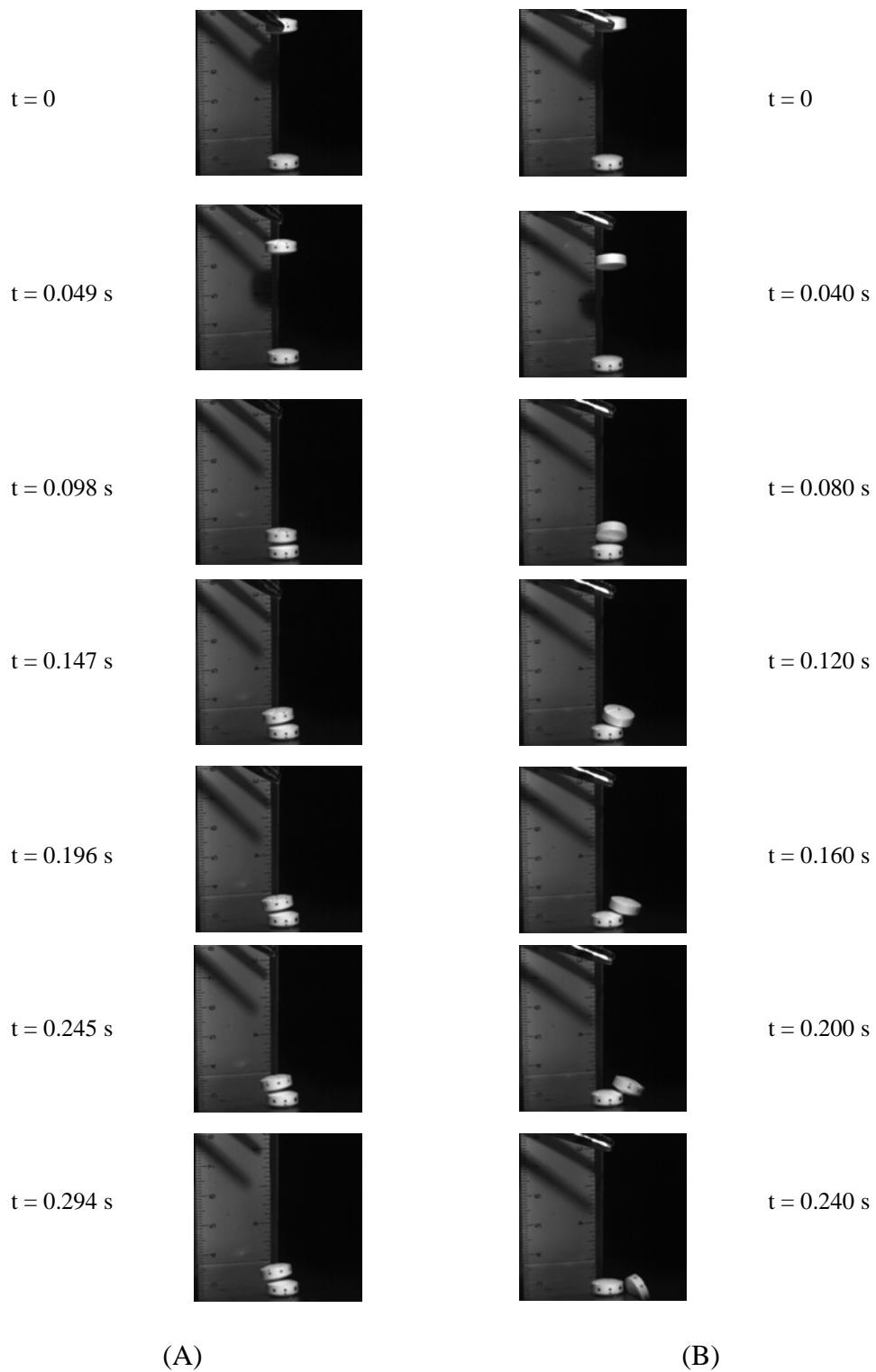
Figure 4.21 Comparison of a series of successive images of tablet-tablet contact using viscous silicone oil with viscosity of 200 cps (A) sticking together; (B) not sticking together

t = 0

t = 0.045 s

t = 0.090 s

t = 0.135 s

t = 0.180 s

t = 0

t = 0.057 s

t = 0.114 s

t = 0.171 s

t = 0.228 s

(A)

(B)
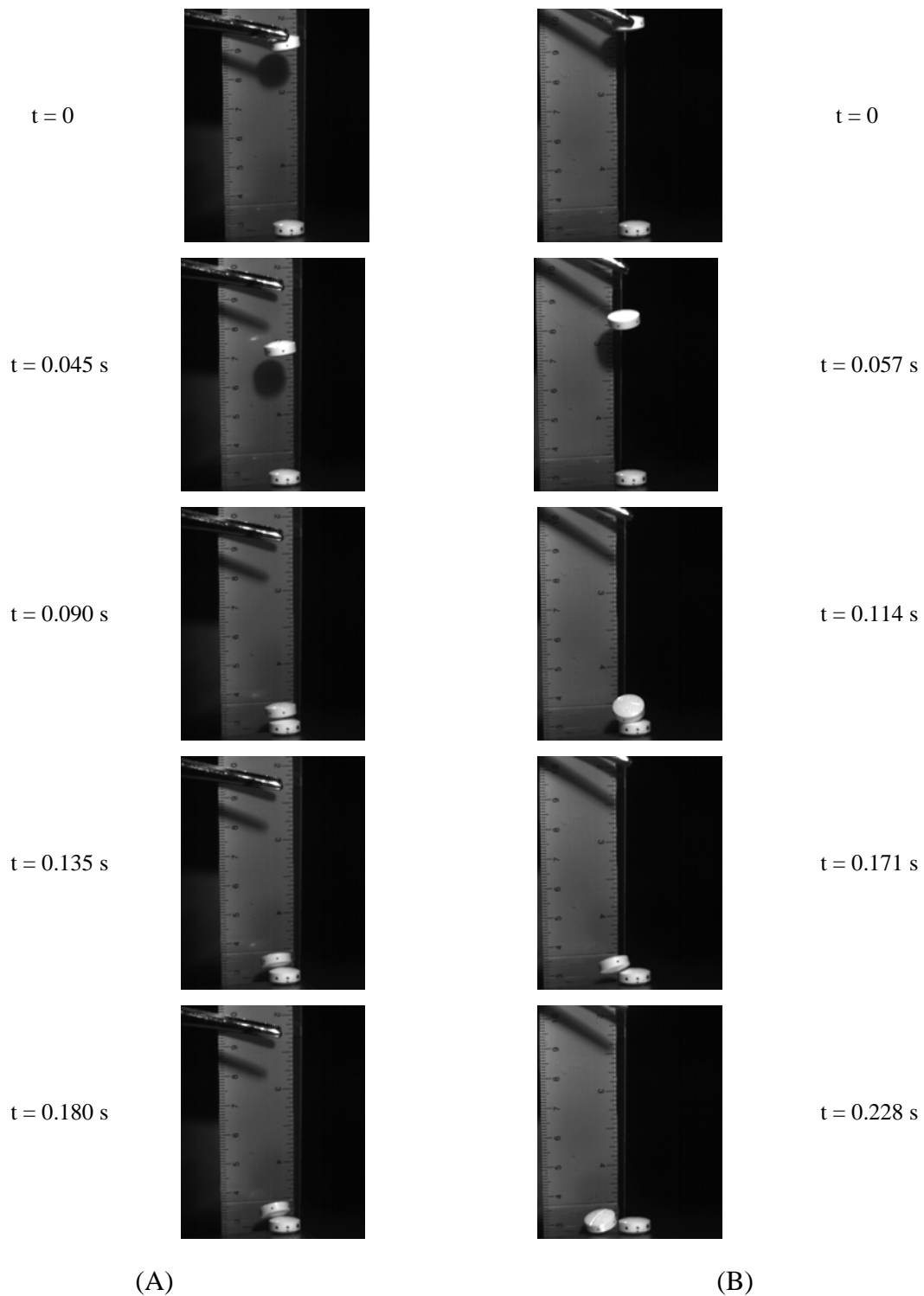
Figure 4.22 Comparison of a series of successive images of tablet-tablet contact using viscous silicone oil with viscosity of 350 cps (A) sticking together; (B) not sticking together

t = 0

t = 0.055 s

t = 0.110 s

t = 0.165 s

t = 0.220 s

(A)

t = 0

t = 0.055 s

t = 0.110 s

t = 0.165 s

t = 0.220 s

(B)
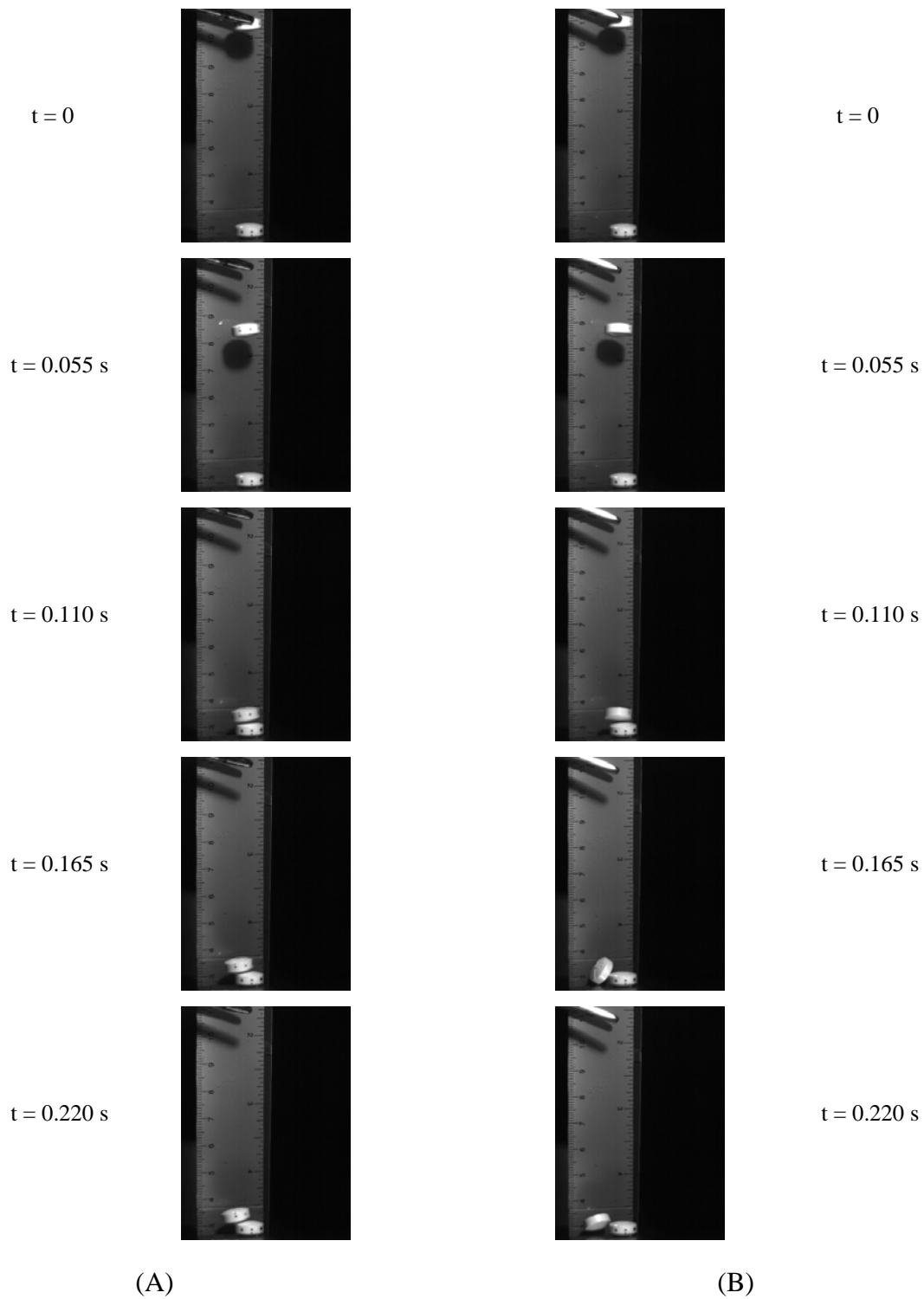
Figure 4.23 Comparison of a series of successive images of tablet-tablet contact using viscous silicone oil with viscosity of 500 cps (A) sticking together; (B) not sticking together

t = 0

t = 0.060 s

t = 0.120 s

t = 0.240 s

t = 0.360 s

t = 0.480 s

t = 0

t = 0.070 s

t = 0.140 s

t = 0.280 s

t = 0.420 s

t = 0.560 s

(A)

(B)
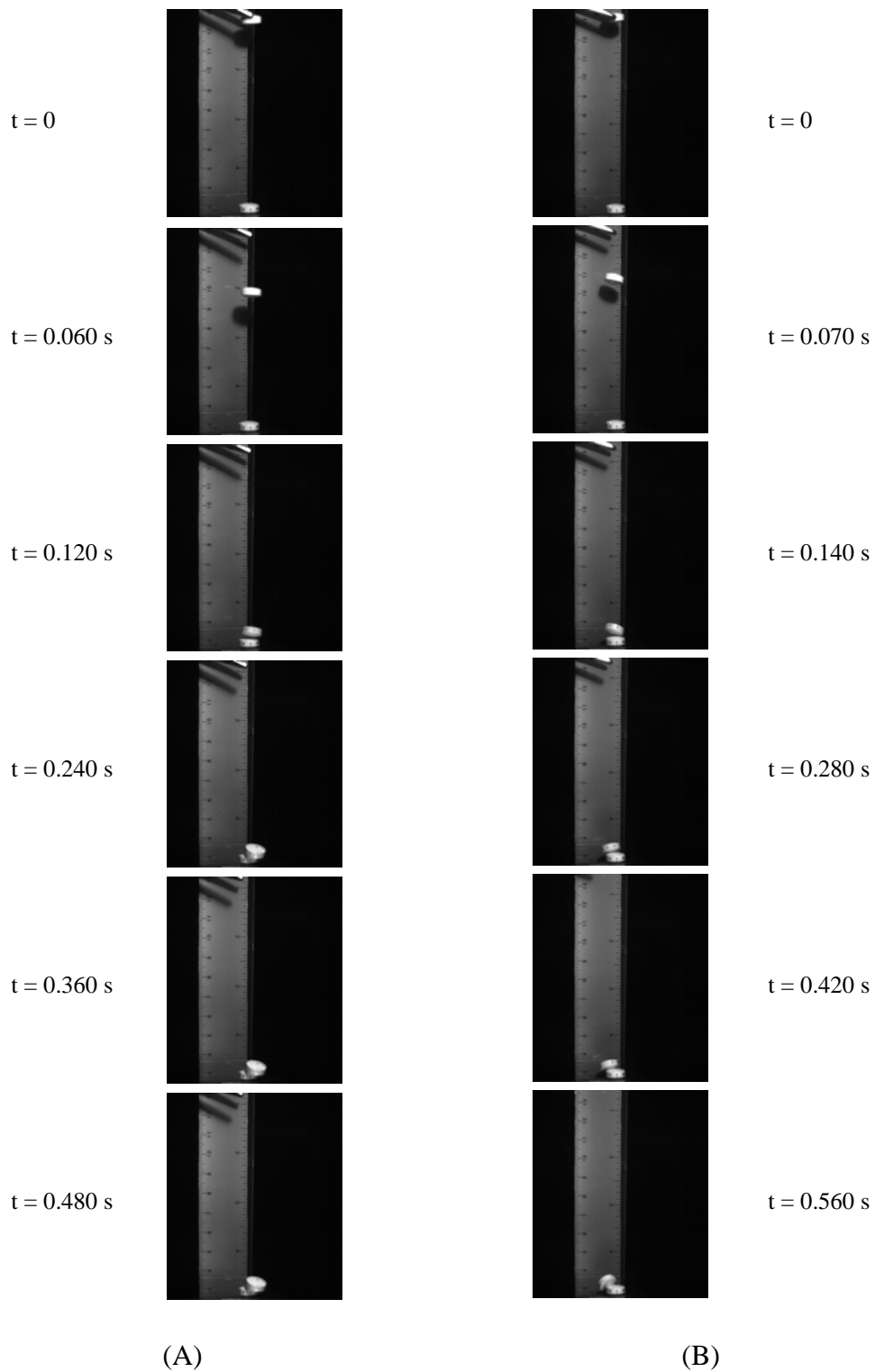
Figure 4.24 Comparison of a series of successive images of tablet-tablet contact using viscous silicone oil with viscosity of 1000 cps (A) sticking together; (B) not sticking together

To determine the limiting separation distance in the liquid viscous force model, the critical initial height of the moving tablets was calculated by the analysis of these images using the spreadsheet analysis module for each viscous silicone oil shown in Figures 4.20 – 4.24, so that there was no rebound after the moving tablet contacted the stationary tablet anchored on a flat surface when different viscosity silicone oils were used. Based on the analysis of the recorded images by the high speed digital imaging system, the critical initial height of the moving tablets for these 5 different viscosity silicone oils were 2.98, 3.97, 5.94, 7.06 and 9.48 cm, respectively. For the tablet-tablet contact simulation which included the liquid viscous force model, the surface tension of the silicone oils was 0.021 N/m and the ratio of the liquid volume to the volume of the tablet was 1.1×10^{-4}. Based on the above critical initial height for each silicone oil, the limiting separation distances were determined through the simulations. It was found that the values of S_C were 0.88, 1.86, 2.63, 3.34 and 6.36 mm, respectively for the silicone oils with the viscosity of 100, 200, 350, 500 and 1000 cps and are shown in Figure 4.25.
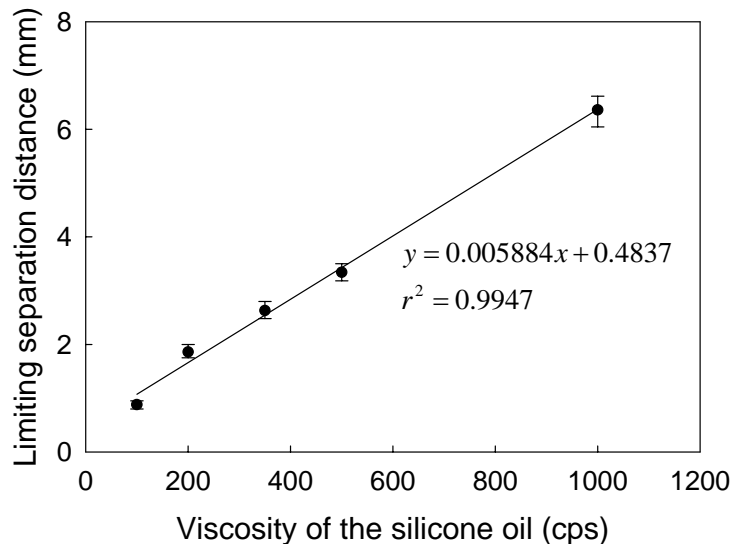
Figure 4.25 The relationship of limiting separation distance with the viscosity of silicone oils

$$y = 0.005884x + 0.4837$$
$$r^2 = 0.9947$$

From Figure 4.25, it can be seen that there is a linear relationship between limiting separation distance and the viscosity of the liquid used to form the liquid bridge between two tablets. The limiting separation distance used in the liquid viscous force model must be increased for a higher viscous liquid. In addition, the order of magnitude of the limiting separation distance was about 1 mm. For the tablet defined in Figure 4.2, the radius of the larger surface of the tablet is about 15.7 mm. Therefore, the dimensionless limiting separation distance in the liquid force model is 0.064 (It is defined as the ratio of limiting separation distance to the radius of the spherical surface). This result is consistent with the work of Mazzone et al. [63], where they found that good agreement was obtained between experiments and simulations when the dimensionless separation distance was taken as 0.05. Therefore, the viscosity of the liquid must be taken into account in order to determine S_C and to apply this liquid viscous force model to multi-particle simulations.

Figure 4.26 shows a series of successive images of tablet-tablet contact with a thin film of silicone oil applied to the larger surface of the fixed tablet. The viscosity of silicone oil is 30,960 cps. From this figure, it is seen that the moving tablet rebounded back after these two tablets contacted each other even though very high viscous silicone oil was used. The reason is that it takes some time to form the liquid bridge between two tablets when the film of the liquid is applied to only one tablet. Based on the simulation result, the total contact time was about 3×10^{-4} s for a single contact between two tablets. Hence, the contact time for a single contact may be not long enough to form the liquid bridge.

t = 0

t = 0.027 s

t = 0.054 s

t = 0.081 s

t = 0.108 s
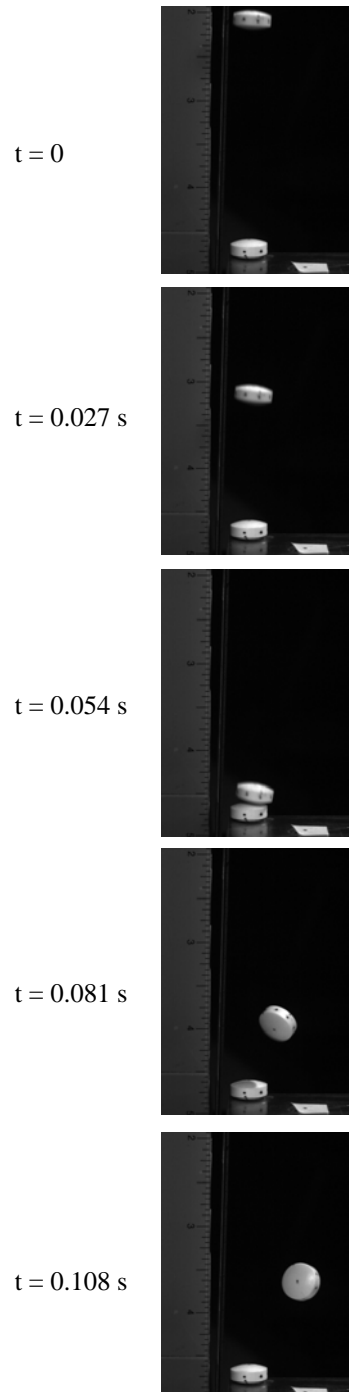
Figure 4.26 A series of successive images of tablet-tablet contact with thin film of silicone oil applied to the larger surface of the fixed tablet (Viscosity of silicone oil is 30,960 cps)

4.6 Multi-particle simulations in a rotating drum

As mentioned in Section 4.4, the computational time for two spheres in contact is much less than that for two tablet-shaped particles in contact in the DEM simulations. The difference in computational times between spherical and tablet-shaped particles is increased dramatically when thousands of particles are simulated in a rotating drum. Therefore, considering the CPU speed of computers used for DEM simulations and understanding better the parameters affecting particle movement in the rotating drums, spherical particles should first be used in the DEM simulations to investigate particle movement in the equipment.

4.6.1 Multi-spherical particles simulations

DEM simulation programs using a MATLAB^{TM}-based code were developed by IETek (Tacoma, WA) to study the movement of a large number of particles in rotating drums. Figure 4.27 shows a snapshot of the graphical user interface (GUI) used in the DEM simulations. From Figure 4.27, it is seen that many parameters used in the simulations can be changed easily. These parameters include operating conditions, the dimension of the drum, particle size and density, and physical properties of particles related to the applied contact force models, etc.
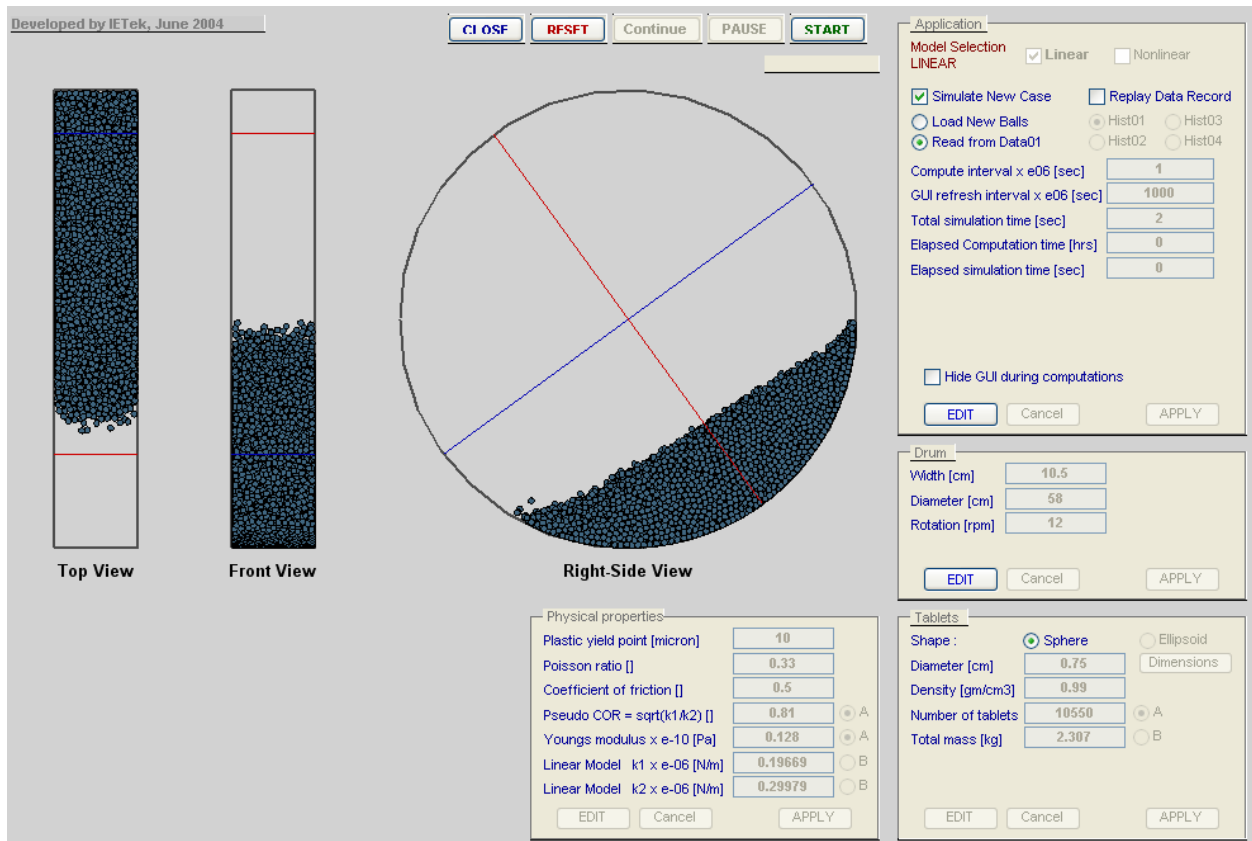
Figure 4.27 A snapshot of graphical user interface in the DEM simulations

In the DEM simulations, the particles used are 7.5 and 9 mm polystyrene spheres with a density of 0.99 g/cm^3. The coefficient of friction for the polystyrene balls is 0.5. Based on the micro indentation studies on the polystyrene balls by Micro Photonics, Inc. (Irvine, CA), the Young's modulus of the particle was set to 1.28×10^9 Pa [64]. The Poisson ratio was 0.33. The relative energy loss for the single contact of polystyrene balls at different initial drop height was analyzed using the high speed imaging system as shown in Figure 4.28. From Figure 4.28, it is found that the relative energy loss for a single contact is about 35% for different initial drop height. Therefore, the value of coefficient of restitution ($COR = \sqrt{k_1 / k_2}$) was estimated to be 0.81, where the ratio of k_1 / k_2 is equal to (1 – relative energy loss for a single contact). The time interval was set to be 1×10^{-6} s. In addition, two different sizes of rotating drum were

used in the simulations. The width of the drum was 10.5 cm, and the drum diameters were 29

and 58 cm, respectively. The pan speed of the drum was varied at two levels of 6 and 12 rpm.

Table 4.5 summarizes the simulation conditions used in the multi-particle simulations using
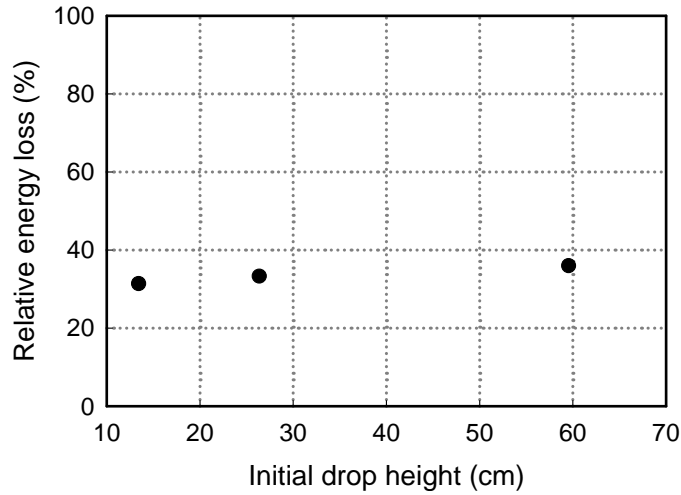
spheres.

Figure 4.28 Relative energy loss on contact for polystyrene balls as a function of drop height using a high speed digital imaging system [3]

Table 4.5 Conditions for multi-particle simulations using spheres

Diameter of spheres (mm)	7.5, 9
Thickness of the drum (cm)	10.5
Radius of the drum (cm)	29, 58
Pan speed of the drum (rpm)	6, 12
Particle density (g/cm^3)	0.99
Poisson ratio of particle	0.33
Coefficient of restitution	0.81
Young's modulus of particle (Pa)	1.28×10^9
Coefficient of friction	0.5
Time interval (second)	1×10^{-6}

In order to represent the effect of pan load on the dynamic behavior of particle movement in

the drums, a parameter called fractional fill volume (υ) was introduced. It is defined as the

ratio of volume occupied by the particle bed to the volume of the rotating drum, and is given by:

$$\upsilon = \frac{\text{Volume of the particle bed}}{\text{Volume of the rotating drum}}$$

To determine the total simulation times required to get to steady-state conditions for all simulations, results for the dynamic angle and for the average surface velocity at a fixed location on the inclined surface of particle bed were compared. Figure 4.29 shows the variation of dynamic angle with different simulation time at a pan speed of 6 rpm for $\upsilon = 0.10$ and $\upsilon = 0.17$ in a 58 cm rotating drum. From Figure 4.29 it is seen that the time required to reach a steady-state condition based on the average dynamic angle is about 6 seconds. The relationship for the average surface velocity at a fixed location with simulation time is also shown in Figure 4.30 at the same conditions. As shown in Figure 4.30, the average surface velocity also reaches a steady-state after 6 to 8 s of simulation. Therefore, results obtained after 8 seconds of simulation are reported in the remaining discussion.
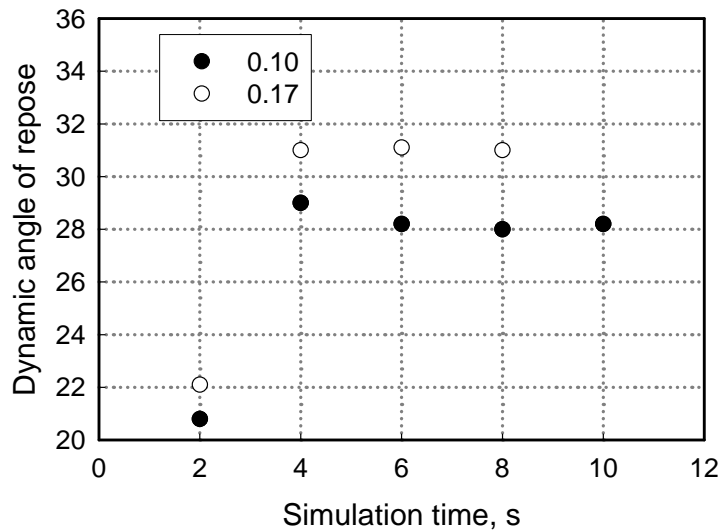
Figure 4.29 Variation of dynamic angle of repose as a function of actual rotation time of pan for $\upsilon = 0.10$ and $\upsilon = 0.17$ in a 58 cm rotating drum [3]
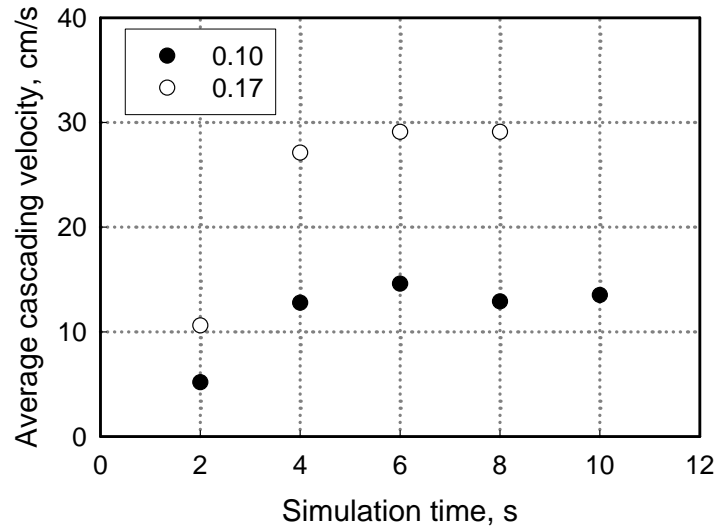
Figure 4.30 Variation of average surface velocity as a function of actual rotation time of pan for $\upsilon = 0.10$ and $\upsilon = 0.17$ in a 58 cm rotating drum [3]

The effect of coefficient of friction for the particles on the variation in dynamic angle of repose was studied in the DEM simulations and is shown in Figure 4.31. This simulation was conducted with 1000 particles in a 24 cm diameter, 8.8 cm wide pan drum with a rotating speed of 6 rpm. As seen in this figure, the angle increases with increasing values of coefficient of friction. The reason is that the increased coefficient of friction between the spheres causes them to move higher in the bed before cascading down, thereby increasing the dynamic angle. This result is not in agreement with that obtained by Yamane et al. [42], where the dynamic angle reaches a constant value at and above some value of coefficient of friction. In addition, the particle-wall slip was found to be substantial for low values of coefficient of friction ($\mu < 0.4$), and gradually decreases with increasing values of μ, hence a monotonic increase in dynamic angle of repose was observed. This is in contrast to the findings of Yamane et al. [42], where there almost was no slip for $\mu > 0.2$. It should be noted that the operating conditions were different for these two studies.
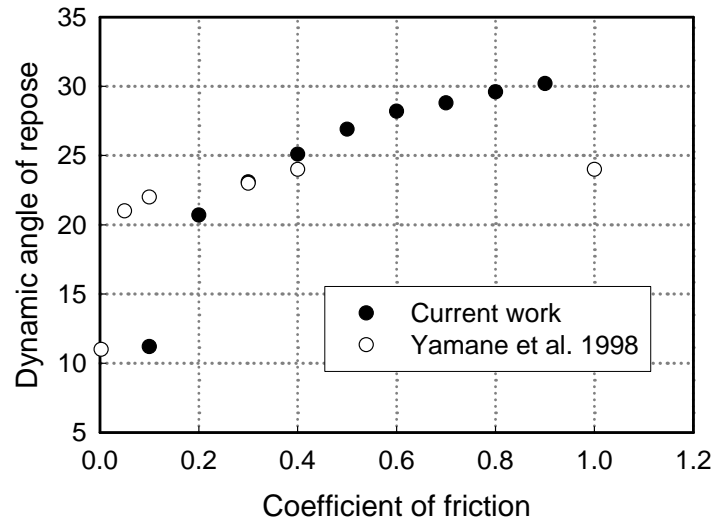
Figure 4.31 Variation of dynamic angle of repose as a function of coefficient of friction in a 29 cm diameter pan with 1000 particles (Results are compared with those obtained by Yamane et al. [42]) [3]

4.6.1.1 Effect of particle size

The effect of particle size on the surface velocity profile of particles on the inclined surface of the particle bed was also simulated. In the simulations, polystyrene balls with diameters of 7.5 mm and 9 mm, respectively, were used in a 58 cm diameter rotating drum. Other parameters in the simulations were set to be the same. Pan speed was set to be 12 rpm. The fractional fill volume was 0.15.

Figure 4.32 shows the surface velocity profiles along the inclined surface of the particle bed for two different particles. In Figure 4.32, the x-axis is the dimensionless distance from the top of particle bed's surface. $x = 0$ refers to the top of the inclined surface and $x = 1$ indicates that the particles are at the bottom of the inclined surface.
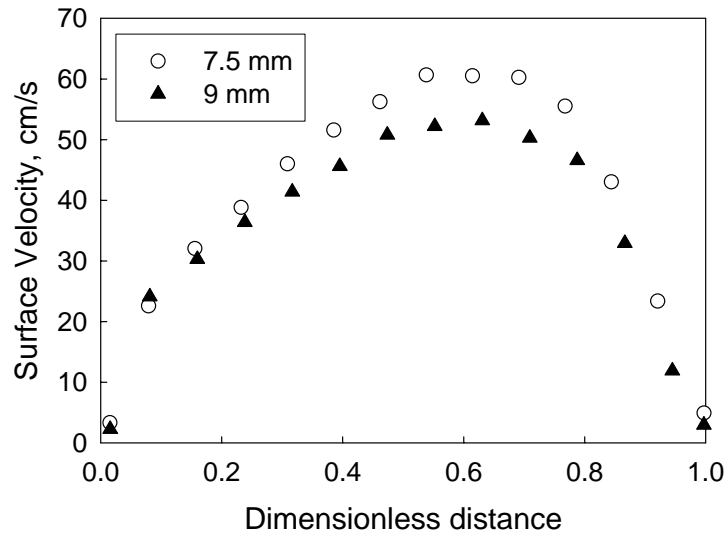
Figure 4.32 Simulated surface velocity profiles along the inclined surface for two different sizes of particles in a 58 cm diameter drum (pan speed is 12 rpm and $\upsilon = 0.15$)

It can be seen that the velocity profiles are somewhat asymmetric and slightly shifted towards the lower end of the chord. The particles reach their maximum velocity close to the mid-point of the chord (dimensionless distance of about 0.6). It is believed that particle-wall and particle-particle interactions at the lower end of the cascading surface propagate upstream, causing a decrease in the velocity of particles after a certain point [65]. The properties of velocity profiles by DEM simulations are close to the experimental results of Alexander and Muzzio [66], who measured the surface velocity profiles along the cascading layer using images from a digital camera installed on the side of a tumbling blender. In their study, all experiments were conducted with the fractional fill volume of 0.5.

In addition, from Figure 4.32, it is found that the surface velocity is increased when using smaller particles in the simulations, which is consistent with experimental results [66]. In order to account for the effect of particle size on surface velocity of particles, the data shown in Figure 4.32 was normalized by using the diameter of particles. It was found that the simulation

86

data overlapped when the surface velocities were multiplied by $d_p^{0.5}$, where d_p is the diameter

of particles. Figure 4.33 shows the normalized surface velocity profiles.
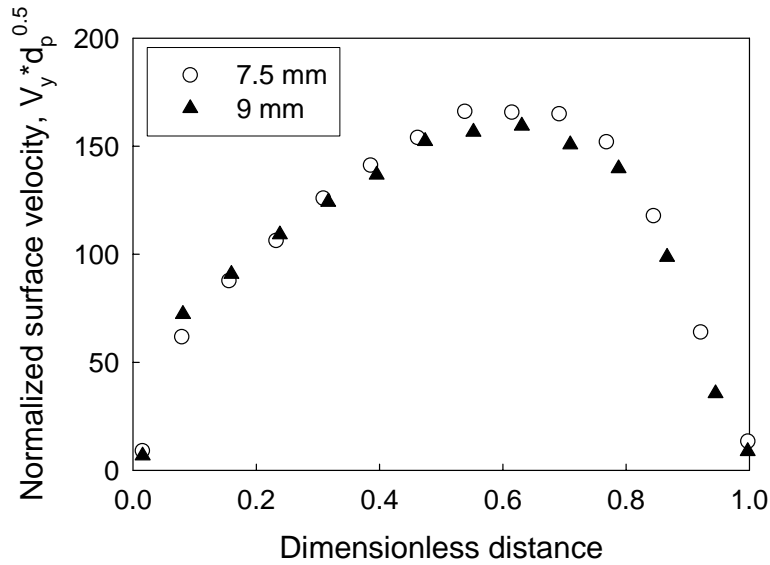
Figure 4.33 Normalized surface velocity profiles from Figure 4.31 by multiplying $d_p^{0.5}$

It was found that surface velocity of particles is inversely proportional to the square root of

particle's diameter as follows:

$$V_y \propto \frac{1}{d_p^{0.5}}$$

4.6.1.2 Effect of fractional fill volume

The effect of fractional fill volume on the surface velocity of particles in a pan coating

device was studied by Pandey et al. [3]. It was shown that the surface velocity of particles will

be increased with increasing fractional fill volume. The velocity of particles in the inclined

surface of the particle bed was proportional to $\upsilon^{1.8}$, where υ is the fractional fill volume [3].

One of the reasons for this is that the dynamic angle of repose is increased when the fractional

fill volume is increased, which results in a higher surface velocity. However, the dynamic angle

only increased from 31.8 to 34.6 degree even though the fractional fill volume was almost doubled to 0.26 in the simulations. Therefore, some other parameters should be considered to account for the effect of fractional fill volume on surface velocity of particles.

Figure 4.34 shows the surface velocity profiles for three different fractional fill volumes in the DEM simulations. The simulations were carried out in a 58 cm diameter drum with 9 mm polystyrene balls and a rotation speed of 12 rpm. From Figure 4.34, it is seen that there is much difference in surface velocities when the fractional fill volume was increased from 0.15 to 0.26.
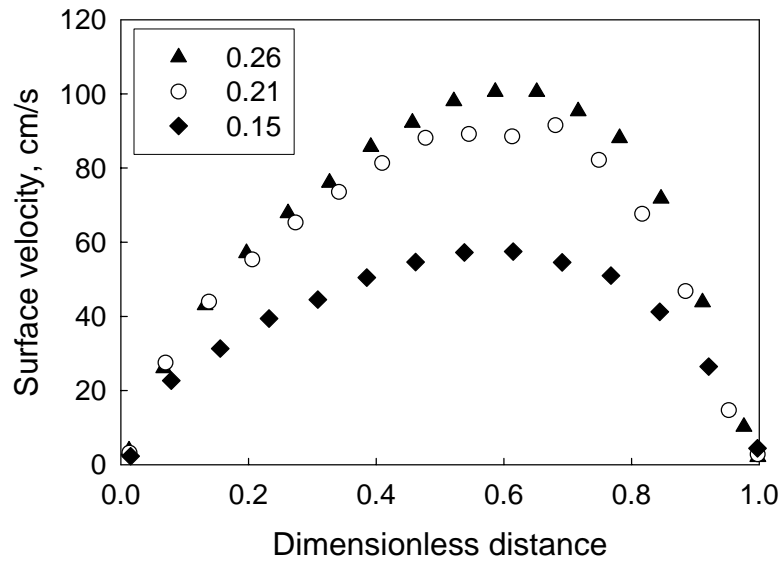
Figure 4.34 Surface velocity profiles in the inclined surface for 9 mm polystyrene spheres at different fractional fill volume in a 58 cm diameter rotating drum (pan speed is 12 rpm)

Figure 4.35 shows the side view of the rotating drum with a rotation speed of Ω in the clockwise direction. υ_1 and υ_2 refer to the two different fractional fill volumes.
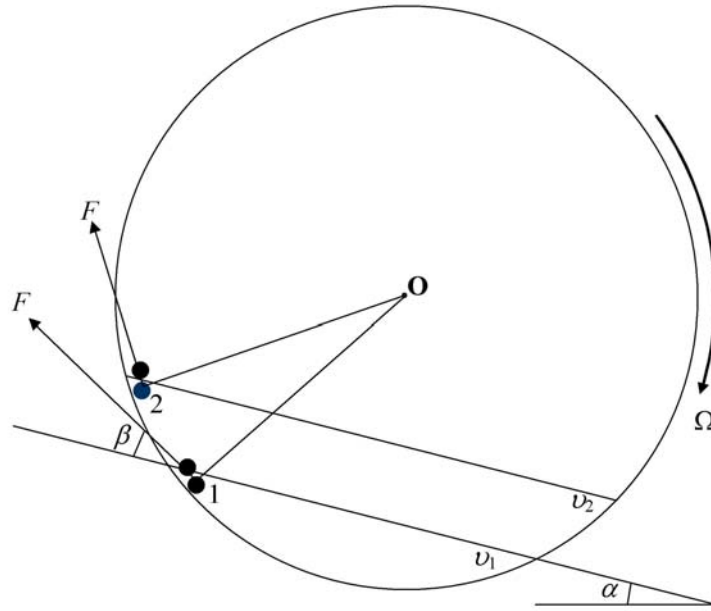
Figure 4.35 Schematic diagram of side view of the rotating drum

As shown in Figure 4.35, the movement of a particle along the inclined surface is resisted by particle 1 below the inclined surface when the fractional fill volume is υ_1. The direction of the interacting force between two particles is also shown for υ_1, which is the same as the direction of the centrifugal force of particle 1. The component of the interacting force along the inclined surface is $F\cos\beta$. When the fractional fill volume is increased to υ_2, the movement of the particle along the inclined surface is resisted by particle 2. Since the rotation speed is kept constant for these two cases, it can be assumed that the interacting force between two particles is constant. However, β, the angle between the direction of interacting force and the inclined surface, is increased for the larger fractional fill volume. So the component of interacting force along the inclined surface decreases with increasing fractional fill volume. Therefore, the movement of particles on the top of the inclined surface will receive less resistance for higher fractional fill volume, which results in higher surface velocity of particles.

Therefore, when the effect of fractional fill volume on the surface velocity of particles is studied, both dynamic angle of repose and the angle between the direction of the centrifugal force and the inclined surface should be taken into account. Let α to be the dynamic angle of repose, and β to be the angle defined in Figure 4.35. Simulation results in Figure 4.34 were normalized by divided by $\sin\alpha(1-\cos\beta)$ and are shown in Figure 4.36. From Figure 4.36, it was found that there was a small disparity for the simulation data when normalized by $\sin\alpha(1-\cos\beta)$. That means higher dynamic angle of repose and the angle between the centrifugal force and the inclined surface were obtained for higher fractional fill volume, both of which contribute to the increase of the surface velocity of particles along the inclined surface.
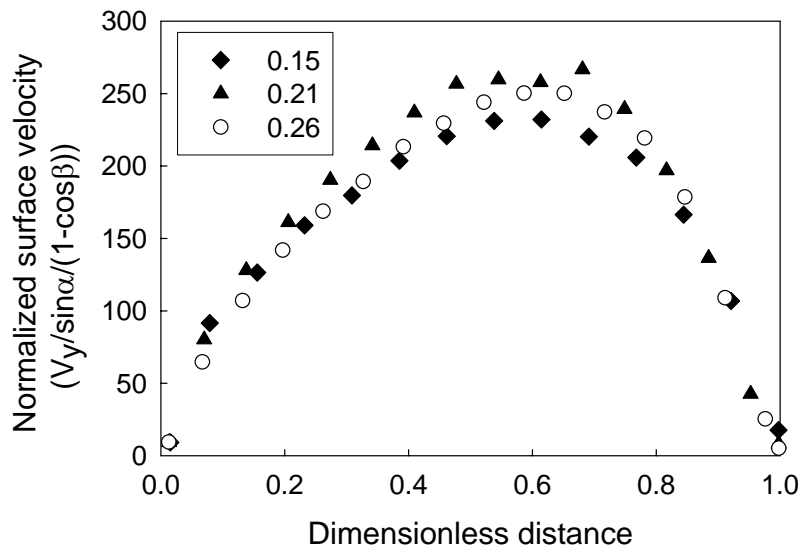
Figure 4.36 Normalized surface velocity profiles for all three fractional fill volumes in Figure 4.33 by $\sin\alpha(1-\cos\beta)$

4.6.1.3 Effect of the diameter of rotating drum

It was shown that the surface velocity was proportional to the radius of the drum when all experiments were conducted in a tumbling blender along with fractional fill volume of 0.5 [66].

However, the fractional fill volume of the particle bed is usually much less than 0.5 for particle processes in the pharmaceutical industry, especially for particle coating in a pan coater. Therefore, a question arises as to whether this relationship between the surface velocity and radius of the drum is valid for smaller fractional fill volumes.

Figure 4.37 shows the surface velocity profiles of particles along the inclined surface for the simulations of the movement of 9 mm polystyrene balls in rotating drums with two different drum diameters. The diameters of the drums are 29 cm and 58 cm, respectively. The rotation speed of the drum was 12 rpm for both cases. The fractional fill volume was set to be 0.25. From Figure 4.37, it is seen that the surface velocities for the 58 cm drum were much larger than those for the 29 cm drum. The reason is that the length of the inclined surface is proportional to the drum diameter when the fractional fill volume is kept constant. Therefore, particles on the inclined surface take more time to reach the center of the chord for the larger drum.
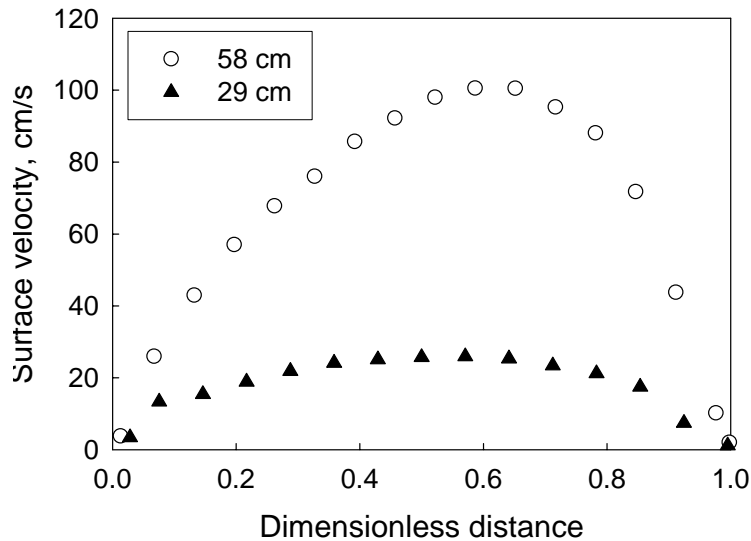
Figure 4.37 Surface velocity profiles for two different drum sizes using 9 mm polystyrene balls (pan speed is 12 rpm and $\upsilon = 0.25$)

The surface velocity profiles for two drums with different diameters were also normalized by dividing by R^2 as shown in Figure 4.38. Here R is the radius of the drum. From Figure 4.38, it can be seen that good agreement was obtained, especially for the lower part of the inclined surface. This simulation results are in contrast to the experimental results of Alexander and Muzzio [66]. They proposed that there is a linear relationship between surface velocity and the radius of the drum. It should be noted that they obtained all experimental data with the fractional fill level of 0.5.
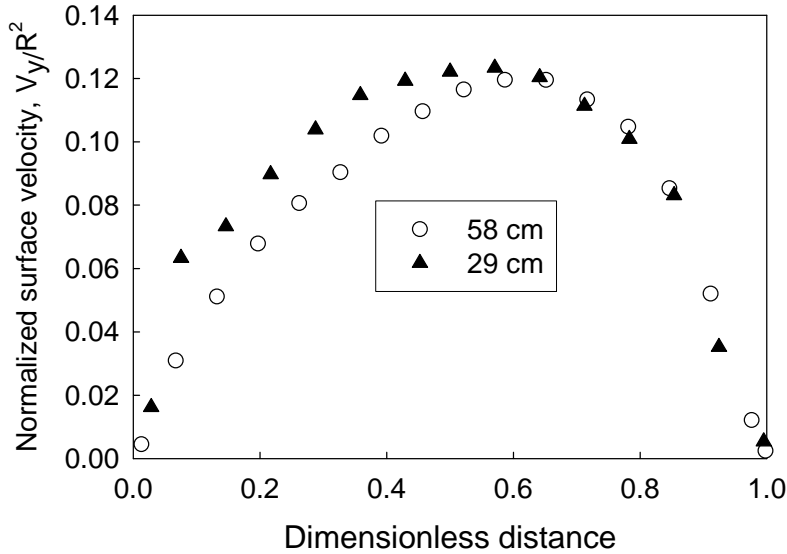
Figure 4.38 Normalized surface velocity profiles from Figure 4.37 divided by R^2 for two different drums

Therefore, based on the above simulation results and experimental work of Alexander and Muzzio [66], the relationship of the surface velocity of particles with the radius of the drums is suggested as follows:

$$V_y \propto R^n$$

where R is the radius of the drum, n is constant and is a function of fractional fill volume.

$$n = f(\upsilon) = \begin{cases} 1 & \upsilon = 0.5 \\ 2 & \upsilon = 0.25 \end{cases}$$

In fact, in order to get more consistent surface velocity profiles, especially for the smaller drum, the fractional fill volume should be as large as possible. Figure 4.39 shows the velocity profiles for 4 different fractional fill volumes in a 29 cm rotating drum. The rotation speed of the drum was 6 rpm. As shown in this figure, the fractional fill volume should be larger than 0.25 to obtain a consistent velocity profile. The reason is that the S-shape of the inclined surface was obtained for the lower fractional fill volume, while the inclined surface is more flat when the fractional fill volume is increased. In addition, particles reach the maximum velocity at about 0.4 of the dimensionless distance when fractional fill volume is less than 0.5, which is very different from the velocity profile obtained from the larger drum. Therefore, when addressing scale-up issues for particle coating processes, the difference due to the change in drum size must be taken into account.
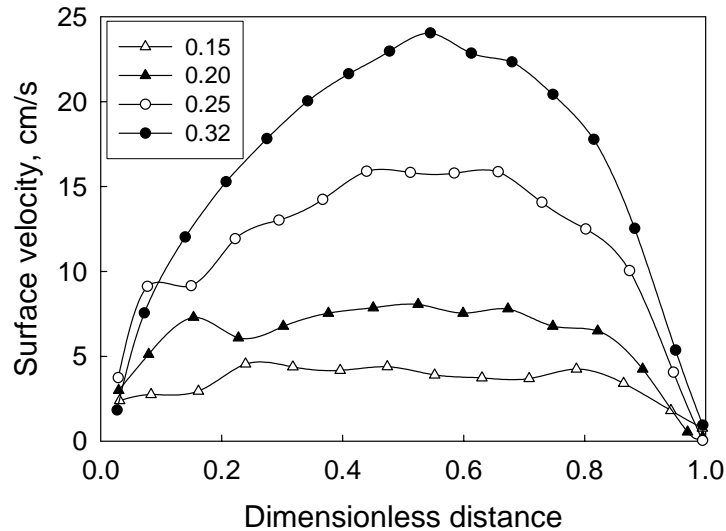
Figure 4.39 Surface velocity profiles for different fractional fill volume at a 29 cm rotating drum using 9 mm polystyrene balls along with the rotation speed of 6 rpm

4.6.2 Multi-particle DEM simulations using tablets

For the multi-particle DEM simulations using tablets, tablet shape is represented by using 3-sphere model and the contact algorithms for tablet-flat surface, tablet-curved surface and tablet-tablet contacts were also implemented by IETek (Tacoma, WA) to investigate the tablet movement in a rotating drum. The GUI for multi-particle simulations using tablets is similar to that for multi-spherical sphere simulations shown in Figure 4.27. The only difference is that the size and the shape of the tablet are defined by using the three parameters in Figure 4.2, which are the edge thickness, the center thickness, and diameter of the tablet.

The steady-state conditions were first investigated for multi-particle simulations using tablets in a rotating drum. The simulations were conducted in a 29 cm diameter rotating drum with a rotation speed of 6 rpm. 1500 tablets were used in the simulation. The edge thickness, the center thickness and diameter of the tablet were 3.2, 5.1 and 8 mm, respectively. The density of the tablet was 1.2 g/cm^3. Other parameters used in the DEM simulations are determined based on the discussion in Section 4.3 and shown in Table 4.1. Figure 4.40 shows the dynamic angles at different simulation times. The average surface velocities of tablets at different simulation times are also shown in Figure 4.40. From Figure 4.40, it is seen that the steady-state conditions for the average dynamic angle and surface velocity were obtained after 6 seconds of simulations. Therefore, results for all multi-particle simulations using tablets were reported for 8 seconds.
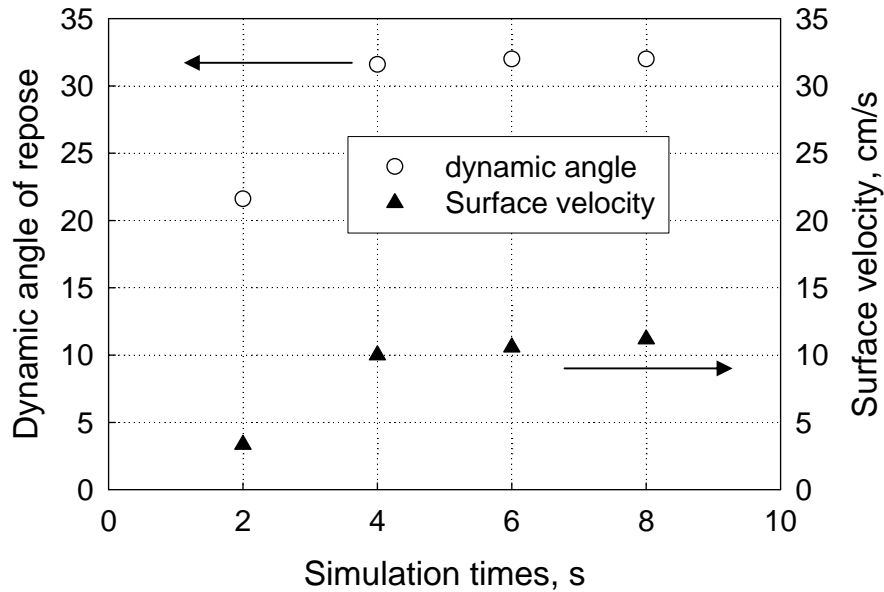
Figure 4.40 Variation of dynamic angle of repose and surface velocity as a function of actual rotation time of pan for 1500 tablets in a 29 cm rotating drum

The effect of particle shape on the dynamic behavior of particle movement in a rotating drum was studied in the simulations. In this comparison, 1500 tablets and 1500 spherical particles were used. The edge thickness, the center thickness and diameter of the tablet are 3.2, 5.1 and 8 mm, respectively. The volumes of the spherical particle were equal to the volumes of the tablet and all other physical properties were the same. The diameter of the drum was 29 cm and the pan speed was 6 rpm. The dynamic angle of repose for spherical particles is 25.2^{o}, while it is 32° for tablets in the simulation. Since all the physical properties and the number of spheres and tablets are the same in the simulations, it can be assumed that the fractional fill volumes remain constant for multi-particle simulations using spheres and tablets. Based on the discussion in Section 4.6.1, the surface velocity profiles both from multi-particle simulations using spheres and tablets are normalized by $\sin \alpha$. Figure 4.41 shows the normalized surface velocity profile along the inclined surface for tablet and spherical particle simulations in a rotating drum.
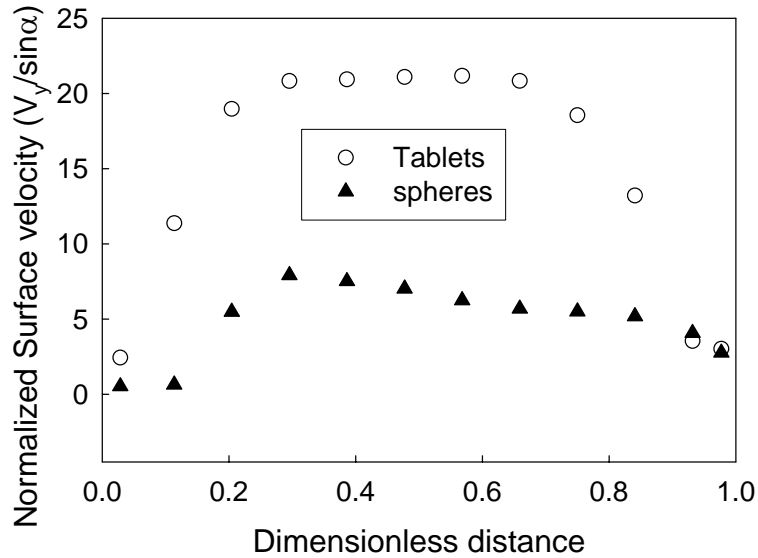
Figure 4.41 Comparison of normalized surface velocity profile by $\sin \alpha$ **along the inclined surface between tablet and spherical particles (The diameter of the drum used is 29 cm and pan speed 6 rpm)**

From this figure, it can be seen that the surface velocity of tablets is much larger than that for spherical particles, which is consistent with the work of Pandey et al. [2], even though the dynamic angle of repose is considered for the effect of surface velocity of particles. The reason may be that the component of resisting force acting on the moving tablets along the inclined surface is much less than that for the spherical particles.

As shown in Figure 4.18, the computational time for a single tablet-tablet contact was about 1.5 times longer than for a single sphere contact. Therefore, the computational time for multi-particle simulations using tablets will be much larger than for multi-particle simulations using spheres when the same number of particles was used in both cases. Simulation results for the 1500 tablets and spheres simulations in a rotating drum showed that the computational time for tablet simulations is about 60 times longer than that for spherical particle simulations in the rotating drums. Another reason for this is that it takes a longer time to visualize the tablet shape during the simulation compared to the shape of spheres.

5. Conclusions and Recommendation for Future Work

By using the intersection of three convex spherical surfaces, a very realistic representation of typical standard round tablets was created. Based on the geometry of tablet using this representation, contact detection algorithms for Tablet-Flat Surface, Tablet-Curved Surface and Tablet-Tablet were developed. Comparison of the simulation results for the collision of two tablets with those obtained from experiment showed that the interaction between two tablets can be simulated by using DEM methods. In addition, simulation results for the collision of two tablets using multi-sphere representation methods showed that the computational time for the 66- and 178- sphere representations were much larger than that of the tablet shape representation using 3-sphere model, and the dynamic behavior of the tablet was very different from any of the multi-sphere representations. Therefore, by using three convex spherical surfaces, the shape of common spherical capped tablets can be represented accurately and the dynamic behavior obtained via DEM simulations are more close to the actual behavior of colliding tablets.

Simulation results for the effect of liquid bridging between two tablets on the dynamic behavior of tablets indicated that the presence of liquid bridges should be taken into account when simulating coating processes in a rotating drum. It was shown that the capillary force can be ignored compared to the viscous forces caused by the liquid bridge, especially for liquids with high viscosity. Additionally, study of the effect of the viscosity of liquid on the limiting separation distance used in the liquid force model showed that there was a linear relationship between limiting separation distance and viscosity of the liquid. The higher the viscosity of the liquid, the larger the limiting separation distance needed in the liquid force model. The order of magnitude of the limiting separation distance was about 1 mm.

For the multi-particle DEM simulations using spheres, the simulations reached steady state (both for dynamic angle and average surface velocity) after approximately 6 s of pan rotation. The dynamic angle and average surface velocity were found to increase with increasing pan speed. The velocity profile along the inclined surface was found to be more symmetric for high pan loadings. The particles were found to reach their maximum velocity close to the mid-point of the plane defining the inclined surface. Study of the effect of particle size and radius of the drum on the surface velocity of particles along the inclined surface showed that the surface velocity of particles was inversely proportional to the square root of the diameter of the particles, and the surface velocity of particles is proportional to the square of the radius of the drum. In addition, the fractional fill volume in the smaller drum should be larger than 0.25 to obtain a consistent velocity profile. The effect of fractional fill volume on the surface velocity was also investigated and the results showed that the surface velocity was increased with increasing fractional fill volume. The higher dynamic angle was obtained when fractional fill volume was increased. In addition, the resistance of particles on the inclined surface was decreased for higher fractional fill volume, which resulted in the much higher surface velocity of particles.

Comparison of the surface velocity profile from multi-particle simulations using tablets with that from multi-particle simulations using spheres showed that the surface velocity of tablets was much larger than that for spherical particles. Simulation results for 1500 tablets and spheres in a rotating drum showed that the computational time for tablets was about 60 times longer than that for spheres.

Future work should be focus on studying multi-particle simulations using tablets in a rotating drum. The effect of particle size, fractional fill volume and the radius of the drum on

the surface velocity of tablets should be investigated and compared with those from multi-particle simulations using spheres. The liquid force model should be implemented into the current DEM code to simulate realistic coating processes. Since the computational time for tablet simulations was much larger than that for sphere simulations, clustering techniques should be developed for multi-particle simulations using tablets in the rotating drums.

6. Nomenclature

a	radius of the contact area in Figure 2.1	cm
A_c	the projected contact area in Section 3.2	cm^2
A_R	rotation matrix in Section 2.4	
C	constant in Section 4.3	
d	distance defined in Figures 4.4-4.6, 4.8-4.9	mm
e	coefficient of restitution in Section 2.2.2	
e^b	one vector in local coordinate in Section 2.4	
e^s	one vector in global coordinate in Section 2.4	
e_i	unit vector in Figure 2.2	
E	Young's modulus of the tablet in Section 3.2	GPa
E_i	Young's modulus of the indenter in Section 3.2	GPa
E_r	reduced modulus in Section 3.2	GPa
E_1, E_2	Young's modulus in Section 2.2.1	GPa
$(F_n)_N$	normal force at time step N in Section 2.2.2	N
$(F_s)_N$	shear force at time step N in Section 2.2.2	N
$(F_s)_{max}$	maximum value of shear force Section 2.2.2	N
F_n	normal force between two contact particles in Section 2.2.2	N
$F_{n\,max}$	the maximum normal force between two contact particles in Section 2.2.2	N
f_L	adhesion force in Section 2.6	N
F_L	dimensionless force in Section 2.6	
F_y	the normal force corresponding to elastic limit δ_y in Section 2.2.2	N
F	total force acting on the particle in Section 2.1	N
F_{v_n}	viscous force in normal direction in Section 2.6	N
F_{v_t}	viscous force in tangential direction in Section 2.6	N
ΔF_n	relative displacement increments within the Δt in e_i in Section 2.2.2	micron

ΔF_s	relative displacement increments within the Δt in e_i in Section 2.2.2	micron
g	gravitational acceleration	N/m^2
h	indentation depth in Section 3.2	nm
h_m	the maximum indentation depth in Section 3.2	nm
h_t	tangent depth in Section 3.2	nm
h_c	contact depth in Section 3.2	nm
H	hardness of the sample in Section 3.2	MPa
k_1	plastic stiffness for loading in Section 4.3	
k_2	plastic stiffness for unloading in Section 4.3	
K_n	elastic stiffness in Section 2.2.2	
K_1	stiffness for loading between two contact particles in Section 2.2.2	
K_2	stiffness for unloading between two contact particles in Section 2.2.2	
K_T	effective tangential stiffness in Section 2.2.2	
K_0	initial tangential stiffness in Section 2.2.2	
$\hat{k}_{ij}$	unit vector in Section 2.2.2	
k_s	the shear stiffness in Section 2.2.2	
k_n	the normal stiffness in Section 2.2.2	
k_y	plastic stiffness for loading in Section 2.2.2	
k_{un}	plastic stiffness for unloading in Section 2.2.2	
I_{xx}, I_{yy}, I_{zz}	principal components of inertia tensor in Section 2.1	
L	distance between two centers in Figure 2.2	mm
L_1	the edge thickness of the tablet in Figure 4.2	mm
L_2	the center thickness of the tablet in Figure 4.2	mm
L_3	the diameter of the tablet in Figure 4.2	mm
m	the mass of the tablet in Section 4.1	
n	power law exponent in Section 3.2	
$\dot{n}$	projection of $\dot{X}_i$ on e_i in Section 2.2.2	

$\Delta n, \Delta s$	components of the relative displacement increment in Section 2.2.2	micron
Q	quaternion in Section 2.4	
P	loading force in Section 3.2	N
$P_{\max}$	the maximum loading force in Section 3.2	
$P_{(x)}, P_{(y)}$	the points in Figure 2.2	
P_t	total loading force in Section 2.2.1	N
$\vec{r}_i$	radius vector for the location of sphere I in Section 2.2.2	
r	position of the particle defined in Section 2.1	
r_1, r_2	radii of curvature of the liquid bridge in Section 2.6	mm
R	radius of spherical particle in Figure 2.1	cm
$R_{(x)}, R_{(y)}$	radii of discs in Figure 2.2	
R_1	radius of particle in Section 2.6 and radius of sphere 1 in Figure 4.1	cm
R_2	radius of particle in Section 2.6 and radius of sphere 2 in Figure 4.1	cm
R^*	reduced radius of spheres in Section 2.6	cm
$\dot{s}$	projection of $\dot{X}_i$ on t_i in Section 2.2.2	
$\Delta \vec{s}$	relative tangential surface displacement in Section 2.2.2	micron
S	separation distance between two tablets in section 2.6	m
	contact stiffness in Section 3.2	
S_C	limiting separation distance between two tablets in section 2.6	m
t_i	unit vector in Figure 2.2	
Δt	time interval between two time steps in Sections 2.1, 2.2.2	second
T	total tangential force in Section 2.2.2	N
T^*	relative tangential force in Section 2.2.2	N
T_t	total detection time in Section 2.3.3	second
v	velocity of the particle in Section 2.1	m/s
v_n	the relative normal velocity of the spheres in Section 2.6	m/s
v_t	the relative tangential velocity of the spheres in Section 2.6	m/s
$\vec{U}_1$	unit vector defined in Figure 4.7	

V	the volume of the tablet in Section 4.1	cm^3
$\vec{V}_1$	vector defined in Figure 4.7	
$\vec{V}_2$	vector defined in Figure 4.7	
$\overleftarrow{V}_{12}$	vector defined in Figure 4.7	
V_y	cascading average velocity in Section 3.4	cm/s
X	distance defined in Figure 4.19	mm
$\dot{x}, \dot{y}$	linear velocity in Section 2.2.2	
$\dot{X}_i$	relative velocity in Section 2.2.2	m/s
Z	distance defined in Figure 4.1	mm

Greek symbols

α	angle defined in Figures 4.1 and 4.34	degree
β	angle defined in Figures 4.1 and 4.34	degree
γ	surface tension of liquid in Section 2.6	mN/m
	angle defined in Figures 4.4-4.6, 4.8-4.10, 4.14-4.15	degree
γ_1	angle defined in Figures 4.11-4.13	degree
ϕ	Euler's angle in Section 2.4	degree
θ	Euler's angles in Section 2.4	degree
	dynamic angel of repose in Section 3.4	degree
ψ	Euler's angles in Section 2.4	degree
φ	angle in Figure 2.2	degree
ϕ_μ	interparticle friction angle in Section 2.2.2	degree
μ	coefficient of friction in Section 2.2.2	
	fluid's viscosity in Section 2.6	kg/m.s
v_i	Poisson coefficient of the indenter in Section 3.2	
υ	fractional fill volume in Section 4.5	
v_1, v_2	Poisson coefficients in Section 2.2.1	
$\dot{\theta}_x, \dot{\theta}_y$	angular velocity in Section 2.2.2	r/s

$\omega_x^b, \omega_y^b, \omega_z^b$	angular velocities in the body-fixed coordinate in Section 2.1	r/s
$\tau_x^b, \tau_y^b, \tau_z^b$	three components of the torque in the body-fixed system in Section 2.1	N.m
ρ	the density of the tablet in Section 4.1	g/cm^3
δ	overlap of two contact particles in Figure 2.1	micron
δ_0	the value of δ where the unloading force is zero in Section 2.2.2	micron
δ_y	elastic limit in Section 2.2.2	micron
δ_{max}	the maximum value of δ for loading in Section 2.2.2	micron
λ	parameter for effective tangential stiffness in Section 2.2.2	

Abbreviations

CFD	computational fluid dynamics
COR	coefficient of restitution
FDM	force displacement model
GUI	graphical user interface
MHT	micro hardness tester
MRI	magnetic resonance imaging

7. Reference

[1]   K. Yamane, T. Sato, T. Tanaka and Y. Tsuji, Computer simulation of tablet motion in coating drum, Pharmaceutical Research, 12(9)(1995) 1264-1268.

[2]   P. Pandey and R. Turton, Movement of different shaped particles inside a pan coating device using novel video-imaging techniques, AAPS PharmSciTech 6(2)(2005) article # 34.

[3]   P. Pandey, Y. Song, F. Kahiyan and R. Turton, Simulation of particle movement in a pan coating device using a new MATLAB-based Discrete Element Modeling code, Powder Technology, 161(2006) 79-88.

[4]   Y. Muguruma, T. Tanaka and Y. Tsuji, Numerical simulation of particulate flow with liquid bridge between particles (simulation of centrifugal tumbling granulator), Powder Technology, 109(2000) 49-57.

[5]   P.A. Cundall, A computer model for simulating progressive, large-scale movements in blocky rock system, Proc. Symp. Intl. Society of Rock Mechanics, Nancy 2, France, 1971.

[6]   P.A. Cundall, Rational Design of Tunnel Supports: A Computer Model for Rock Mass Behavior Using Interactive Graphics for the Input and Output of Geometrical Data, Technical Report MRD-2-74, Missouri River Division, Corps of Engineers, September, 1974.

[7]   M.P. Allen and D.J. Tildesley, Computer Simulation of Liquids, Oxford Science Publications, 1987.

[8]   R.W. Hockney and J.W. Eastwood, Computer simulation using particles, McGraw-Hill, New York, 1981.

[9]   Wm. G. Hoover, Computational Statistical Mechanics, Elsevier Science Publications, Amsterdam, 1991.

[10]   A. Brodka and T.W. Zerda, Dynamics of liquid acetone: computer simulation, Journal of Chemical Physics, 104(1996) 6313-6318

[11]   P.M. Rodger, A.J. Stone and D.J. Tildesley, The intermolecular potential of chlorine: a three phase study, Molecular Physics, 63(1988) 173-188.

[12] W.C. Swope and H.C. Andersen, 106-particle molecular-dynamics study of homogeneous nucleation of crystals in a supercooled atomic liquid, Physical Review B, 41(1990) 7042-7054.

[13] O.R. Walton and R.L. Braun, Simulation of Rotary-Drum and Repose Tests for Frictional Spheres and Rigid Sphere Clusters, Joint DOE/NSF workshop on Flow of Particulates and Fluids, Sept. 29-Oct. 1, 1993, Ithaca, NY.

[14] C.S. Campbell and C.E. Brennen, Computer simulation of granular shear flows, Journal of Fluid Mechanics, 151(1985) 167-188.

[15] Y. Wang and M.T. Mason, Two-dimensional rigid-body collisions with friction, Journal of Applied Mechanics, 59(1992) 635-642.

[16] C. Hogue and D. Newland, Efficient computer simulation of moving granular particles, Powder Technology, 78(1994) 51-56.

[17] B.P.B. Hoomans, J.A.M. Kuipers, W.J. Briels and W.P.M. Van Swaaij, Discrete particle simulation of bubble and slug formation in a two-dimensional gas-fluidized bed: a hard-sphere approach, Chemical Engineering Science, 51(1)(1996) 99-118.

[18] H. Hertz, Uber die beruhruing fester elasticher Korper (on the contact of elastic solids), Journal of Reine Angewandtl Math., 92(1882) 156-171.

[19] K.L. Johnson, Contact Mechanics, Cambridge University Press, 1997.

[20] P.A. Cundall and O.D.L. Strack, A discrete numerical model for granular assemblies, Geotechnique, 29(1)(1979) 47-65.

[21] J.O. Hallquist and NIK2D-A Vectorized, Implicit Finite-Deformation Finite Element Code for Analyzing the Static and Dynamic Response of 2-D Solids, Lawrence Livermore Nat'l lab. Rept. UCID-19677, Feb., 1983.

[22] O.R. Walton and R.L. Braun, Viscosity, Granular-Temperature, and Stress Calculations for Shearing Assemblies of Inelasitc, Fricitional Disks, Journal of Rheology, 30(5)(1986) 949-980.

[23] R.D. Mindlin, Compliance of Elastic Bodies in Contact, Journal of Applied Mechanics, 16(1949) 259-268.

[24] R.D. Mindlin and H. Deresiewicz, Elastic spheres in contact under varying oblique forces, Journal of Applied Mechanics, 20(1953) 327-344.

[25] O.R. Walton, Numerical simulation of inclined chute flows of monodisperse, inelastic, frictional spheres, Mechanics of Materials, 16(1993) 239-247.

[26] C. Thornton, Coefficient of Restitution for Collinear Collisions of Elastic-Perfectly Plastic Spheres, Journal of Applied Mechanics, 64(1997) 383-386.

[27] B.K. Mishra, Ball charge dynamics in a planetary mill, KONA Powder particle, 13(1995) 151-158.

[28] Y. Tsuji, T. Tanaka and T. Ishida, Lagrangian numerical simulation of plug flow of cohensionless particles in a horizontal pipe, Powder Technology, 71(1992) 239-250.

[29] K.J. Yamane, T. Sato, T. Tanaka and Y. Tsuji, Computer simulation of Tablet motion in Coating Drum, Pharmaceutical Research, 12(9), 1264-1268, 1995.

[30] B. Quentree and C. Brot, New method for searching for neighbors in molecular dynamics computations, Journal of Computational Physics, 13(1975) 430-432.

[31] L. Verlet, Computer 'experiments' on classical fluids I, Thermodynamical properties of Lennard-Jones molecules, Physical Review, 159(1967) 98-103.

[32] D. Knuth, The art of computer programming (2nd edition), Addison-Wesley, MA, 1973.

[33] A. Munjiza and K.R.F. Andrews, NBS Contact Detection Algorithm for Bodies of Similar Size, International Journal for Numerical Methods in Engineering, 43(1998) 131-149.

[34] J.J. McCarthy, Discrete Modeling of Complex Particulate and Multiphase Processes, Summer School in Winter, University of Florida, ERC for particle Science and Technology, January 9-16(2004).

[35] D.J. Evans, On the representation of orientation space, Molecular Physics, 27(1977) 317-325.

[36] W.R. Hamilton, On quaternion; or on a new system of imaginaries in algebra, Philosophical Magazine, XXV.(1844) 10-13.

[37] H. Goldstein, Classical Mechanics (2nd edition), Addison-Wesley, MA, 1980.

[38] K. Shoemake, Animating rotation with Quaternion Cruves", Computer Graphics, Proceedings of SIGGRAPH, 19(3)(1985) 245-254.

[39] G. Baumann, I.M. Janosi and D.E. Wolf, Surface properties and flow of granular material in a two-dimensional rotating-drum model, Physical Review E, 51(3), 1879-1888, 1995.

[40] G.A. Kohring, Studies of diffusional mixing in rotating drums via computer simulations, Journal of Physics I France, 5(1995), 1551-1561.

[41] J.J. McCarthy and J.M. Ottino, Particle dynamics simulation: a hybrid technique applied to granular mixing, Powder Technology, 97(1998) 91-99.

[42] K. Yamane, M. Nakagawa, S.A. Altobelli, T. Tanaka and Y. Tsuji, Steady particulate flows in a horizontal rotating cylinder, Physics of Fluids, 10(6)(1998) 1419-1427.

[43] R.Y. Yang, R.P. Zou, and A.B. Yu, Microdynamic analysis of particle flow in a horizontal rotating drum, Powder Technology, 130(2003), 138-146.

[44] X. Lin and T.T. Ng, Contact detection algorithms for three dimensional ellipsoids in discrete element modeling, International Journal for Numerical and Analytical Methods in Geomechanics 19(9)(1995) 653– 659.

[45] R. Hart, P.A. Cundall and J. Lemos, Formulation of a three-dimensional distinct element model: Part II. Mechanical calculations for motion and interaction of a system composed of many polyhedral blocks, International Journal of Rock Mechanics & Mining Sciences & Geomechanics Abstracts 25(3)(1998) 117– 125.

[46] J.R. Williams and A.P. Pentland, Superquadrics and modal dynamics for discrete elements in concurrent design, 1st US Conference on DEM, Golden, CO, 1989.

[47] J. Favier, M.H. Abbaspour-Fard, M. Kremmer and A.O. Raji, Shape representation of axi-symmetrical, non-spherical particles in discrete element simulation using multi-element model particles, Engineering Computations-International Journal for CAE and Software 16(4)(1999) 467–480.

[48] H. Abou-Chakra, J. Baxter and U. Tuzun, Three-dimensional shape descriptors for computer simulation of non-spherical particulate assemblies, Advanced Powder Technology 15(1)(2004) 63– 77.

[49] J.A. Elliott and A.H. Windle, A dissipative particle dynamics method for modeling the geometrical packing of filler particles in polymer composites, Journal of Chemical Physics 113(22)(2000) 10367–10376.

[50] M. Gan, N. Gopinathan, X. Jia and R.A. Williams, Predicting packing characteristics of particles of arbitrary shapes, KONA 22(2004) 82– 93.

[51] L. Vu-Quoc, X. Zhang and O.R. Walton, A 3-D discrete-element method for dry granular flows of ellipsoidal particles, Computer Methods in Applied Mechanics and Engineering, 187(2000) 483-528.

[52] Y. Cao, An efficient detection algorithm for arbitrary rigid shapes, Master's thesis, University of Florida, Gainsville, FL, 1996.

[53] X. Lin and T.T. Ng, Numerical modeling of granular soil using random arrays of three dimensional elastic ellipsoids, in: Eighth International Conference on Computer Methods and Advances in Geomechanics, 1, Morgantown, WV, 1994.

[54] J.R. Williams and R. O'Connor, A 3D representation scheme for fast contact detection in multi-body dynamics, Technical report, Intelligent Engineering Systems Laboratory (IESL), Department of Civil and Environmental Engineering, MIT, Cambridge, MA, Contract No: F29601-91-C-0029, 1995.

[55] Y. Muguruma, T. Tanaka and Y. Tsuji, Numerical simulation of particulate flow with liquid bridge between particles (simulation of centrifugal tumbling granulator), Powder Technology, 109(2000) 49-57.

[56] R.A. Fisher, On the capillary forces in an ideal soil, Journal of Agricultural Science, 16(1926) 491-505.

[57] S. T. Nase, W. L. Vargas, A. A. Abatan and J.J. McCarthy, Discrete characterization tools for cohesive granular material, Powder Technology, 116(2001) 214-223.

[58] E. Poire, Analytical Report MHT-020830, Micro Photonics Inc., Aug. 30, 2002.

[59] Y. Song, R. Turton and F. Kayihan, Contact detection algorithm for DEM simulation of tablet-shaped particles, Powder Technology, 161, 32-40, 2006.

[60] F. Bertrand, L.-A. Leclaire, and G. Levecque, DEM-based models for the mixing of granular materials, Chemical Engineering Science 60(2005) 2517-2531.

[61] S. J.R. Simons, Liquid bridges in granules, Handbook on Granulation, book chapter submitted to Elsevier, 2006.

[62] http://www.herc.com/aqualon/pharm/pharm_data_sheets/images/pdf_files/vc_556c.pdf

[63] D.N. Mazzone, G.I. Tardos and R. Pfeffer, The behavior of liquid bridges between two relatively moving particles, Powder Technology 51 (1987) 71-83.

[64] E. Poire, Analytical Report MHT-020830, Micro Photonics Inc., May 2th , 2002.

[65] Y. Ding, S. Antony and J. Seville, Granular motion in the transverse plane of rotating drum, in: Antony, Hoyle, Ding (Eds.), Granular Materials Fundaments and Applications, Royal Society of Chemistry, Cambridge, UK, 2004.

[66] A. Alexander and F. Muzzio, Batch size increase in dry blending and mixing, in: Levin (Ed.), Pharmaceutical Process Scale-up, Marcel Dekker, New York, 2001.